AFIT/GAE/ENY/92D-04

COMPUTATIONAL AND EXPERIMENTAL INVESTIGATION INTO FRACTURE OF BRITTLE FIBER - BRITTLE MATRIX COMPOSITE SYSTEMS

THESIS

James Paul Solti, Captain, USAF

AFIT/GAE/ENG/92D-04

AFIT/GAE/ENY/92D-04

COMPUTATIONAL AND EXPERIMENTAL INVESTIGATION INTO FRACTURE OF BRITTLE FIBER - BRITTLE MATRIX COMPOSITE SYSTEMS

THESIS

Presented to the Faculty of the School of Engineering of the

Air Force Institute of Technology

Air University

In Partial Fulfillment of the Requirements for the Degree of Master of Science in

Aeronautical Engineering

James Paul Solti, B.S., M.S.

December 1992

Preface

It would be impossible to list on a single page all the individuals who were instrumental in the completion of this project. From the professors and students here at AFIT to those at U.D., O.S.U. and Wright State; from the Scientists and technicians at the Material's Lab to the numerous manufacturing companies, glass blowers, and imaging personal, my heartfelt thanks to all. I was fortunate to have two very knowledgeable advisors to help me through all the trials and tribulations. Dr. Palazotto and Dr. Larson's guidance through the world of Fracture Mechanics was instrumental to my understanding of the problem at hand. Special thanks to the Dr. Kerans, Dr. Parthasarathy, Dr. Jero and the rest of the Ceramics Division at the Material's Lab for all their help. I am also grateful to my committee members, Dr. Mall and Dr. Torvik, for all their guidance and encouragement. Bill and Mark for scrounging anything I ever asked for. Jim and Keith for answering all my questions. I cannot express my appreciation enough for all the work performed by the AFIT Model Shop. No matter what the task or how many changes I threw at them, they finished them all with flawless quality; ahead of schedule, and never a complaint. Thanks. Lastly, I'd like to thank my wife, Christine, who stayed up many a night learning more about "breaking glass" than any optometrist should.

James P. Solti

Table of Contents

Chapter 2

Chapter 3

Chapter 4

List of Figures

List of Tables

List of Symbols

a ..... half crack length

A ..... cross-sectional area

B ..... material thickness

c ..... compliance

d ..... distance from crack tip

δ ..... crack opening

E ..... Young's modulus or energy

γ ..... Surface Energy

FG ..... Frictional Grab

Γ ..... slip length

k ..... radius of gyration

K ..... stress intensity factor

K_{1c}..... fracture toughness

μ ..... friction coefficient

p ..... applied load or pressure

r ..... radius

r_f ..... fiber radius

r_m ..... matrix radius

r_p ..... radius of plastic zone

R ..... critical energy release rate (material property)

σ_n ..... normal stress

σ_0 ..... driving stress

σ_∞ ..... far-field applied stress

σ_r ..... residual normal compressive stress

σ_y ..... yield stress

τ ..... surface tractions or shear stress

ABSTRACT

Experimental and computational analyses provided an improved understanding of quasi-static fracture in model composite systems. Constant displacement compression tests using borosilicate glass double cleavage drilled compression test templates provided qualitative assessments of localized toughening for crack growth near cylindrical inclusions. Fiber diameter and fiber-matrix cohesion were found to be major contributors in arresting crack growth. Estimates of critical fiber spacing and optimal interfacial Frictional Grab were determined by varying these two parameters. Large crack-tip stress fields induced interfacial slip and separation prior to arrival of the main crack. Further, debonding and the proliferation of secondary matrix cracks characterized the role of bridging fibers along weak interfaces. Strong residual normal compressive interfacial stresses diminished the influence of crack-tip stresses; however, slip was still observed. VHS tape and computer enhanced photos record a history of crack propagation and interfacial slip. Experimental data was used to validate a fully three-dimensional computational code capable of analyzing fracture near and around cylindrical inclusions. Consistent variations in the shape of the crack periphery (in comparing the experimental and computational results) renders confidence in the elasticity solution.

CHAPTER 1

INTRODUCTION

The purpose of this investigation is to characterize fracture near a brittle fiber - brittle matrix interface. The development of valid design and failure criteria for ceramic composites is contingent upon a full understanding of the physical mechanisms occurring at the interface during fracture. Specifically of interest to this study is the development and influence of frictional slip zones which form at the interface. The frictional sliding within these zones plays a significant role in the local dissipation of energy which results in an overall global toughening of the composite. Experimental data is used to validate a surface integral code capable of analyzing three-dimensional fracture. Crack growth around a single fiber, characterizing a small crack in a real composite, is modelled incorporating an interfacial Coulomb friction law. The purpose of the study is not to quantify the material properties of the composite; rather to gain a better understanding of interfacial influences on fracture in brittle composites.

1.1 Background and Motivation

The ability to improve today's flight vehicles weighs heavily on the advancement of composite materials. Many military aircraft and weapon systems incorporate large percentages of composite materials in their design. The Advanced Tactical Fighter (ATF), F-117 Stealth Fighter, and B-2 Bomber use composite materials extensively throughout their primary structure. The F-15, F-14, F-16, F/A-18 and AV-8B also use composites in their design. Still others like the F-111 and A-10 are continually being modified using composite materials in many of their secondary structures. With the introduction of the National Aerospace Plane (NASP), researchers have noted, however, that the mechanical properties of today's composite materials still fall short of what is required. The NASP project calls for high strength, high modulus materials capable of maintaining their mechanical properties at temperatures in excess of 1500 degrees Fahrenheit. In order to satisfy many of these requirements, research is being diverted from standard polymer composites to ceramic matrix composites (CMCs).

Ceramic materials are excellent thermal and electrical insulators, able to withstand most environmental and chemical attacks. They possess high strength and high modulus even at elevated temperatures. The major drawback of ceramic materials is their inability to resist fracture. They are brittle. Theoretically, ceramic materials with ionic and covalent bonds are stronger than most metals, but due to the ceramic's low toughness this strength is never realized. Ironically, the complex bonding which gives ceramic materials

exceptional strength, stiffness, and environmental resistance also prevents favorable localized plastic deformation [3]. As a result, failure is often catastrophic. Voids and inclusions in the material's atomic structure act as nucleation sites where crack growth initiates. Concentrated stresses at the crack tip are usually above the material's critical threshold value allowing the crack to propagate quickly through the material.

In the early 1920's, Griffith [12] investigated the fracture behavior of brittle materials extensively. He is best known for the development of an energy equilibrium criterion which states that crack propagation will occur if the energy released upon crack growth is sufficient to provide all the energy required for crack growth [4]. In other words, the total energy released upon an incremental crack growth, da, must be equal to the sum of the negative of the work done by the tractions at the boundaries; the change in internal energy, and the energy required for the formation of the two new surfaces created by the crack growth. The total energy is defined by

$$E = -W + U + \int 2\gamma da \tag{1.1}$$

where

E = total energy

W = work done by tractions

U = elastic strain energy

γ = surface energy

da = incremental crack growth

For equilibrium to be satisfied,

$$\frac{dE}{da} = 0 \tag{1.2}$$

or from Equation (1.1)

$$\frac{dW}{da} - \frac{dU}{da} = 2\gamma = G \tag{1.3}$$

where G is known as an energy release rate characterizing the energy released per unit crack extension. Based upon stress field calculations for a centrally-located elliptical flaw, Griffith estimated that

$$G = \frac{\pi\sigma^2 a}{E} \tag{1.4}$$

Substituting Equation (1.4) into Equation (1.3), the well known Griffith energy equation is derived (Equation 1.5).

$$\sigma_{crit} = \sqrt{\frac{2E\gamma}{\pi a}} \tag{1.5}$$

The above equation states that a critical stress value exists beyond which crack growth will occur.

If manufacturers introduced mechanisms into the system to absorb the applied external and the existing internal energy, less energy would be available for the creation of new surface area (crack growth). The objective then is to either decrease the number of imperfections in the material microstructure, or to "create" energy dissipating mechanisms capable of arresting crack growth. The latter is the focus of this study.

1.2 Fracture of Composite Materials

In the early 1920's, Griffith laid the basic foundation upon which the field of Fracture Mechanics is founded. Since that time, tremendous amounts of analytical and empirical data have aided in the development of a practical set of fracture criteria for homogenous materials. Recent requirements for lighter and stronger materials have turned industry's focus toward composite materials. Specifically, focus has turned toward ceramic matrix composites (CMCs) and metal matrix composites for high temperature, high stress applications. Unfortunately, much is still unknown about failure in such materials.

Unlike polymer composites, the fibers used in ceramic matrix composites serve to slow crack growth rather than carry load. Ideally, designers would like to add fibers with high fracture toughness, but unfortunately, the design (temperature) considerations which dictated the use of ceramic materials also preclude the use of ductile fibers. Ceramic composites are, therefore, composed of brittle fibers in a brittle matrix.

Realizing that brittle fibers have low fracture toughness and are likely to fail in the presence of high crack tip stresses, the original problem: an inherent inability to resist fracture, still exists. If properly designed, however, energy which would otherwise be available for crack growth may be dissipated at the fiber/matrix interface.

As a crack advances toward a fiber, a number of physical mechanisms occur at the interface due to the presence of high crack-tip stress fields. If a chemical bond exists between the fiber and matrix, fiber debonding may occur; dissipating internal energy. Once debonded, frictional sliding across the interface initiates; again contributing positively toward toughening of the composite. As crack growth continues past the fiber, the fiber may break, pullout, or continue to bridge the matrix. The strength of the interface determines which of these events takes place. If the interface is too strong, the crack propagates though the fiber. If the interface is too weak, the entire fiber debonds. In both cases, no appreciable improvement in the mechanical properties of the composite is noticed. Bridging, however, promotes toughness through load transfer and continued frictional energy losses*.

---

*Energy which would otherwise be available for crack growth is consumed through the creation of stress fields along interlocking interfaces as shown in the figure below. Energy is also dissipated though the creation of heat (resulting from frictional sliding) and smoothing of the joining surfaces.

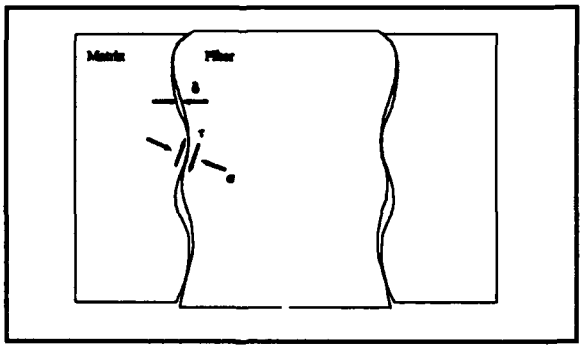

Due to potentially large frictional forces, fiber pullout may be a large contributor to the material's toughness. Fiber failure, on the other hand, releases only a small amount of energy equal to the stored elastic energy in the fiber [10]. After pullout or failure, the fiber no longer contributes to the mechanical properties of the ceramic. Figure 1.1 illustrates several events which may occur as the crack propagates through the matrix. Only by understanding how each of these events contributes to the toughening of the whole composite can suitable fracture criteria be developed.

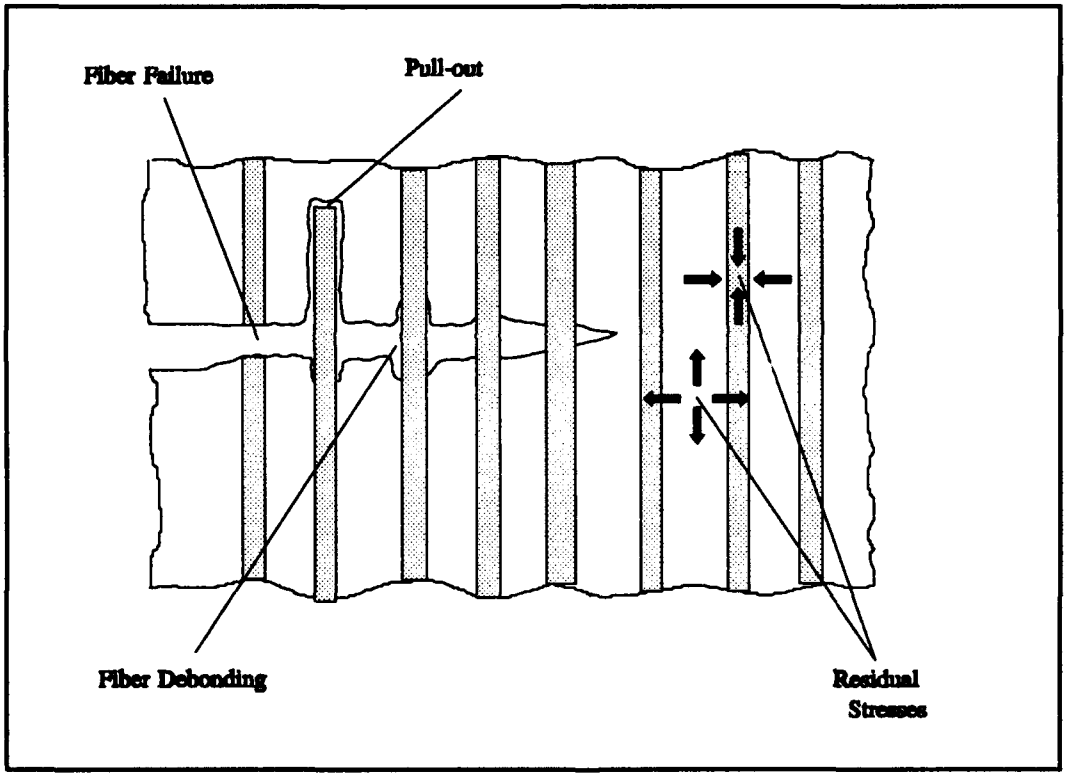

Figure 1.1 Fracture of fiber reinforced composites

Currently, two practical strengthening procedures exist for ceramic matrix composites [10]. These techniques are *flaw control* and *toughening mechanisms*. Flaw control accepts the brittleness of the material and attempts to reduce the number of material imperfections (nucleation sites) created during processing. High research and manufacturing costs coupled with the mere complexity of the task have diverted efforts toward toughening mechanisms. *Toughening* attempts to reduce the brittleness of the material by introducing energy absorbing mechanisms which prevent catastrophic failure. Bowen [3] outlines three of the most commonly used toughening mechanisms:
(1) introduction of small cracks (microcracks) into the material's microstructure,
(2) transformation toughening, and (3) fiber\whisker reinforcement.

Introducing small microcracks may appear contrary to our goal: increasing strength through the introduction of cracks? Recall, however, that crack propagation initiates due to the existence of large stress fields at the crack tip. If the large primary crack grows into one of these "microcracks," an apparent blunting of the crack tip may occur reducing the stresses at the crack tip and possibly arresting growth.

Transformation toughening involves the dispersion of small pellets of zirconia into the material. High stresses associated with the crack cause the zirconia to transform from a tetragonal to a monoclinic structure. During this transformation, the zirconia undergoes a volumetric increase; inducing localized compressive stresses which tend to close the crack tip.

Fiber reinforcement is the most common and perhaps most promising toughening mechanism. Energy is removed from the system through the aforementioned mechanisms of frictional dissipation, bridging, and pull-out occurring at the interface. The end result of all three techniques is an apparent global toughening of the composite.

1.3 Linear Theory for Brittle, Plane Strain Materials

Linear Elastic Fracture Mechanics (LEFM) theory is appealing since it allows stress fields near the crack tip to be defined by a single parameter, K. K is known as a *stress intensity factor*, and relates the applied load, crack length, and geometry through equations of the form

$$\sigma_{ij} = \frac{K}{\sqrt{2\pi r}} F(\theta) + HOT's \qquad (1.3.1)$$

where

σ = stress near crack tip

K = stress intensity factor

r = distance from the crack tip

$F(\theta)$ = function of the angle theta

HOT's = higher order terms (neglected)

For a centrally-located circular crack in an infinite body or a small crack in a finite body, the crack tip stresses are defined by

$$\sigma_x = \sigma_o \sqrt{\frac{a}{2r}} \cos\frac{\theta}{2}\left[1 - \sin\frac{\theta}{2}\sin\frac{3\theta}{2}\right]$$
$$\sigma_y = \sigma_o \sqrt{\frac{a}{2r}} \cos\frac{\theta}{2}\left[1 + \sin\frac{\theta}{2}\sin\frac{3\theta}{2}\right] \qquad (1.3.2)$$
$$\tau_{xy} = \sigma_o \sqrt{\frac{a}{2r}} \sin\frac{\theta}{2}\cos\frac{\theta}{2}\cos\frac{3\theta}{2}$$

The local coordinate system is defined as shown in Figure 1.2.

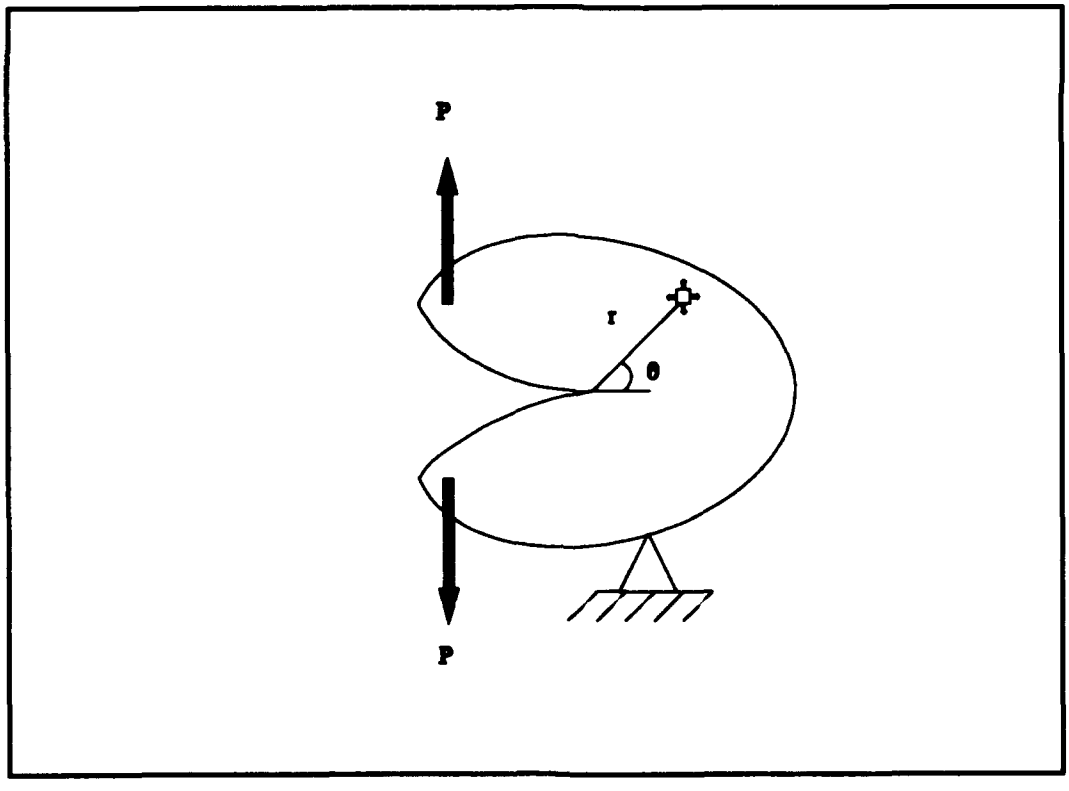

Figure 1.2 Arbitrary body

Equation (1.3.2) consists of the first term in the expansion of Equation (1.3.1) and adequately describes the stresses near the crack tip where the singularity dominates any higher order terms. These stresses are plotted for r equal a in Figure 1.3. As $r \rightarrow 0$ (approach crack tip), stresses become singular. Of course, in reality, stresses are not singular. Stresses near the crack-tip exceed the yield condition which results in a localized zone where plastic deformation occurs.

The presupposed linear assumptions require

$$\frac{r_p}{a} \leq 0.1 \qquad (1.3.3)$$

where

r_p = radius of the plastic zone

a = half crack length

This requirement is easily satisfied in brittle materials; allowing stresses to be characterized by only the stress intensity factor.

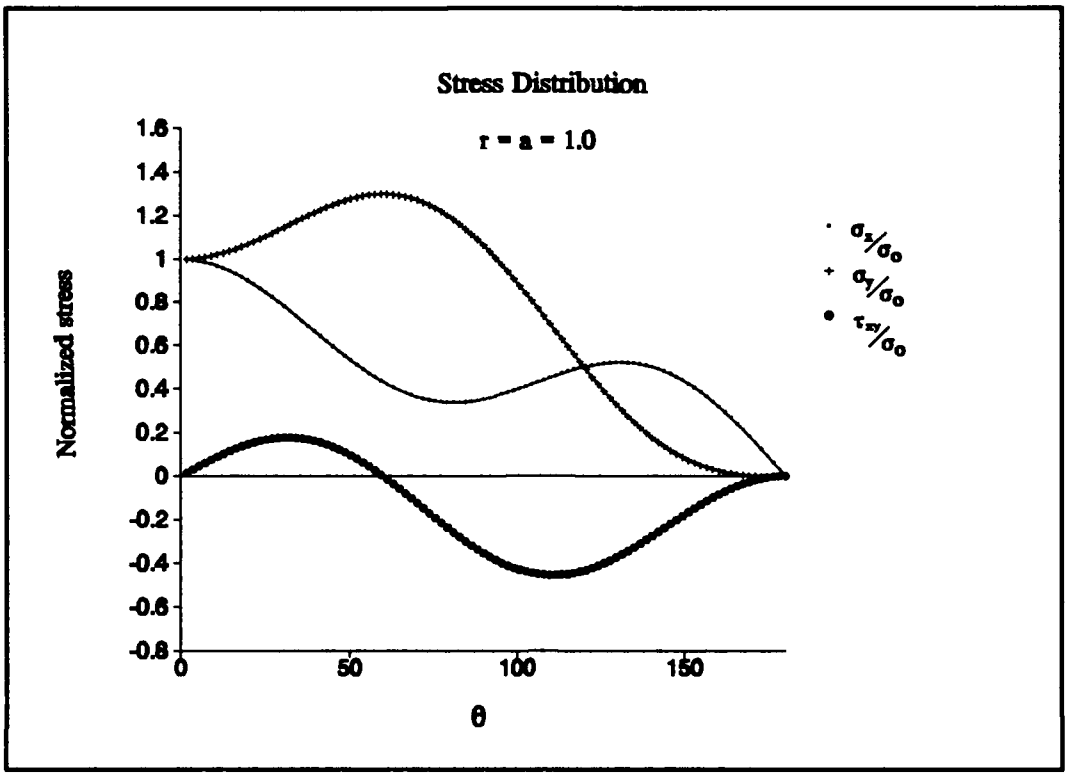

Figure 1.3 Stress distribution near crack tip

Analytical and empirical solutions exist for determining K for a myriad of geometries and loading conditions [29]. The general form of these solutions can be written as

$$K = \beta\sigma\sqrt{a\pi} \tag{1.3.4}$$

where β is a dimensionless constant relating geometries of the crack and body. Given the applied stress, σ, and half crack length, a, the stress intensity factor is easily

determined. Linear elastic theory states that crack growth will occur if K is greater than the material's fracture toughness, K_{1c}, a material property. For brittle, plane strain materials, K_{1c} is assumed constant, but will in general may vary with crack length and material thickness.

Relative motion of crack surfaces can be broken down into components in three orthogonal directions local to the crack front. Subsequently, K is divided into three modes which may be superimposed to describe a general three-dimensional loading. Stresses normal to the crack plane produce Mode I "opening"; in-plane shear results in Mode II "sliding," and out-of-plane shear yields Mode III "tearing." Deformation resulting from application of more than one mode is referred to as "mixed." Figure 1.4 illustrates the direction of deformation for each of the modes.

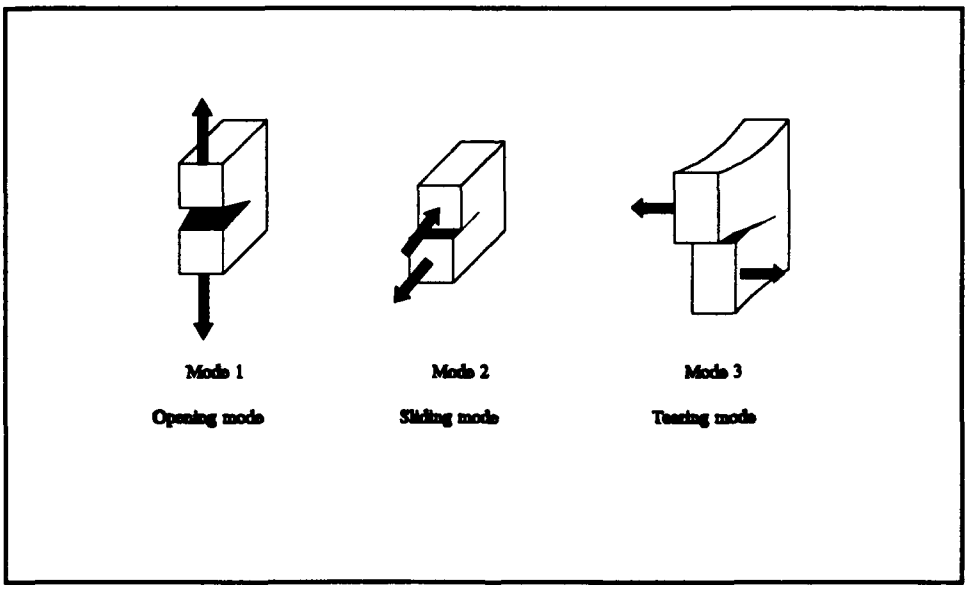

Figure 1.4 Crack displacement modes

Poisson effects produced by the large normal crack-tip stresses cause material immediately in front of the crack periphery to tend to contract (Figure 1.5). However, depending upon the thickness, surrounding material may prevent this contraction. This results in a tri-axial state of stress near the crack tip [1]. This results in a condition of plane strain in the interior of the plate. At the boundary, transverse stresses are zero; creating a region of plane stress. Therefore, the stress state transitions from a state of plane stress at the edges to a state of plane strain in the interior of the material. As mentioned above, K_{1c} is dependent on material thickness. As the thickness is decreased, K_{1c} eventually increases due to a reduction in the number of material imperfections and less restricted motion of slip planes in the plastic region. This apparent increase in toughness may result in a slight concave bowing of the crack front.

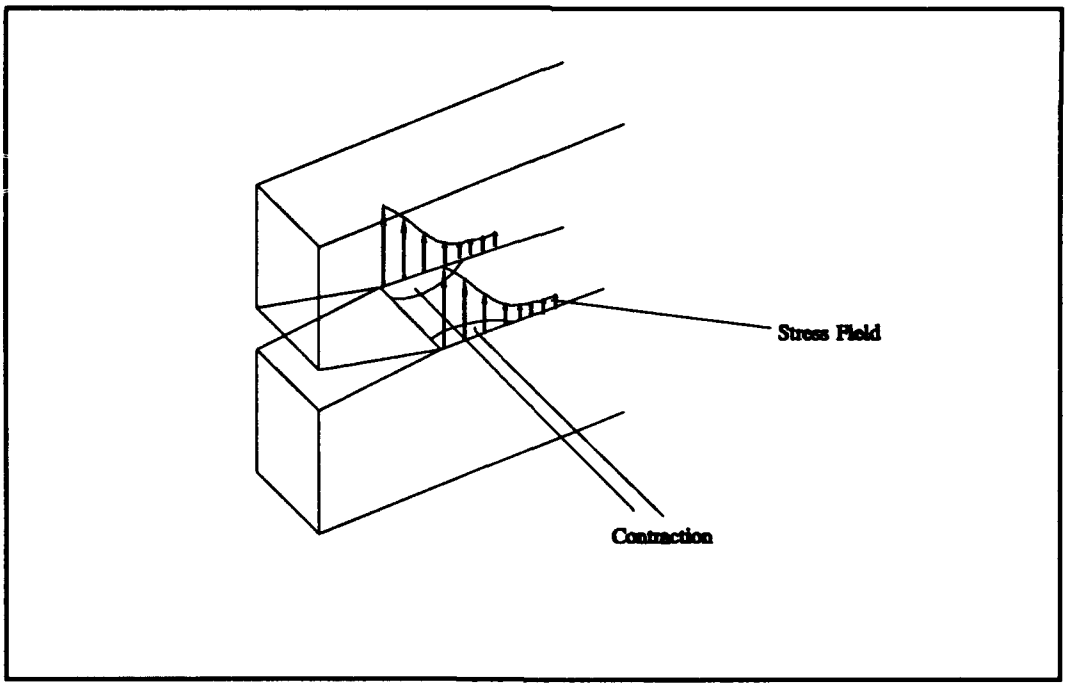

Figure 1.5 Contraction

1.3.1 Fracture in Glass

Pfaender [25] defines a glass to be "all materials which are structurally similar to a liquid but which have a viscosity so great at normal ambient temperatures that they can be considered as solids. In a more limited sense, the term 'glass' denotes all inorganic compounds which possess these basic qualities." Glass is formed through rapid cooling of inorganic oxides creating an "energetically unstable" non-crystalline structure. As such, stress recovery is likely to occur over a prolonged period of time. Uhlmann [31] distinguishes glasses from supercooled liquids by noting that glasses are indeed rigid solids at standard temperatures and that any viscous flow historically reported (e.g. window panes) is likely to be caused by this delayed recovery process.

Although fracture mechanics theory in glass is fairly well established dating back to Griffith's analysis, non-intuitive peculiarities do exist [31]. For instance, plasticity has been reported in glasses. Such deformation is assumed not to influence crack propagation but is worth noting since it may explain reported increases in modulus of glass specimens during testing. This phenomenon is due to inefficient molecular packaging which is forced into more favorable atomic position. Another unexpected finding is that the relative humidity (partial pressures) of the environment plays a significant role in the fracture velocity. Stress corrosion leads to a blunting and strengthening of the crack tip. The reaction may dominate such that velocity becomes independent of the stress intensity. Also, interestingly, that static friction coefficient of glass on glass approaches unity when chemically cleaned [28]. It is the presence of oils, the coefficient may drop to 0.005.

1.4 Crack Growth Near Interfaces

The term "interfacial strength" used throughout this analysis refers to the cohesiveness or "stickiness" of the interface from a Coulomb friction point of view. It is assumed the fiber and matrix are not chemically bonded, and therefore, no true interfacial strength (fracture toughness) is present. The only parameters required to describe the interface reduce to the residual normal stress, σ_R , which may result during processing, and μ, the friction coefficient, such that

$$\tau = \sigma_R * \mu \qquad (1.4.1)$$

Equation (1.4.1) is the standard statement of Coulomb friction. As such, the interface may, therefore, only stick, slip, or open. Larson [19] noted that the extent of slip along an interface decreases dramatically if interfacial toughness is considered. Slip is reduced by about half for a fracture toughness as low as fifteen percent of the driving stress intensity.

The generalized stress fields as depicted in Figure 1.3 precede the crack periphery resulting in interfacial slip and separation. Reduced stress intensities at the crack tip due to the presence of the fiber may result in a convex bowing of the crack periphery.

Conversely, increasing stress intensities produce a concave bowing of the crack front (Figure 1.6). Slip along an interface is the by-product of relative movement between regions undergoing deformation. If the magnitude of the strain gradient is greater than the frictional resistance at the interface, relative movement (slip) results.

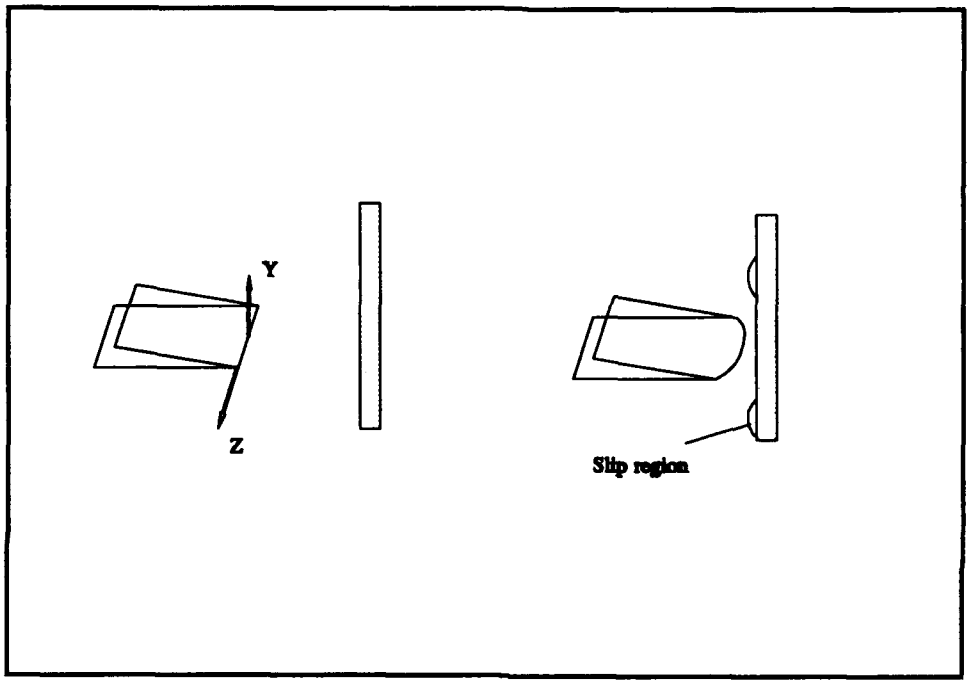

Figure 1.6 Interfacial slip and separation

For the purposes of this analysis, crack growth is assumed to remain perpendicular to an infinitely long planar interface in the two-dimensional case and perpendicular to a cylindrical fiber in the three-dimensional case. The two materials forming the interface are assumed to be the same, and the crack is not allowed to penetrate the interface. Such simplifying assumptions eliminate complex stress intensity formulations (often singular) associated with bi-material interfaces [5].

Interest is focused specifically on the developing slip zone and interfacial separation occurring at the interface. A "Frictional Grab" parameter [19], FG, will be used to characterize the strength of the interface.

$$FG = \mu \frac{\sigma_R}{\sigma_o} \tag{1.4.2}$$

where

σ_r = nominal compression across interface

σ_o = driving stress

μ = friction coefficient

Computational tools are available which can predicted stresses at a planar interface resulting from an approaching crack [5,13,26]. There are a number of codes which describe the behavior of a crack totally engulfing a fiber in which the fiber is usually modelled as a closing traction behind the crack periphery [7]. Larson, however, has developed a fully three-dimensional code capable of predicting stresses and displacements for a crack approaching and growing around a fiber, and as such will be used in this study. Development of the code is discussed in Chapter 3.

1.4.1 Slip Zone Development

Figure 1.7 plots a typical shear stress distribution along an interface due to an approaching crack. Two local maxima predict that slip initiates off the plane of the crack, and even the possibility of a second smaller zone developing. Note that the direction of the shear stresses in the smaller zone are opposite to those in the larger zone. This phenomenon results in opposing interfacial deformations in the two zones (ie. the relative displacements between the fiber and matrix in the larger zone are opposite to those in the smaller zone).

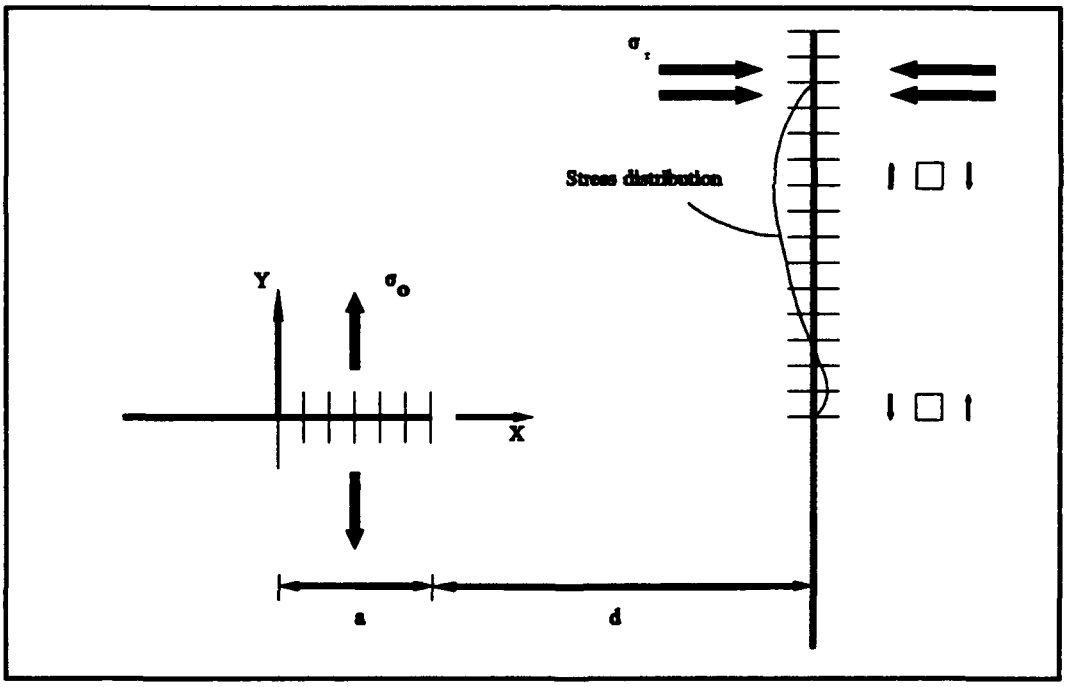

Figure 1.7 Interfacial stress distribution

Figure 1.8 outlines the location, size, and direction of slip for a crack approaching a planar interface. The smaller zone (c-d) will be referred to as the zone of reverse slip. Note that this zone is engulfed by the larger zone (a-b) as d/a $\rightarrow$ 0. Reverse sliding is difficult to conceptualize, but the possibility has not been disproved experimentally. Stress distributions and corresponding displacements illustrating the tendency for the interface to slide prior to crack arrival are included in Appendix A. Figure 1.9 shows the influence of the Frictional Grab parameter on slip initiation. The distance from the crack tip to the interface at which slip initiates and the height above the crack plane at the same point are plotted for several values of Frictional Grab.

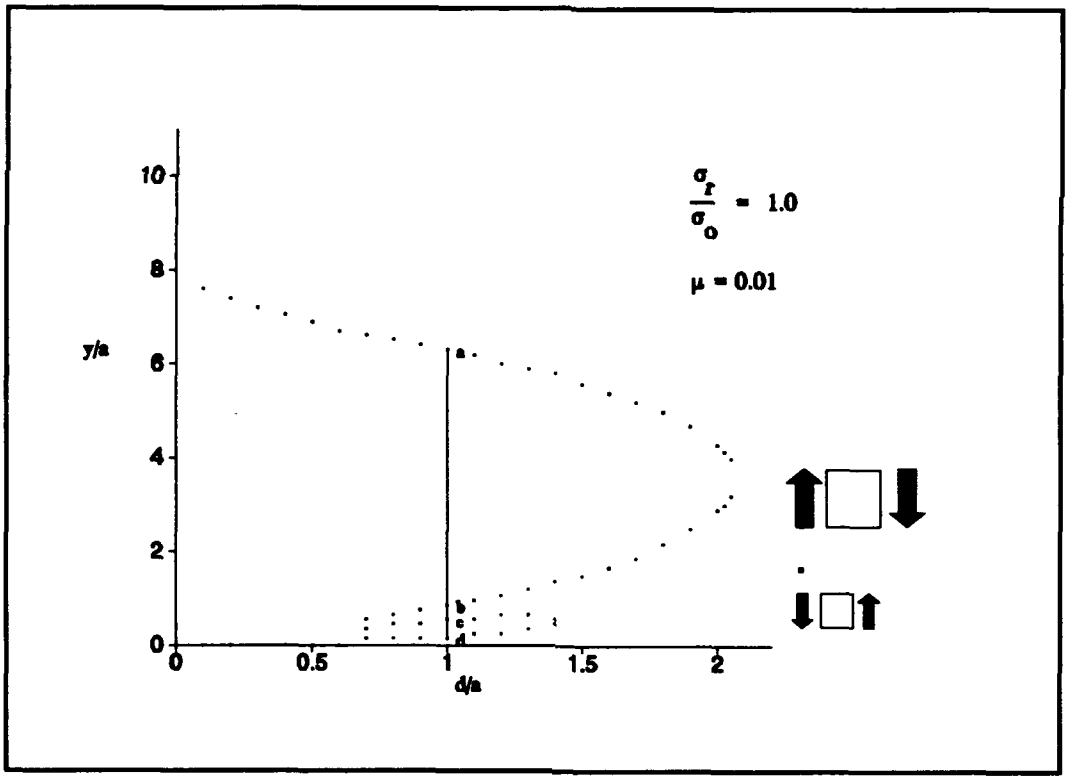

Figure 1.8 Slip zone development

Other investigators have noted the tendency for debonding to occur prior to the main crack reaching the interface. Pan [24] investigated transverse fracture (crack plane parallel to fiber) of three-point bend epoxy specimens with hexagonally-packed, one-millimeter diameter, glass rods used as fibers. Experiments revealed that debonding initiated prior to the main crack reaching the interface. Further, coalescence of secondary cracks, which continually formed ahead of the primary crack promoted further debonding. Fuller [8] also noted similar tendencies in specimens formed by hot pressing SiC (SCS-6) fibers between borosilicate glass plates. Neither study, however, produced distinct observation of the interface during fracture.

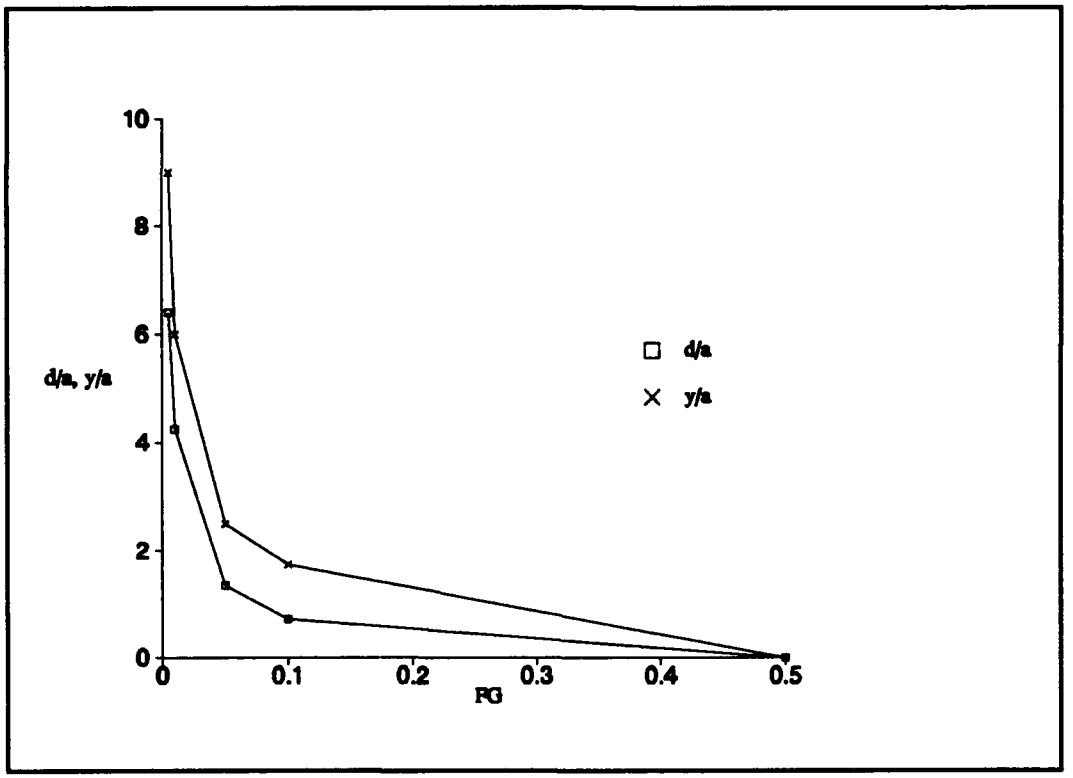

Figure 1.9 Slip Initiation

Knowledge of initiation and development of a slip zone along different cohesive interfaces is important toward quantifying energy dissipation characteristics as an explanation for the variation in the shape and speed of the crack front during growth near and around a fiber. As the crack approaches the interface, local stress intensity values on the crack periphery can increase or decrease depending on the strength of the interface. The weakest interface corresponds to no fiber at all, just a cylindrical hole which acts to increase the matrix crack stress intensity and, hence, increase the propensity for crack growth. At the other end of the spectrum, the strongest interface would occur for a matrix perfectly bonded (i.e. no slip) to a rigid inclusion. Somewhere near this upper bound is a perfect interfacial bond between a fiber and matrix possessing like material properties. This composite would behave as a homogeneous system with the crack propagating as it would through a monolithic medium.

1.5 Numerical Development

The key episode in the fracture of brittle composite materials occurs between the approaching crack periphery and each individual fiber. Recent development of computational tools for analyzing this phenomenon have been restricted to two-dimensional and axisymmetric models whose applicability to the three-dimensional physics of the problem at hand is difficult to assess. The critical parameter is believed to be the amount of energy dissipated through frictional sliding along the interface. Characterization of the resulting stress fields is crucial in defining the equilibrium state

of the body. Larson and Keat [15] have established the effectiveness of the surface integral method for modelling 3-D fractures in infinite regions. The solution is obtained through superposition of known influence functions via boundary collocation. Reference Appendix F for a more comprehensive description of the computational development. The extension to 3-D analyses provides a more representative model of the interfacial energy mechanisms discussed in section 1.2. Prior to this development, bridging fibers were modelled as closing tractions behind the crack periphery [7]. The codes were unable to consider cases where the crack was not engulfing the fiber; nor could they handle fiber debonding or frictional sliding. Larson's development of interfacial stress fields permits both.

CHAPTER 2

EXPERIMENTAL PROCEDURE

This experimental study investigates a brittle fiber - brittle matrix interface in the presence of crack-tip stress fields. Information is gathered on how the shape and speed of the crack front change as the fracture approaches and grows around an inclusion. Growth history is preserved on VHS tape and digitized computer images. Estimates of crack-tip stress intensities, as well as, load versus crack length analyses help quantify toughening as a function of Frictional Grab. The experimental data is compared to computational results in Chapter 4. Fiber debonding is observed during fracture for several interface strengths.

Figure 2.1 is a photograph of one of the fractured glass specimens which was tested. The unfractured template is compressively loaded at the top and bottom surfaces as illustrated by the dark arrows in Figure 2.1. The stress concentrations near the hole cause the glass to fracture, and the crack propagates slowly toward the cylindrical fiber indicated by the astrict (*). The fiber is placed through the center of the template width, one inch above the larger hole such that the fiber is orthogonal to the crack plane. (The

fiber diameter is approximately ten percent of the template width). This particular geometry allows for examination of quasi-static fracture around the cylindrical inclusion. The fiber diameter is kept small relative to the crack length and width in order to investigate localized toughening induced by interfacial energy dissipation mechanisms.

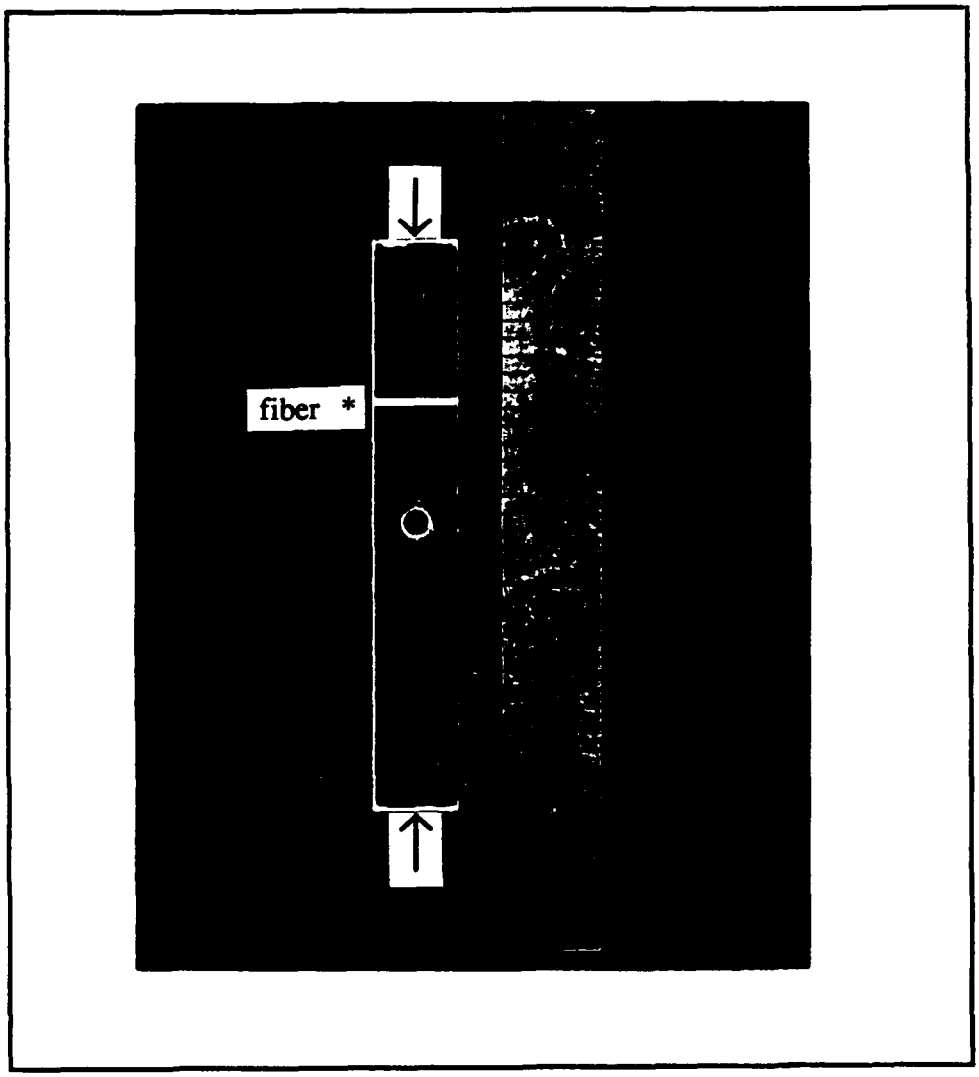

Figure 2.1 Fractured specimen

2.1 Test Specimen

Double Cleavage Drilled Compression test specimens [8] were produced using pyrex templates incorporating several different fibers. Table 2-1 outlines the material properties of each of the constituents. First cut dimensions for the DCDC specimens were calculated to insure fracture prior to geometric buckling failure. This analysis is included in Appendix C. Figure 2.2 shows the typical DCDC dimensions used; however, the dimensions of the specimen and fiber were varied to qualitatively assess how the different parameters influenced the fracture. Increasing the template thickness also prevented cracks from initiating at the fiber hole, but did not alter the load at which crack growth began.

Table 2-1 Material properties*

Material	E (GPA)	υ	α (/°C)	K (Mpa*$m^{1/2}$)
Pyrex	51.0	0.22	32.0e-7	0.83
Epoxy	3.5	0.34	-	1.50

*Material properties were found in reference [1]

As the template is loaded, stress intensities at the large centrally-located hole cause the glass to fracture. Recalling that cracks propagate perpendicular to the maximum tensile stress; bending moments result in the crack propagating orthogonal to the (compressive) loading direction. Stable growth of the crack is achieved after a short period of unstable growth, commonly referred to as pop-in. A stability analysis is included in Appendix B. The crack continues to propagate through the mid-plane of the material, perpendicular to the fiber axis, as outlined in Figure 2.2. Eventually, the system fails catastrophically due to excessive crack length, or growth is arrested due to the presence of the fiber, or the maximum loading capacity is reached. Occasionally growth is retarded as energy available for the creation of new surface area (cracking) is absorbed by other failure mechanisms which begin to dominate the system. The maximum load was limited by the loadcell to 2000 pounds.

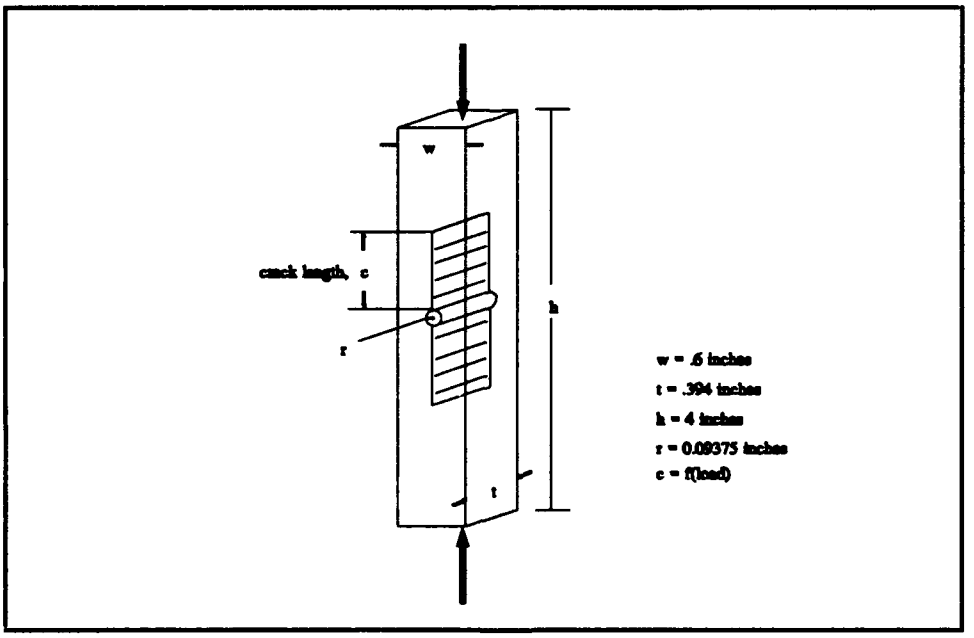

Figure 2.2 Double Cleavage Drilled Compression test specimen

DCDC specimens offer several advantages. They are characterized by a relatively long period of stable crack growth which can easily be controlled. Growth rate remains reasonably constant during constant displacement rate tests. Further, stress relaxation is virtually nonexistent. The test may be held with little or no crack extension*. Certainly, brittle materials exhibit rate-dependent behavior, but for low strain rates, the material is well behaved. (Creep behavior [11] in more viscoelastic materials, such as epoxy, proved detrimental.) If the load is removed, the crack appears to retract. In actuality, the material is of course still cracked, but as the crack opening displacement (COD) is allowed to close, the fracture becomes transparent except at high levels of magnification. This allows for re-examination of the crack "tip" as the load is reapplied. The behavior of the crack propagation when compared to that of the original growth may prove useful in determining failure criteria for fatigued systems.

Other advantages of DCDC specimens are: (1) the crack velocity may be controlled easily over a wide range of speeds which may allow for examination of dynamic affects on crack arrest, (2) crack growth remains on the longitudinal plane of the material, and (3) ease of manufacturing.

---

*Note reference on stress corrosion cracking on page 1-15.

Unfortunately, DCDC specimens must be produced from materials with very low fracture toughness. A considerable amount of time was spent testing epoxy specimens; however, the epoxy proved to be too ductile resulting in plastic deformation and buckling prior to crack initiation at the hole. Variation in strain-rate, temperature, cure ratio, and specimen size proved to be of no help. Pan [24] reported similar findings of considerable plastic deformation during three-point bend tests of epoxy specimens.

2.1.1 Specimen Preparation

Glass templates were purchased from Behm Quartz, Dayton, Ohio. For uniform loading, it proved critical that the edges of the specimen be parallel and the corners be square. "High spots" were found to be the greatest obstacle during testing, often resulting in catastrophic failure in shear. Behm was able to alleviate the problem through precise milling of the edges.

Two holes were introduced into the glass plate using the Sheffield ultra-sonic drill pictured in Figure 2.3. The crack initiates at the larger 0.1875 inch diameter hole located at the center of the specimen. The second smaller hole, drilled through the width of the template, held the fiber as described in Appendix D. The hole diameter was approximately 0.05 inches. The templates were similar to those used by Fuller [8] which he termed Double Cleavage Drilled Compression (DCDC) test specimens.

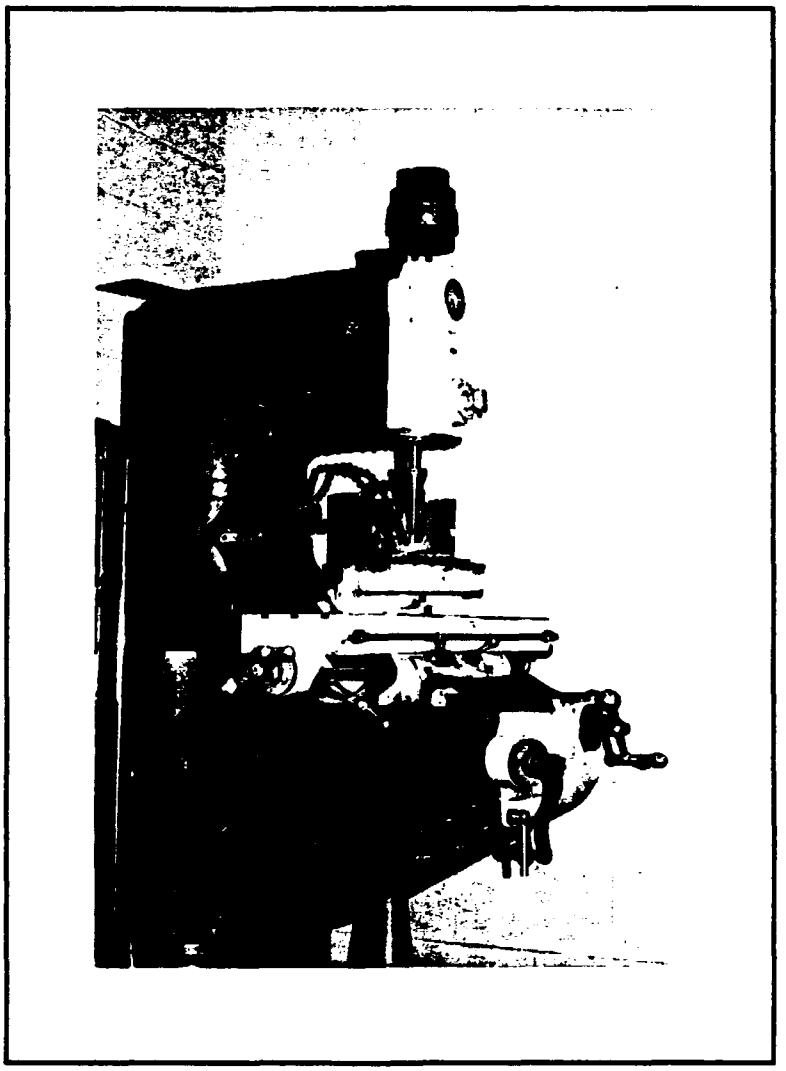

Figure 2.3 Ultrasonic drill

Prior to drilling, the templates were hot waxed between a 0.25 inch base plate and 0.0625 inch guide plate (Figure 2.4). The ultrasonic drill operates by vibrating a steel bit at or near a resonant frequency of the glass. Upon reaching the key frequency, the drill pulverizes its way through the material. A liquid abrasive is continually sprayed on the

bit to aid in drilling. Approximately 20% of the templates fractured as the bit exited the glass. Sandwiching the templates between the base plate and guide plate reduced the damage and produced less variation in hole diameter through the thickness of the specimen.

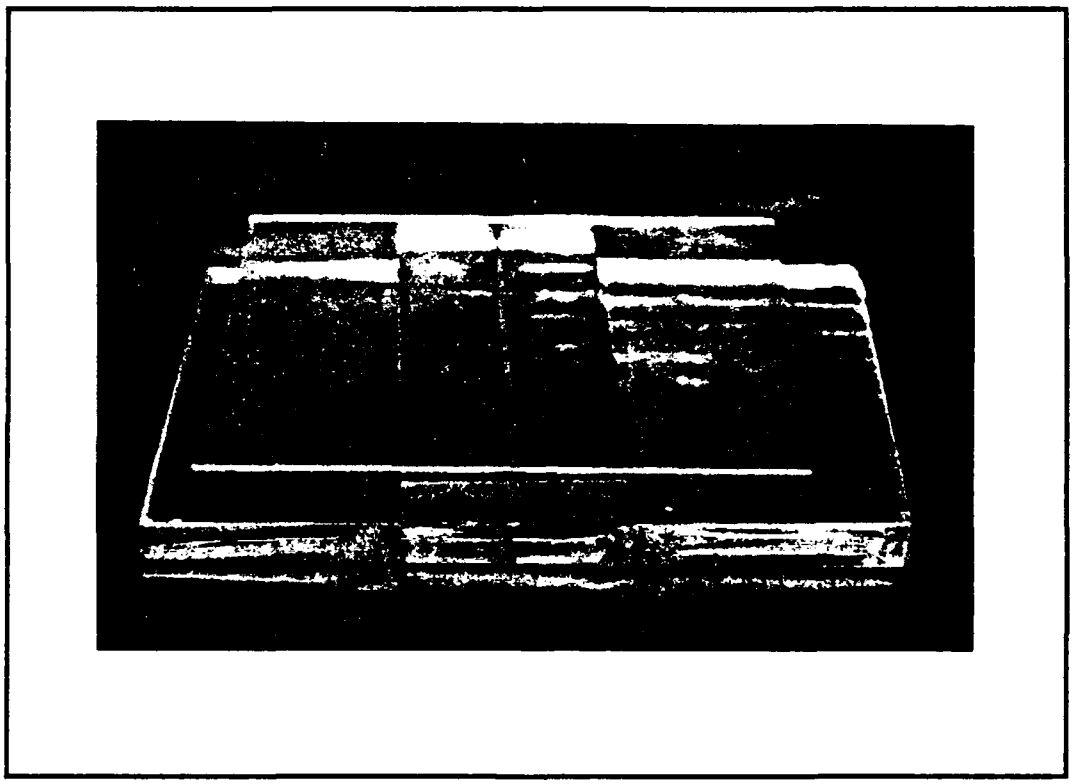

Figure 2.4 Two specimens sandwiched between two glass plates in preparation for drilling

Towards the later stages of this research, diamond-tipped drill bits were used to bore holes into the templates. This method resulted in a cleaner hold with much less effort, but was more expensive. The hole, however, proved to be "too smooth" requiring that a starter-notch be filed to prevent excessive pop-in lengths.

After drilling, the specimens were cleaned with acetone, and prepared for polishing. The templates were manufactured from a large piece of plate glass and had a single rough edge from being cut. The jagged edge reflected light back into the video camera degrading the quality of the image. To reduce this problem, the edge was ground using silicon carbide paper and polished using a special rouge purchased from the Ohio State University College of Optometry.

2.2 Test Setup

Constant displacement tests at a rate of 0.002 inches per minute were conducted on a United model SFM test system. A video camera was used to record crack propagation and interfacial slip. The crack length was measured visually, and the load was audibly recorded on the VHS tape using a microphone. Figures 2.5 through 2.7 illustrate the test setup used.

2.2.1 Digitization of Crack Front

Twenty-four bit digital imaging techniques were used to capture frames off the half-inch VHS tape. Computerized filtering of the images enhanced visualization of the crack periphery. Three consecutive frames from the VHS tape were averaged to reduce any blurring which may have existed on any single frame. Each image consists of approximately 720 bytes of data. These images are included in Appendix E.

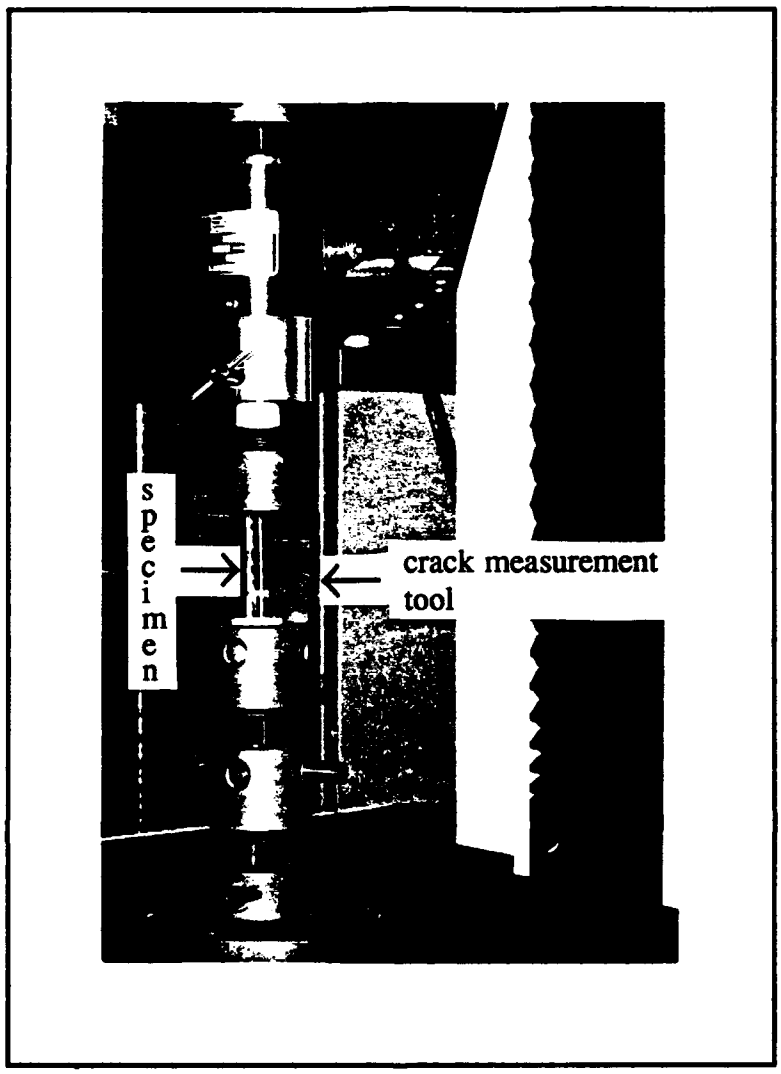

Figure 2.5 Test setup

2.3 Test Plan

The Frictional Grab parameter describing the cohesiveness of the interface was varied by incorporating both glass and epoxy fibers with and without coatings to weaken the interface. Epoxy fibers were formed by curing the fiber in the existing hole. Glass rods were introduced into the smaller hole using standard shrink fitting techniques. The

glass rods were drawn down to just larger than the diameter of the fiber hole; the matrix was than heated; the fiber was placed into the hole, and the matrix was allowed to cool around the specimen. This procedure created strong residual compressive stresses. The cohesiveness of these interfaces was varied using different release agents. Silicone spray was used with the epoxy fibers and motor oil with the glass fibers. Interfacial strength was estimated using the procedures which are outlined in Appendix D. Table 2-2 (page 2-13) lists a few of the typical tests which were conducted. A large number of tests were conducted with epoxy DCDC specimens. All of the templates failed due to buckling. These tests and a number trials using glass as the matrix material were all part of a large learning curve.

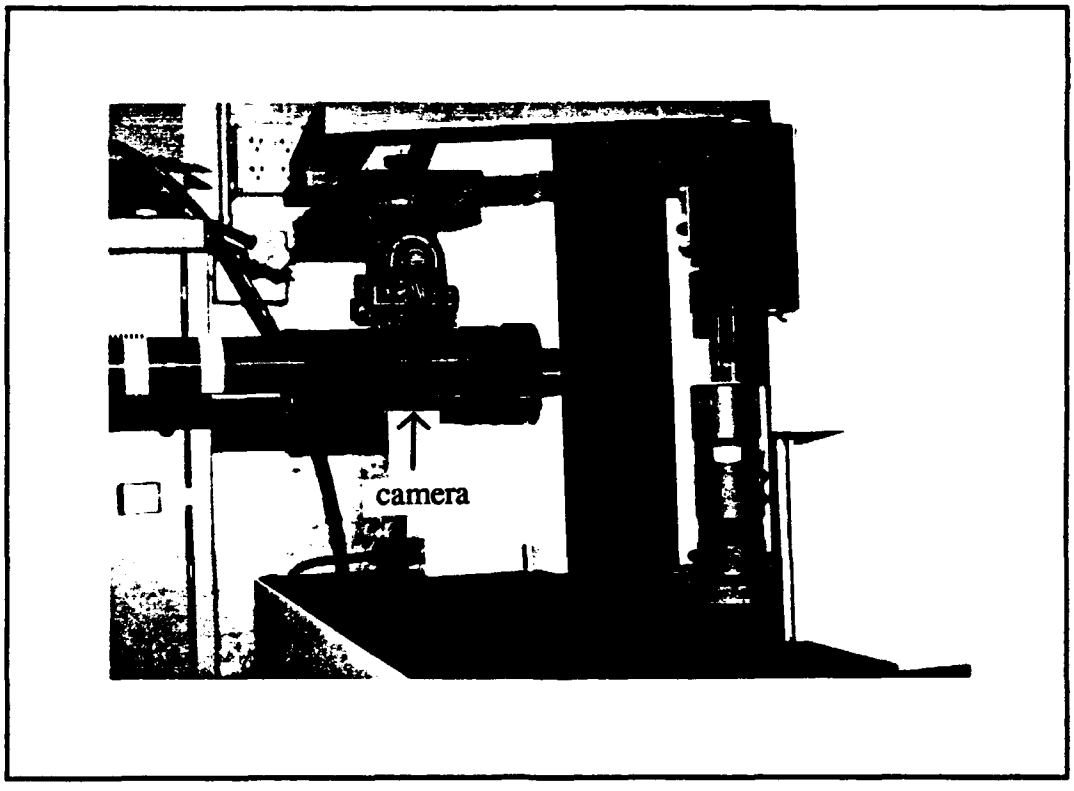

Figure 2.6 Test setup

Figure 2.7 Test setup

Table 2-2 Successful compression tests using DCDC specimens

Parameter / Test	Fiber*	View**	Media***
01	nf	a	v, d
02	h	a, ac, t	v, d
03	e	a, ac, t	v, d
04	es	a, ac, t	v
05	p	a, ac, t	v, d
06	po	a, ac, t	v

*Fiber: (nf) no fiber; (h) hole; (e) epoxy; (p) pyrex; (es) epoxy with silicone coating; (po) pyrex fiber with oil coating

**View: (a) fiber axis; (ac) close-up along fiber axis; (t) transverse fiber axis Note: only one camera was available; therefore, each view required a separate test.

***Media: (v) VHS tape; (d) digitized computer images

CHAPTER 3

COMPUTATIONAL PROCEDURE

Solutions to fracture mechanics problems may be obtained using surface integral techniques, often with less difficulty than if conventional methods are employed. Surface integral formulations are a direct extension from common indirect boundary element techniques which yield elasticity solutions to fracture mechanics problems through integration of fundamental singular solutions across the crack boundary*. Crack-tip displacements are estimated by singular kernels of an integral equation from which the elastic solution in obtained [23]. Two codes capable of investigating two and three dimensional crack growth near an interface are reviewed. Appendix F outlines indirect boundary element procedures as applied to linear elastic fracture mechanics.

*In contrast to direct boundary element formulations which are based on the reciprocal work theorem which states that "if two distinct elastic equilibrium states exist in a region, V, bounded by the surface, S, than the work done by the forces of the first system on the displacements of the second is equal to the work done by the forces of the second system on the displacements of the first." [9]

3.1 Surface Integral Techniques

Although finite element methods are standard for solving many elasticity problems, the problem at hand is solved with considerably less work and computational time using surface integral techniques [9]. These methods are appealing since only surfaces, not volumes, need to be discretized. Consider, as an example, a crack in an arbitrary body. The "crack", in reality, is simply the open space between two free surfaces. The surface integral method requires that only this surface be discretized with two-dimensional elements. Finite element codes, on the other hand, require that the entire volume be discretized as an assemblage of three-dimensional elements. For each increment of crack growth, the entire *volume* would need to be remeshed. Such an approach is impractical. Surface integral formulations only require that the *crack surface* be remeshed as the crack propagates. Surface integral techniques; however, produce fully-populated (not banded) matrices which increase the computational time required for the given degrees of freedom.

3.2 Crack Growth Applications

The following discussion outlines the general methodology incorporated in the two crack growth codes used in this study. The two-dimensional case will be examined, but note that the same approach is used in the three-dimensional case.

3.2.1 Assumptions and Limitations

Computational analysis of crack propagation near and around frictional interfaces is accomplished. The primary interest being the development of frictional slip zones at the interface, and how this sliding affects crack growth. As previously discussed, a myriad of variables influence fracture near interfaces. It is impractical, if not impossible, to study how all these parameters influence growth individually; not to mention any coupling which occurs. This study assumes that the primary variable describing crack growth around an interface is based on friction considerations, and can be characterized by a single parameter known as the Frictional Grab (FG).

The system modelled in this analysis consists of an internally pressurized* crack approaching a single fiber or planar interface. Both the fiber and matrix are assumed to be made of the same material.** This is consistent with aforementioned assumptions, and allows specific examination of frictional mechanisms. In this case, the material is glass. Table 2-1 lists material properties for the constituents used in this study.

---

* For LEFM theory, stress intensities are equivalent in the case of an internally pressurized crack as for an applied far-field stress at boundaries.

** The constituents of CMCs are often composed of materials having similar material properties. It is therefore assumed that since interest in frictional considerations is the primary focus, allowing the fiber and matrix to be of the same material does not produce any ill results [19].

Three-dimensional computational examination of crack growth around bi-material interfaces is an extremely difficult problem, and to my knowledge has not been accomplished. Consideration of only a single fiber is adequate for modelling very small matrix cracks indicative of those which initially form. Maximum toughening will occur if these cracks can be arrested before they reach a critical length where unstable growth may occur. Appendix B addresses stability issues.

In this symmetric geometry, the crack remains orthogonal to the interface; eliminating the need for a complex crack growth law to determine the direction the crack periphery would move. The interface is assumed void-free with no fracture toughness. In reality, of course, interfaces are prone to imperfections and to some extent mechanical interlocking, but since the length of the slip zone is small relative to major imperfections, we assume the interface is smooth.

3.2.2 General Solution

The following is a summary of the methodology behind the development of the two codes written by Larson [19].

Kelvin [21] derived the fundamental solution for the stresses induced by a point force in an infinite medium. The solution has the form

$$\sigma_{ij} = c \frac{1}{|R^3|} f(R) \qquad (3.2.1)$$

where R is a vector originating at the location of the point force and extending to a point of interest.

A force dipole is created in the limit as two opposing point forces converge as shown in Figure 3.1. A new fundamental singular solution, f(δ,x,y,z), describing the stresses induced by the dipole at any point, a, is formed.

The strength of the singularity is characterized by the strength of the dipole. The dipole represents a point of infinite strain, or equivalently, a finite displacement between two infinitesimal surfaces (a hole).

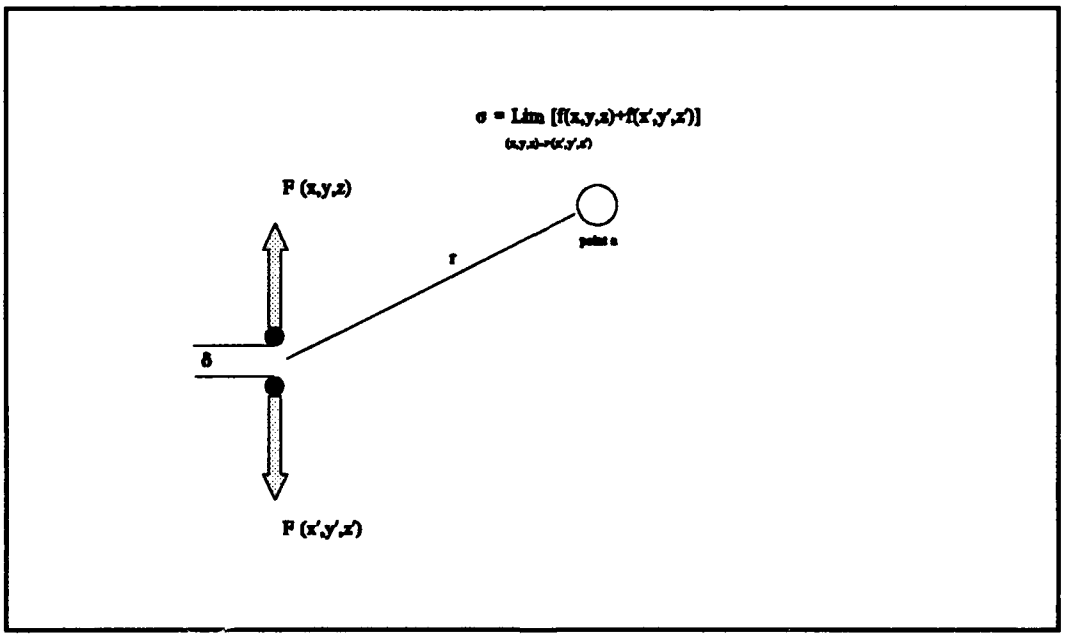

Figure 3.1 Force dipole

The crack and interface are discretized into elements comprising a continuous distribution of dipoles. For the general three-dimensional case, plane strain considerations are maintained through the addition of two other continuous distributions of dipoles acting in the two remaining axial directions to remove any Poisson contractions which may occur. Elements are defined by three or four geometric nodes* and include a single structural node (collocation point**) centered in the element where the nodal degrees of freedom (dof) are calculated. Typical meshes for a crack impinging on a fiber are illustrated in Figures 3.2 and 3.3.

---

* Higher order elements are used at the crack tip in order to capture complex stress gradients.

** Point at which boundary conditions are exactly satisfied. Since it is the applied stresses, not the crack opening, δ, which is defined, the surface integral technique seeks to satisfy the prescribed boundary condition at a single collocation point for each element by determining the required strength of the singularity such that when superimposed the boundary condition is exactly satisfied at the collocation point.

The elastic solution is found by solving

$$\bar{\sigma} = [C]\ \bar{\delta} \tag{3.2.2}$$

where [C] is a matrix of influence coefficients satisfying Equation (3.2.1). The singularity in the fundamental solution localizes the influence of δ to a single point (collocation point), and we can therefore assume that the elements along the crack plane have a constant opening over their length. With this assumption, the fundamental solution becomes a function of only the relative position between the collocation point of interest and continuous distribution of dipoles on any given element. Opening along crack-tip elements are defined by interpolation functions since they must be closed at one end and have a finite opening value at the other. These elements require special handling since $\delta=\delta(r)$. The approach is discussed later in this section.

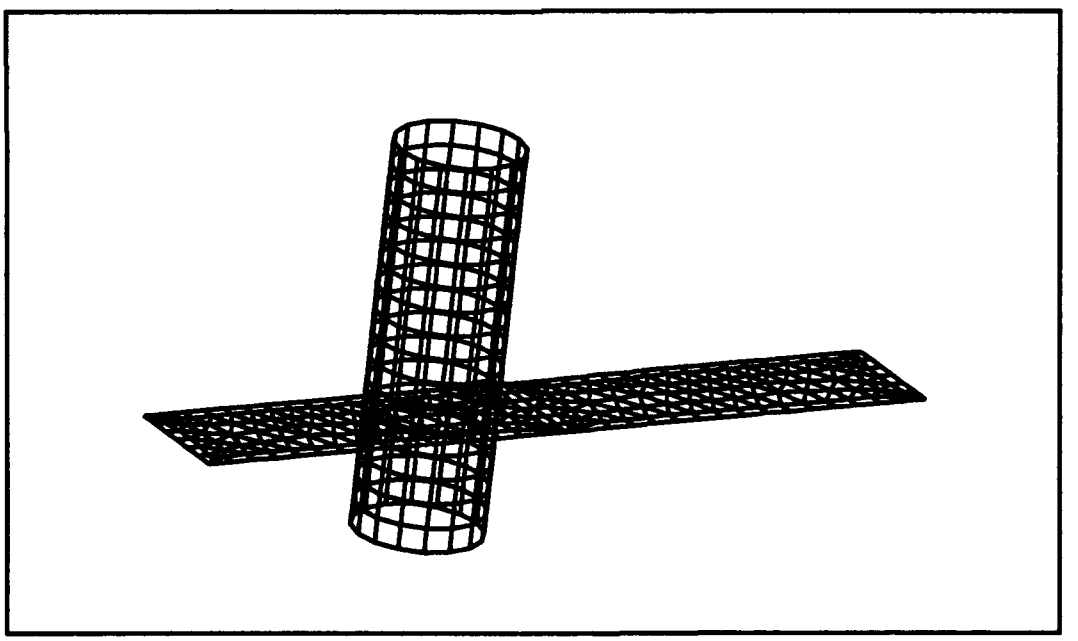

Figure 3.2 Three-dimensional boundary elements for the fracture approaching a fiber

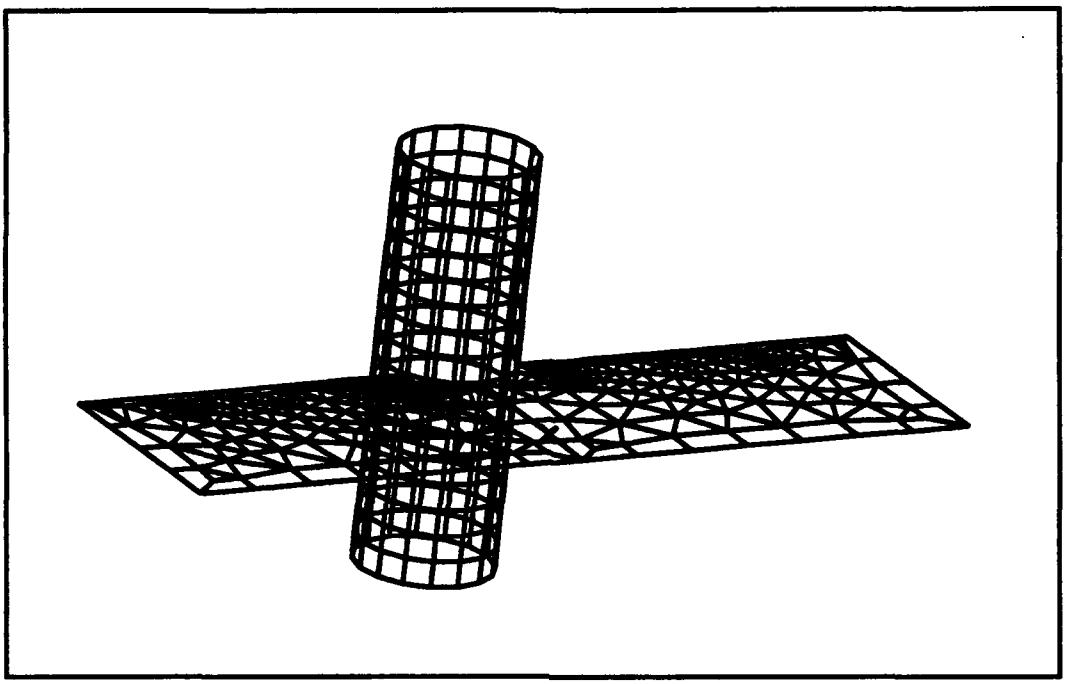

Figure 3.3 Three-dimensional boundary elements for the fracture impinging on a fiber

Once the crack and the interface have been discretized into elements consisting of a single collocation point and a continuous distribution of dipoles, the elements of the [C] matrix are determined by calculating the influence of every dipole on any given collocation point. Therefore, to determine the influence on any one element due to the dipoles on any other element, we simply integrate the derived fundamental solution over the area of the element taking into account the vector between the two points. For a typical one-dimensional isoparametric element referenced in a natural coordinate system, ξ, the elasticity solution becomes

$$\tau = \delta \int_{-1}^{1} f(x,y,z)\, d\xi \tag{3.2.3}$$

The integration is performed numerically by Gauss Qaudrature [6]. Tractions are related to stresses through Cauchy's law shown below.

$$t_i = \sigma_{ij}\, n_j \tag{3.2.4}$$

Two instances exist where the above equation is not valid: (1) crack-tip elements where $\delta=\delta(r)$, and (2) when investigating the influence of the dipoles coincident with the collocation point of interest. Fortunately, a mathematical manipulation, equivalent to imposing a rigid body motion, results in a solution. Adding and subtracting

$$\int_{-\infty}^{\infty} f(x,y,x)\, \delta_2\, d\xi \tag{3.2.5}$$

where δ_2 is the crack opening at the collocation point, results in an equation, although still singular, is integrable by Cauchy's Principal Value Theorem.* Figures 3.4 (a) and (b) illustrate the singularity transformation.

---

*Cauchy's Principal Value (pr. v.) Theorem is based on the residue integration theory [18] which develops techniques for integrating analytic functions around closed contours. The Principal Value Theorem handles definite integrals whose integrand becomes infinite at a point ρ in the interval of integration. The theorem states that

$$pr.v. \int_A^B f(x)dx = \lim_{\epsilon \to 0} \left[\int_A^{\rho-\epsilon} f(x)dx + \int_{\rho+\epsilon}^B f(x)dx \right]$$

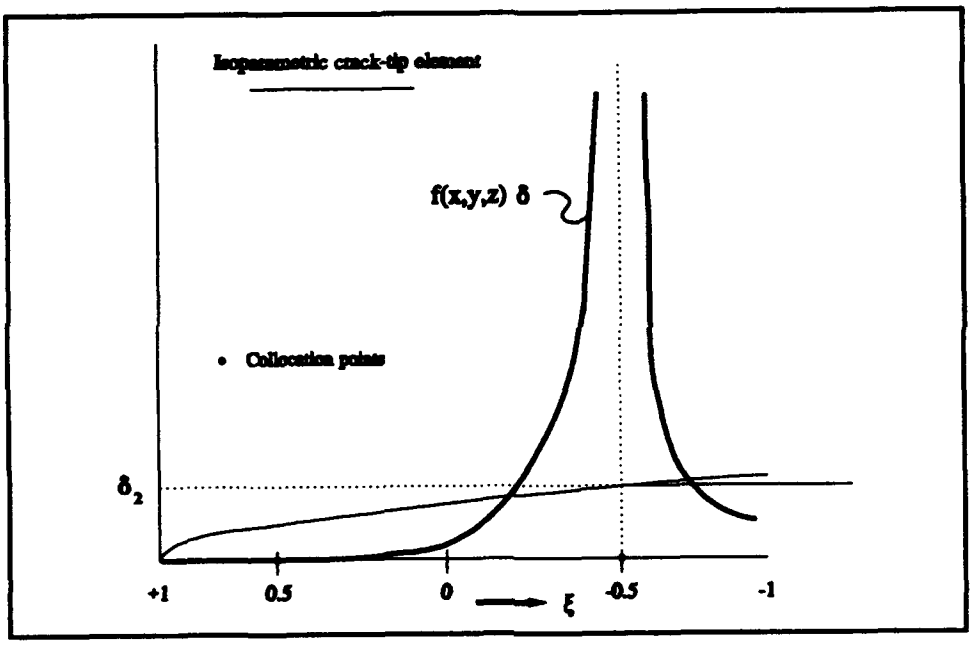

Figure 3.4 (a) Typical form of an elemental singular integral

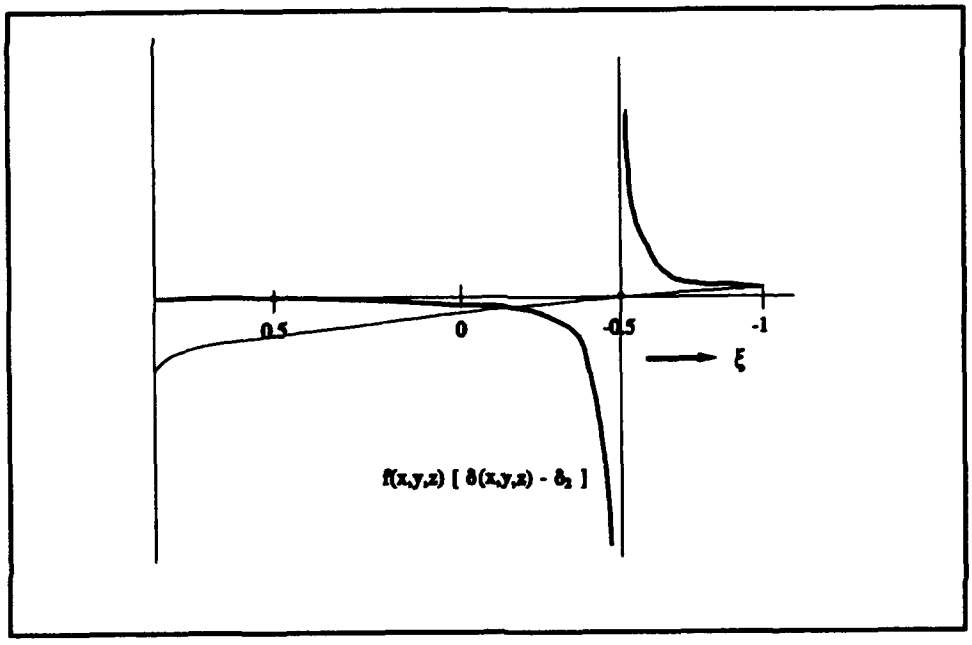

Figure 3.4 (b) Modified singular integration for Cauchy Principal Value

The final form of the solution becomes

$$\tau = \int_{-1}^{1} f(x,y,z)\,[\delta(r) - \delta_2]\,d\xi - \int_{-\infty}^{-1} f(x,y,z)\,\delta_2\,d\xi - \int_{1}^{\infty} f(x,y,z)\,\delta_2\,d\xi + \int_{-\infty}^{\infty} f(x,y,z)\,\delta_2\,d\xi \tag{3.2.6}$$

Solutions to the first term are found using Cauchy's Theorem. The second and third term are evaluated directly, and the last term is ignored since it is associated with a rigid body displacement and does not alter the stress within the system.

Once the influence coefficient matrix has been determined based upon the current geometry of the model, the problem may be solved. Initially, all displacements on the interface are assumed zero and the only prescribed boundary condition is the uniform pressure associated with the crack. Partitioning of Equation (3.2.2) allows solution of unknown displacement on the crack and unknown stresses upon the interface. Stresses at the interface are determined using Equation (1.4.1). If the shear stress is less than the normal stress times the friction coefficient, the stress at the interface is set equal to the value of the shear stress and the interface does not displace. If the shear stress is greater than the product of the normal stress and friction coefficient, then the shear is set equal to the value of the normal stress times the friction coefficient and the interface slips. If the normal tractions are greater than the initial compressive stress, the interface is allowed to open and the shear stress is set equal to zero. Given these stresses, displacements are solved by again applying Equation (3.2.2). Once the displacements are known, new

stresses are calculated, and the procedure is repeated until equilibrium is reached. The final solution is determined through n iterations applying tractions of p/n on the crack plane at each increment. Note that as in other linearized elasticity solutions, displacements are assumed to be small such that the original geometry is not altered. Reference Appendix F for a more comprehensive discussion of the theory behind the three-dimensional code incorporated in this study.

CHAPTER 4

RESULTS

Observation of non-homogenous fracture provides evidence of localized toughening resulting from cylindrical inclusions in a brittle matrix. Variations in crack propagation rates define the impact of interfacial strength on matrix toughening. Further, as stress intensity values vary across the crack periphery, the shape of the crack front is altered since variations in K effect the propensity to grow. This phenomenon, as well as the development of slip and debonding regions during fracture, is recorded for several interfacial strengths. Experimental data are compared with computational results.

4.1 Preface

The primary focus of this study is an experimental examination of quasi-static fracture in a brittle composite system. Currently, limited information exists regarding the physics of a crack approaching and enveloping an inclusion. Fuller [8] published data tracking stable crack growth around an inclusion using acoustic wave techniques to follow the crack periphery. Although information on the position and speed of the crack front

is presented, Fuller's data is limited and failed to visualize specific crack - fiber interactions.

Since a solid foundation to compare either experimental or computational results does not exist, this analysis is presented as a starting block from which speculation can be resolved and further experiments designed. Certainly, all variables cannot be accounted for in a single experiment. As an example, the disparity between the modulus of elasticity of the constituents may play an important role during fracture. For cases where the materials are tightly bonded or have large friction coefficients, the modulus is certainly important. However, for weak interfaces (which is desired in ceramic matrix composites), interfacial slip will influence the compliance near the fiber to a greater extent than will differences between the elastic modulus of the fiber and the matrix, especially in ceramic matrix composites which have constituents with similar mechanical properties.

More information needs to be gathered in order to base crack growth laws on physical mechanisms as is evidenced by the use of empirical rules for dynamic and fatigue growth (e.g. Paris Law) [1,4]. To make a one-to-one correlation between the computational and experimental results is not feasible since no true physical law has been identified which defines the propensity of the crack to advance. The quasi-static growth being modelled here might seem to be a straightforward application of static fracture methods through time, yet questions remain unresolved for the three-dimensional fracture

analysis. Larson assumes that brittle fractures proceed in proportion to the local stress intensity values. (In contrast to global energy considerations.) Computationally, stress intensities at discrete nodal coordinates may be determined across the crack front. Suppose, however, the analysis determines that K at one node is greater than K_{Ic}, but is below this critical value at the two surrounding nodes. Would the crack advance? If so, how far, and what do we do with the adjacent nodes? In reality, K is never greater than K_{Ic}, but to a computer, they are both merely numbers. Further, how should the solution be affected by changes in crack length and model geometry. This work will provide guidance in determining an appropriate computational criterion. It is assumed that the specific boundary condition which produces the driving stress is unimportant, and that valid comparisons can be made between computational and experimental data since growth occurs when K reaches K_{Ic} for both cases. Computationally, each node advances perpendicularly to a tangent drawn parallel to the radius of curvature at the given coordinate. The distance the node advances is proportional to the value of its stress intensity normalized with the average stress intensity at a point along the crack front far away from the influence of the inclusion or edge (Figure 4.1).

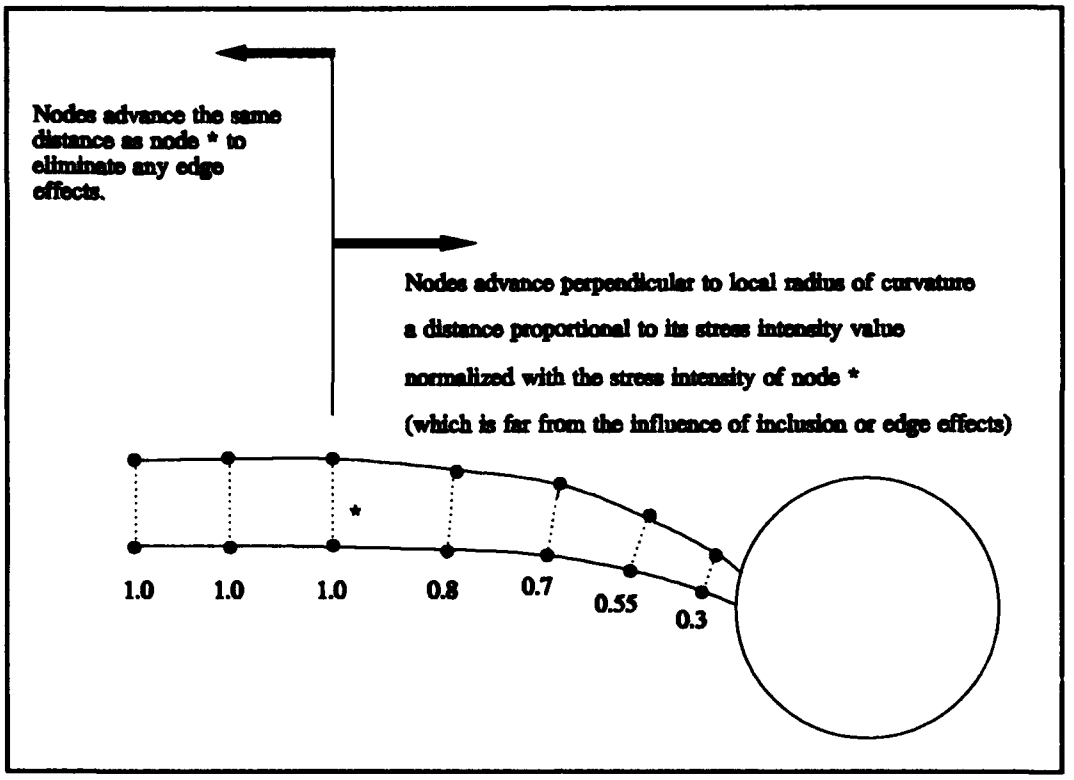

Figure 4.1 Crack advancement

4.2 Experimental Results

4.2.1 Effective Toughening

The propensity for crack growth is proportional to the magnitude of the stress intensity value at the crack tip. Once K reaches K_{Ic}, the crack propagates. During fracture through the homogenous region of the specimen, variations in K across the crack periphery can be neglected which results in a flat* crack front.

*The front of the crack plane is flat and perpendicular to loading axis.

The shape of the crack front shown in Figure E1 (Appendix E) shows that this assumption is reasonable. Any curvature of the crack front (far from the inclusion) may be attributed to the transition between a state of plane strain to plane stress as discussed in chapter one. Fractures far away from fiber influence maintain their initial shape since K is constant across the crack front. As the crack approaches the inclusion, variations in stress intensity values alter the general shape of the crack periphery. Thus changes in the shape of the fracture indicate the degree of matrix toughening.

During constant-displacement testing, the load increases continually until fracture occurs. At this moment, K is equal to K_{1c}. As the crack extends an incremental length, da, some load is relieved, but since testing continues, the load increases until K once again equals K_{1c} and the crack extends further. The energy placed into the system is consumed by two primary mechanisms. A portion of the energy drives the crack; the remaining energy is stored as strain (elastic) energy in the body. Depending on any non-uniformities in loading or geometry, the percentage of energy contributing to each of these mechanisms will vary. Given two specimens with exactly the same geometry and loading, the crack length will be the same for any given load. (Pop-in length will vary accordingly.) However, if the center hole is drilled off-center, or if the loading is somewhat eccentric than the crack length for the same load will differ between the two specimens since less (more) energy is stored within the body. Comparing the load at which the fractures initiated revealed that the disparity between equivalent specimens was around seven percent. This is certainly acceptable; however, to account for this variation

for purposes of comparing the toughening which resulted from the introduction of fibers into the matrix, the load at which the crack initiates is initialized. A typical load versus crack length curve for a DCDC specimen has a positive slope signifying the fact that energy is being stored within the body, and also due to the fact that the crack is propagating into a diminishing mode I stress field, and therefore, the load must continue to increase for an equivalent stress intensity value to be maintained. Figure 4.2 illustrates the local toughening phenomenon which takes place due to the introduction of the fiber. The effective toughening can be determined by drawing a vertical line to the right of the fiber and calculating the additional load required for an equivalent crack length. Note that the crack propagates at a constant rate. This is to be expected since constant displacement tests are being performed and K_{Ic} is constant. Computationally, discrete stress intensity values along the crack periphery are calculated; therefore, if the variation in the shape of the crack front compares well with experimental results than the localized toughening phenomenon has been adequately simulated.

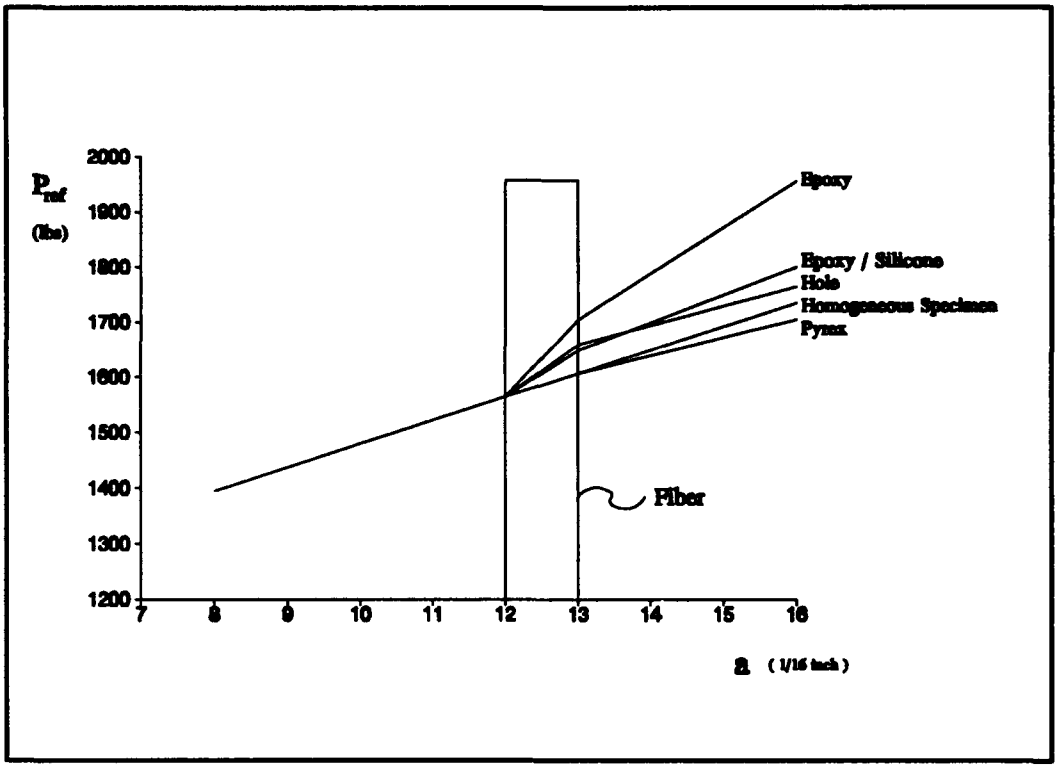

Figure 4.2 Experimentally derived load versus crack length curves for several DCDC specimens

4.2.1.1 Fiber: Hole

As the crack approaches the free surface of the hole, local stress intensities increase and the periphery dynamically snaps into the hole. As the crack continues around the hole, growth is retarded since the periphery must not only advance forward but also propagate along the circumference of the hole diameter. Figures E2 through E5 and Figure E9 (Appendix E) show the sequence as the crack propagates around the hole. An increase in toughening is calculated by determining the percent increase in load

required for the fracture to reach a reference half-crack length of one inch. Using a hole as the fiber, the additional load required was found to be 2.6 percent greater than in the homogenous case.

4.2.1.2 Fiber: Epoxy

The addition of epoxy fibers into the glass matrix proved to be the most beneficial requiring a 13 percent increase in load for the fracture to reach the reference length. This dramatic increase supports the theory outlined earlier. The interface for this case is relatively weak with large amounts of debonding and frictional slip occurring before and after arrival of the main crack (Figures E12 through E14). The energy dissipated through these mechanisms is instrumental for the toughening phenomenon. Note that these results were determined using a fiber diameter equal to 16 percent of the specimen width. Fiber widths on the order of 30 percent of the specimen width were able to completely arrest the fracture (maximum load applied was 2000 pounds.)

4.2.1.3 Fiber: Epoxy and Silicone Spray

The addition of silicone spray along the interface reduced the percentage of toughening from 13 to 3.75 percent. The large variation is attributed to (greatly) reduced energy dissipation which results from frictional sliding along the interface. The silicone eliminates the mechanical interlocking which would normally occur along the interface.

4.2.1.4 Fiber: Glass

DCDC specimens with glass fibers proved to be the most inconsistent during testing. The problems are attributed to the manufacturing procedure used to introduce the fibers into the matrix. Both the fiber hole and the glass fibers are slightly tapered; however, the taper ratio of the two are certainly different. The manufacturing procedure involved quickly forcing a small, brittle rod into a matrix which was heated to around 1000 °F. Since glass dissipates heat rapidly, the matrix had to be removed from the oven, and the fiber inserted and forced down before the hole shrunk back to its original size. On top of all this, there was no guarantee that the fiber and matrix fit snugly together over the length of the fiber.

Of the five pyrex fiber-matrix templates, two recorded slight increases in toughening; two recorded slight decreases in toughening, and one behaved as a homogenous system. Based on experience gained during manufacturing and testing of the specimens, it is believed that the increases in toughening resulted from fibers which were not well bonded. On the other hand, for the strong interfaces in the remaining three templates, the crack-tip stresses were transferred across the interface and the fracture was not altered, or even worse the residual tensile stresses in the matrix* actually increased the stress intensity along the crack periphery.

---

* For compressive interfaces, residual tensile stresses are produced in the matrix in order to satisfy equilibrium.

4.2.1.5 Fiber: Glass and Oil

The addition of motor oil to the interface did not appear to alter the results from the above case (glass fiber - no oil). This is due primarily to the fact that most (if not all) of the oil evaporated due to the intense heat of the matrix during manufacturing.

4.2.1.6 Variation in Crack-Periphery Shape

Figures 4.3 through 4.5 illustrate the general shape of the crack periphery as it proceeds around the inclusion. These figures were obtained by tracing the shape off of a monitor. The arrows denote the direction of crack propagation. Actual digitized images of the periphery are included in Figures E9 through E11 (Appendix E). As expected, weaker interfaces produced more toughening than tight interfaces since energy required for propagation was consumed through frictional slip. The behavior of the fracture near the various inclusions confirms expectations of the workings of the various interfacial mechanisms. Crack-tip stress fields are easily transferred across very cohesive interfaces resulting in limited toughening; limited slip and separation, and limited variations in periphery shape. On the other hand, relatively weak interfaces permit apparent crack-interface interactions.

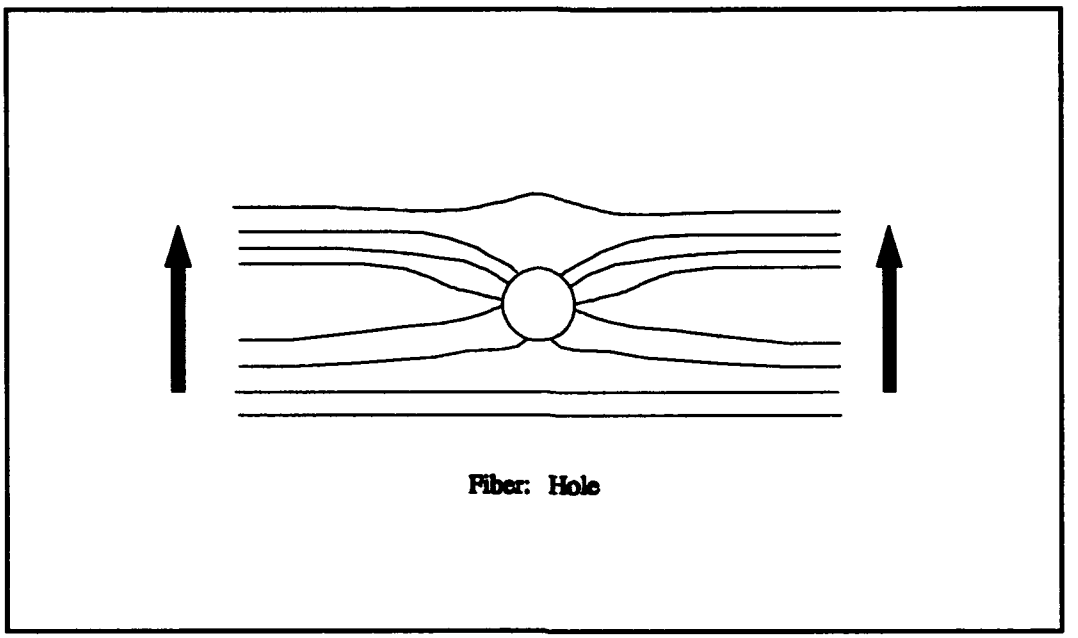

Figure 4.3 Crack-front profiles for a crack propagating around a hole
Arrows indicate the direction of crack propagation

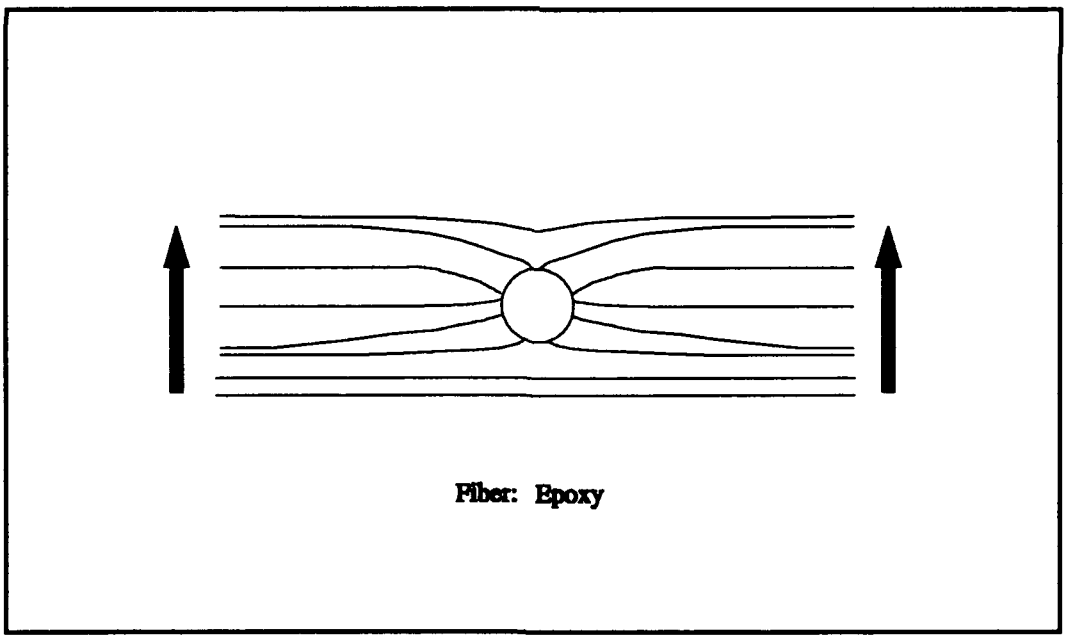

Figure 4.4 Crack-front profiles for a crack propagating around an epoxy fiber
Arrows indicate the direction of crack propagation

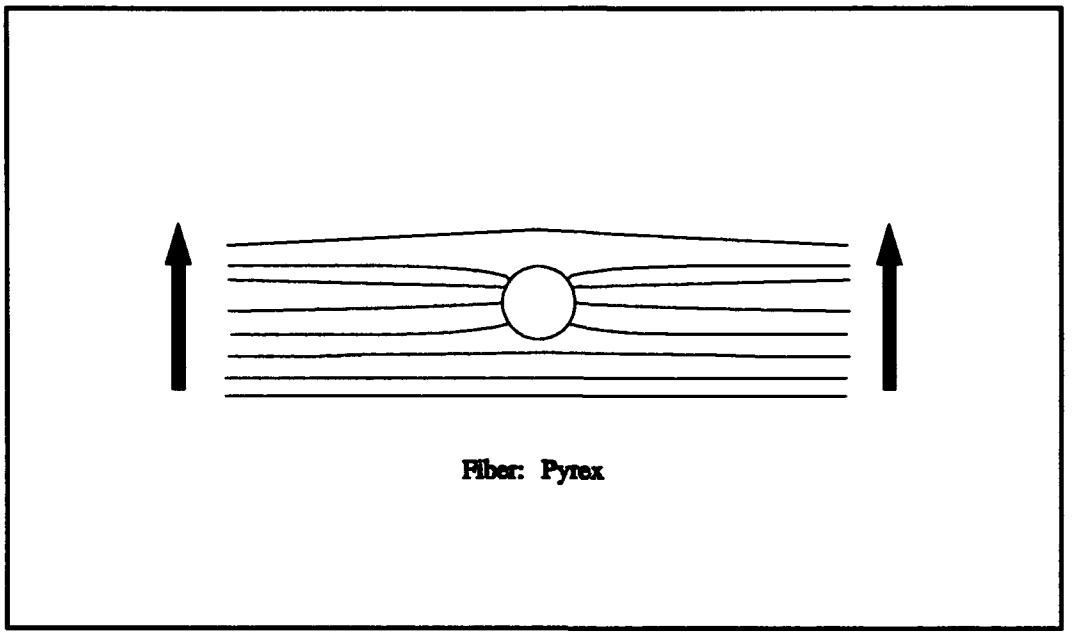

Figure 4.5 Crack-front profiles for a crack propagating around a pyrex fiber
Arrows indicate the direction of crack propagation

4.2.2 Development of Slip Zones

Specific fiber-matrix interactions (as discussed in section 1.2) were observed for four separate interfacial strengths. Pyrex fibers produced strong compressive interfaces. Epoxy fibers resulted in weak (possibly tensile) interfaces. A silicone release agent was used to limit chemical bonding; again decreasing the strength of the interface. Large crack-tip stress fields induced slip and separation (for weak interfaces) prior to arrival of the main crack. Residual normal compressive stresses diminished the influence of crack-tip stresses; however, slip was still observed. Debonding and the proliferation of secondary matrix crack characterized bridging fibers along weaker interfaces. Figures

E12 through E14 illustrate the damage occurring at the interface as the crack propagates past the epoxy fiber. Figures E15 and E16 illustrate the limited interfacial slip and debonding which occur along very cohesive pyrex interfaces. As theory predicts, slip does not initiate until the main fracture reaches the interface.

4.2.3 Failure Strength

During testing, if the fiber was not able to arrest or at least considerably slow the fracture, then growth continued to within a half inch of the edge of the specimen at which time the fracture became unstable and the template failed catastrophically (at loads as low as 1200 pounds). On the other hand, if growth was significantly slowed or arrested, the system could be loaded to 2000 pounds (limited by loadcell) without failure. A single test was conducted to determine the ultimate strength of a DCDC template with six epoxy fibers placed symmetrically above and below the main centrally-located hole. The fibers within each of the two groups of three were spaced approximately one fiber diameter apart. The ultimate load was found to be twenty percent greater than in a homogenous template: a notable increase. The critical crack length was found to be a quarter of an inch shorter than in the other cases. This results from the dramatic increase in load required to propagate the fracture around a series of inclusions. Interestingly for all tests which failed due to excessive crack length, not only did the fracture catastrophically extend to the end of the specimen, but also bent around and reentered at the center of the two columns (each comprising half of the initial template).

As discussed in Appendix C, growth was slowed significantly in two tests when the crack was well beyond the fiber. This is attributed to eccentric loading or material flaws which cause other failure mechanisms (buckling) to dominate. Retardation in crack propagation for these rare cases was followed by either ligament buckling or shear failure at one of the boundaries.

4.3 Computational Results

Larson's code was used to simulate fracture around cylindrical inclusions for five different interfaces. A Frictional Grab of 0.001 was used to model growth around a hole. The remaining cases as presented in Table D-1 in Appendix D were used to simulate growth around the various fibers. Figures 4.6 through 4.8 graphically illustrate the salient features of the crack periphery growing around the various interfaces. These figures indicate the areas around the inclusion which have magnified or retarded stress intensities. It is worth noting again that the solution, although similar in appearance to two dimensional results, are indeed fully three dimensional and include frictional sliding effects which are an essential component of the problem. The code is capable of determining the development of frictional slip zones, as well as the stresses within the fiber. Figures 4.9 and 4.10 illustrate these capabilities. Similar results are well documented in Larson's dissertation [19] for several values of Frictional Grab.

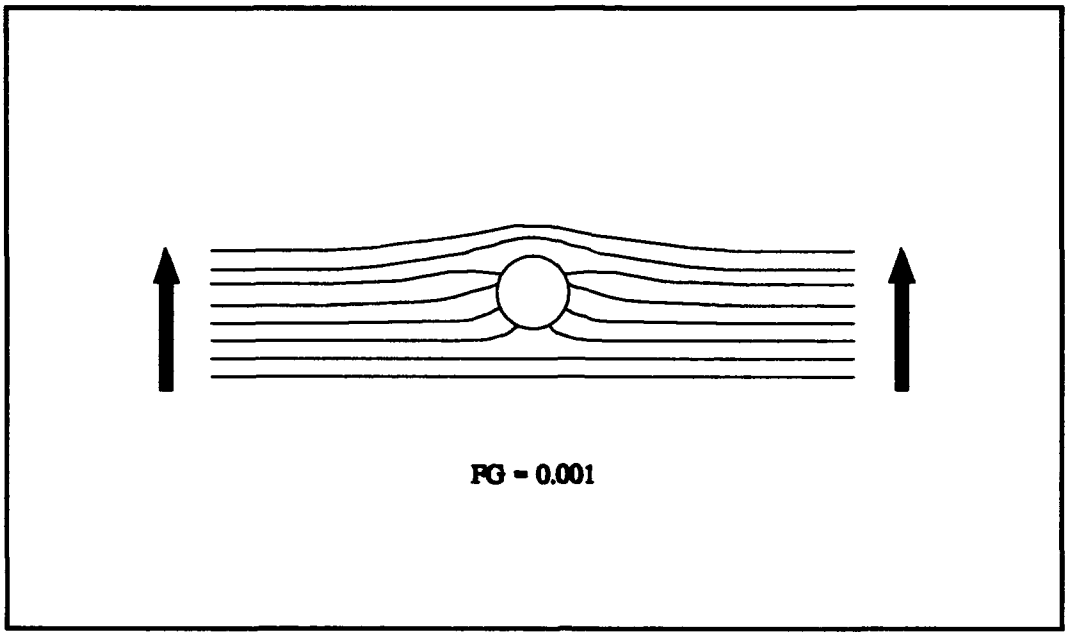

Figure 4.6 Crack-front profiles for a crack propagating around a cylindrical inclusion with a Frictional Grab interfacial cohesive strength of 0.001

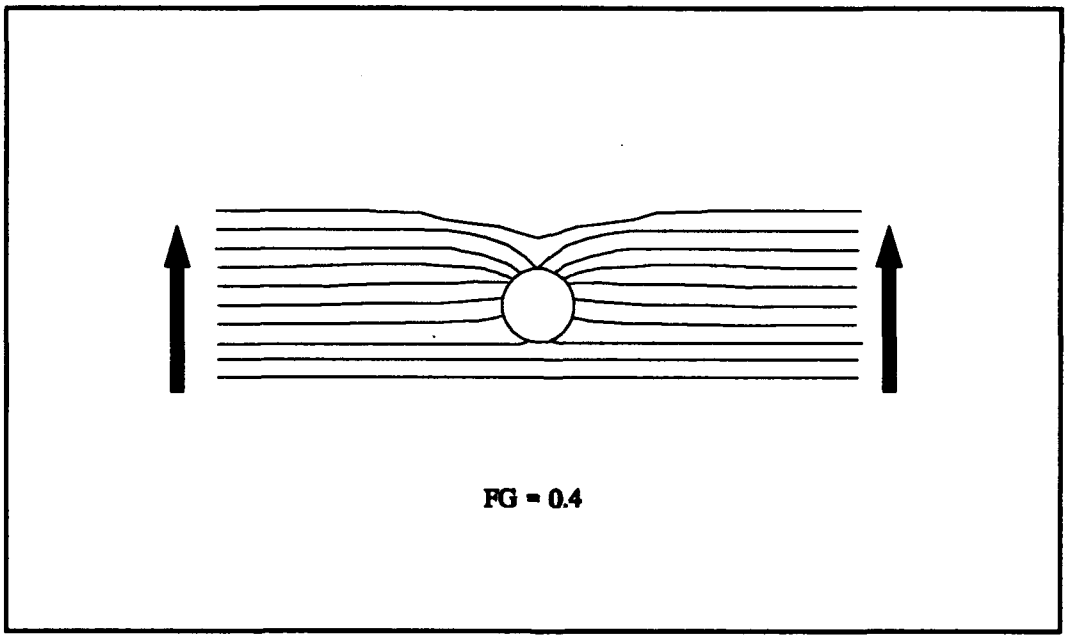

Figure 4.7 Crack-front profiles for a crack propagating around a cylindrical inclusion with a Frictional Grab interfacial cohesive strength of 0.4

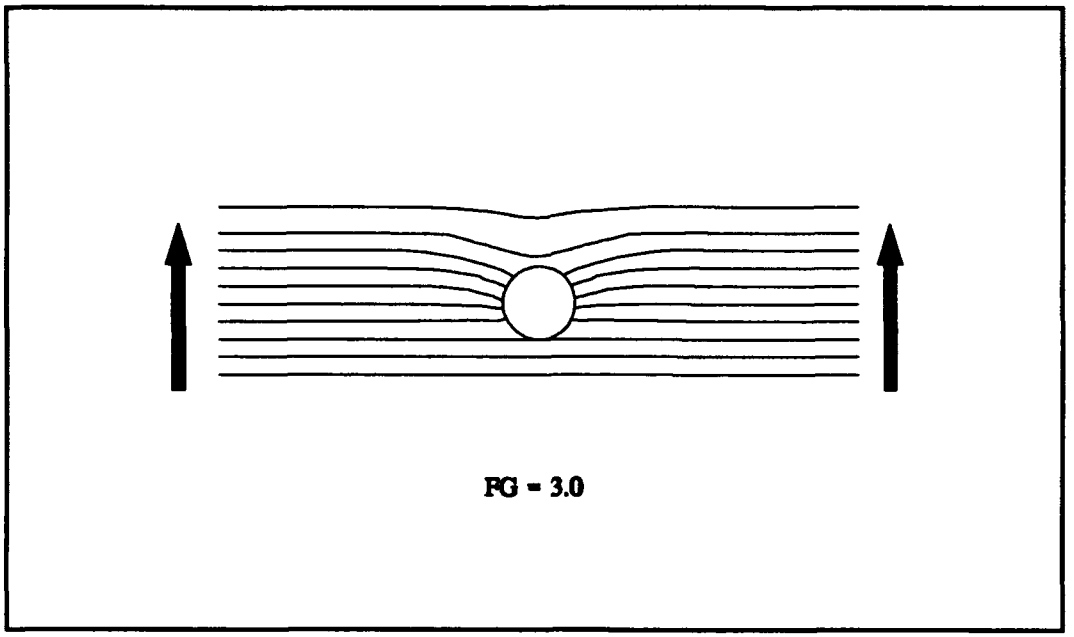

Figure 4.8 Crack-front profiles for a crack propagating around a cylindrical inclusion with a Frictional Grab interfacial cohesive strength of 3.0

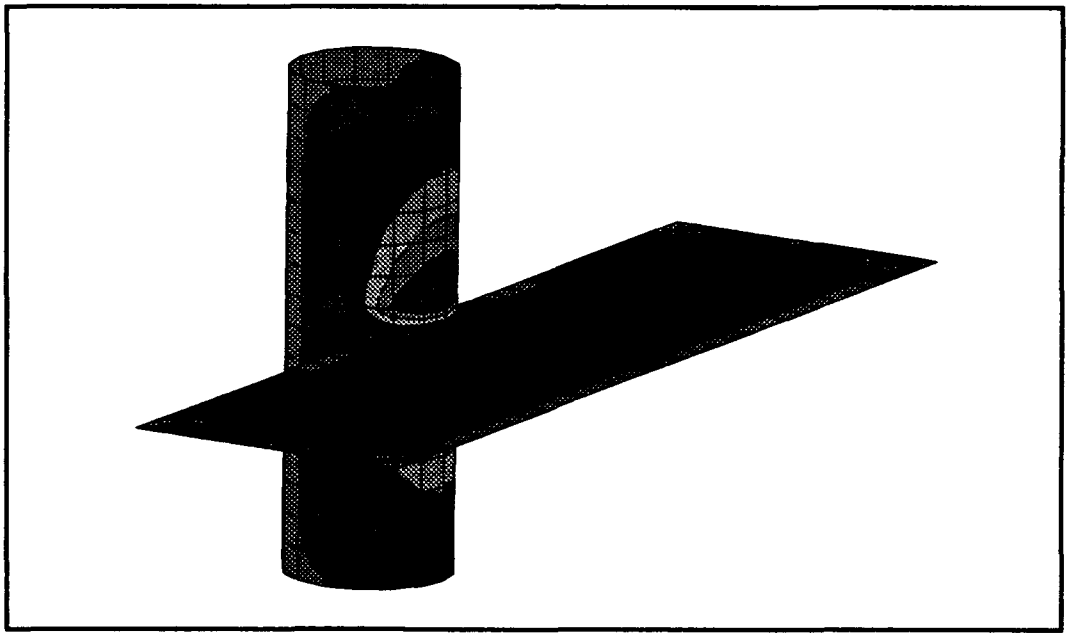

Figure 4.9 Computational prediction of the development of frictional slip zones

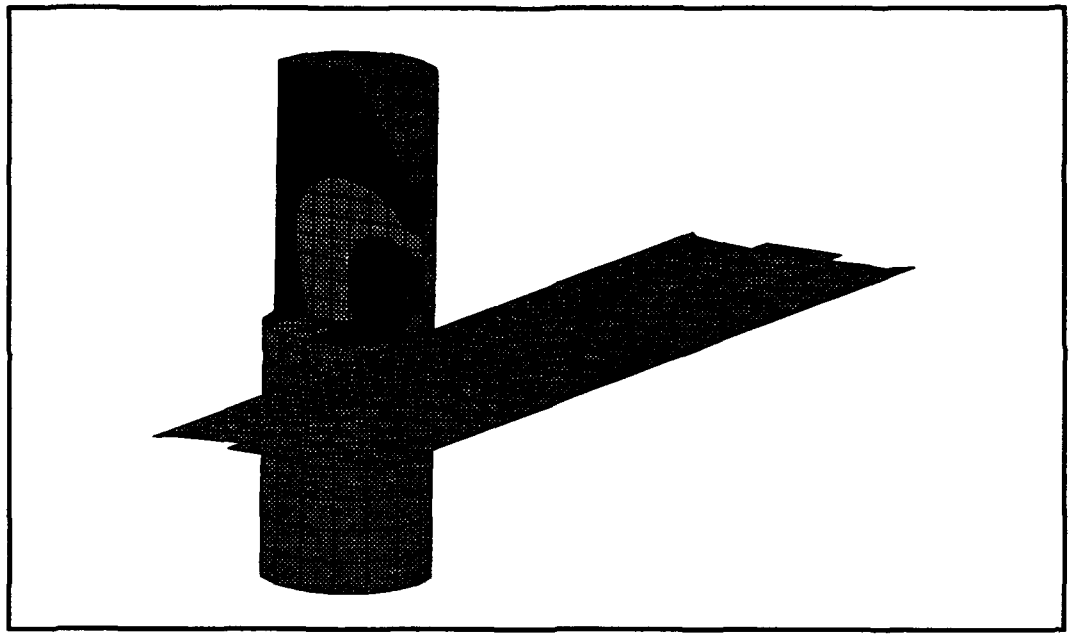

Figure 4.10 Computational prediction of fiber stresses

In an attempt to determine an appropriate increment to advance the periphery, a series of computational analyses were performed. An actual time history of crack propagation around a fiber (Figure 4.11) was used as a guideline for estimating the current position of the fracture. The most accurate results were obtained when the crack was advanced a distance of one-fifth of the fiber diameter. Figure 4.12 shows the computational results at similar locations to those in Figure 4.11. This information is extremely useful since it allows for a completely numerical estimation of toughening as a function of Frictional Grab. Further, by defining a constant value to march the crack forward, the time required for the fracture to reach a critical length, as well as, the variation in growth rate around the inclusion may be predicted. As an example, the number of computational runs required to march the fracture around an interface with a

Frictional Grab of 0.4 was fifteen percent greater than the number required for a Frictional Grab of 0.001. The number of runs is proportional to the time required to propagate the fracture around the interface, and ultimately defines toughening in our model composite system. Figure 4.13 shows a plot of normalized stress intensity values for a flat crack front emanating from the center of the fiber for FG values of 0.001 and 0.4. The stress intensity values are normalized with those of the same crack shape but with a FG of 3.0. The figure reinforces the point that less (time) computer runs are required for low FG values.

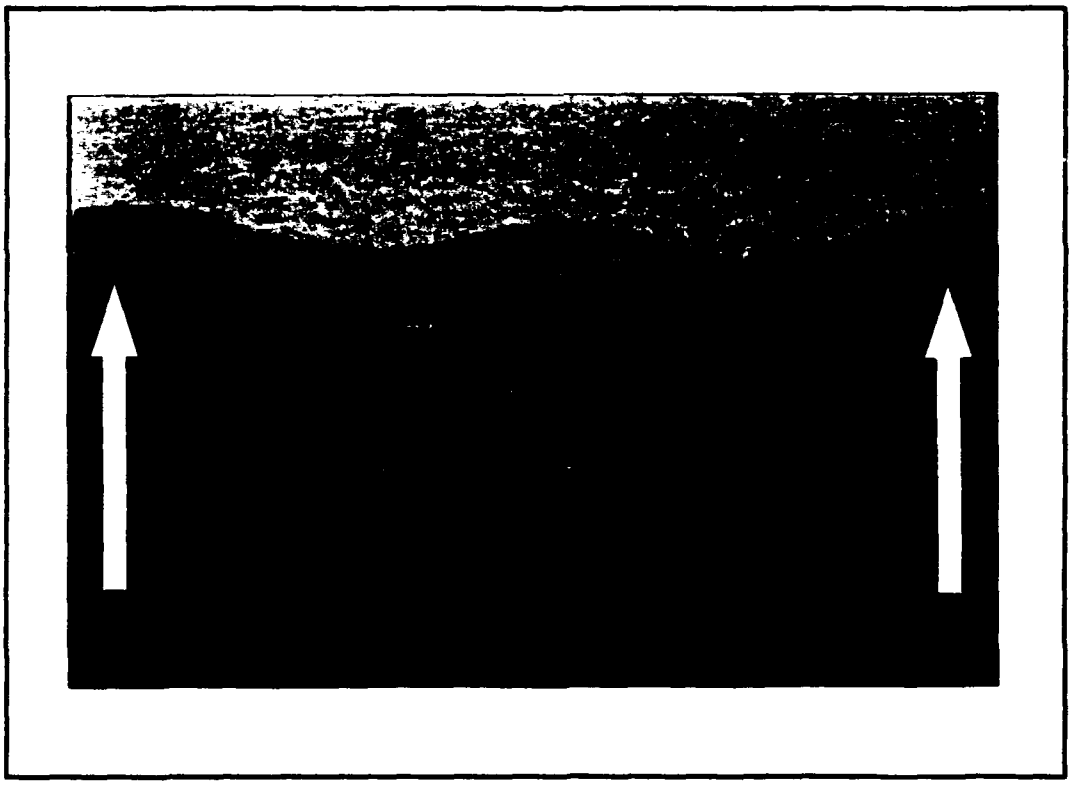

Figure 4.11 Experimental crack-front profiles for a crack propagating around a hole

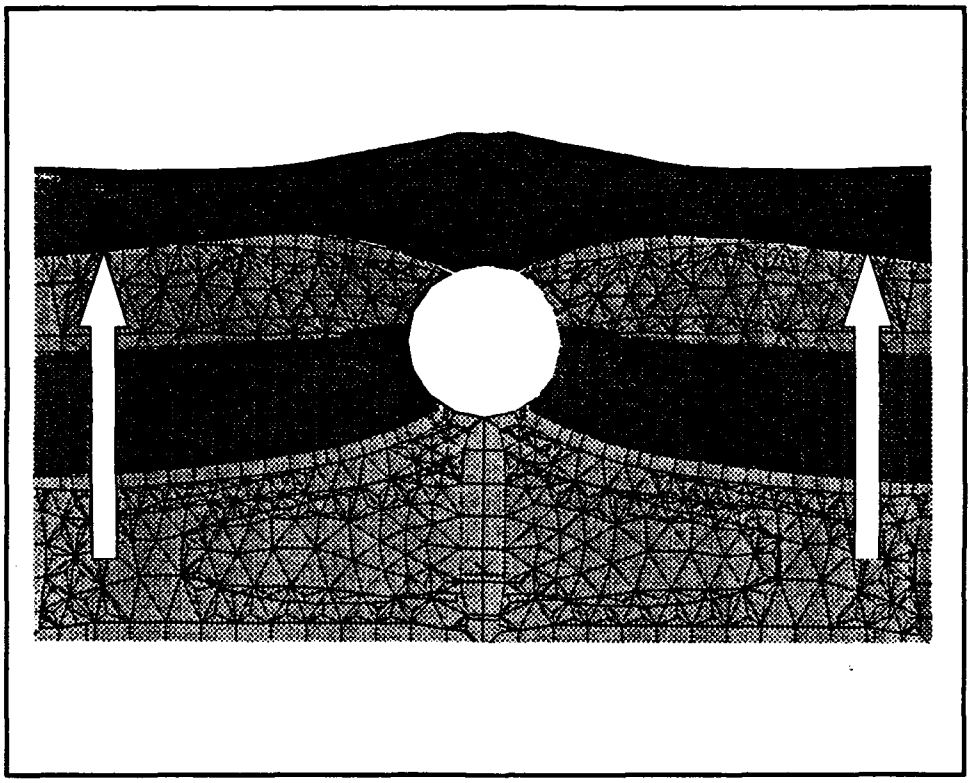

Figure 4.12 Computational crack-front profiles for a crack propagating around a hole

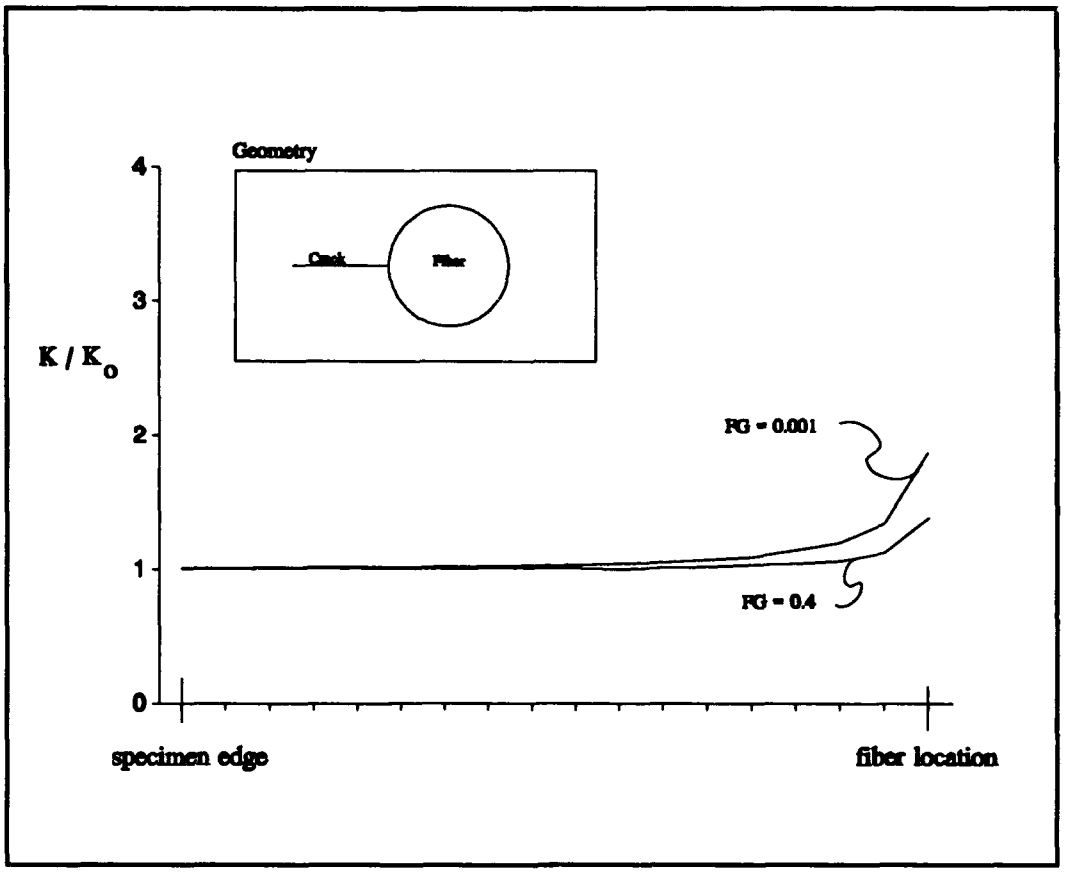

Figure 4.13 Normalized stress intensity values for a flat crack front emanating from the center of the fiber

CHAPTER 5

CONCLUSIONS AND RECOMMENDATIONS

This study has outlined principles from which one may better understand fracture in brittle fiber - brittle matrix composites. One goal is to move away from developing *(ex post facto)* crack growth laws based upon empirical data obtained from very specific tests which may not be applicable to "real world" applications. Validation of Larson's program is one step towards this end. The code may now be expanded with confidence that the elasticity solution adequately describes the problem at hand.

5.1 Experimental Procedure

Observation of quasi-static fracture in a brittle fiber - brittle matrix composite system was successfully accomplished. The development of slip zones, as well as variations in the shape and speed of the crack periphery, could be readily monitored using transparent Double Cleavage Drilled Compression test specimens. Procedures outlined in chapter two provided accurate and repeatable tests, and the glass templates proved surprisingly robust to manufacturing flaws. The most challenging aspect involved

choosing representative fibers which could be easily introduced into the matrix. Typical fibers used in CMCs usually have a (slightly) higher modulus of elasticity than that of the matrix material. This analysis assumed that for relatively weak interfaces, the influence due to the disparity between the moduli was overshadowed by affects produced from slip and debonding. Further analysis of the validity of this assumption should be conducted. A quantitative analysis of Frictional Grab versus Young's modulus would provide insight as to the roles of these two parameters.

One of the major problems with conducting these types of tests is that often the actual item may not be tested whether due to financial or equipment limitations; the mere complexity of the problem; the availability of material, or any of a number of reasons. Certainly computational models are limited by the very definition; however, even with most experimental tests, representative coupons are used in place of an actual inventory item. This study has taken the first step in analyzing quasi-static fracture in brittle materials. The next step is to take the models used (both experimental and computational) and make them more representative of ceramic matrix composites.

The fiber and matrix should be manufactured together such that chemical bonding occurs producing some fracture toughness at the interface. Typical CMCs incorporate fibers with diameters from 10 - 50 microns, and fiber volume fractions which may be quite high. If the inherent processing difficulties in producing a glass DCDC template with say a hexagonally-patterned arrangement of small brittle fibers can be eliminated,

than we have taken the next step in the investigation. Fuller attempted to eliminate this problem by placing fibers between two glass plates and then hot pressing them together. However, a large number of imperfections (bubbles) formed at the interface.

As discussed in the first few pages of chapter one, ceramic composites are amenable to high temperature applications. Therefore, a logical extension of this work would be to include thermal - mechanical testing. Additionally, as was discovered during testing, the percentage of moisture in the air may influence crack-growth rates, and may be worth further investigation.

Computationally, stresses within the fiber are calculated. It would be interesting to experimentally determine these results for comparison. Piezoelectric materials or hollow cylindrical fibers with strain gages are two possibilities for measuring these stresses. Also, if a camera with a higher magnification is used, interfacial debonding and slip could be more readily observed providing a better understanding of the micro-mechanics involved with the problem at hand.

5.2 Computational Procedure

This analysis has presented experimental data necessary for the development of an empirical crack growth law suitable for quasi-static fracture in brittle composite systems. Simply marching the crack periphery forward by an amount proportional to the stress intensity value at discrete nodal coordinates adequately represented variations in the crack front for growth around cylindrical inclusions. However, as discussed in the last chapter, there is no physical law validating this approach. In reality, K is never greater than K_{1c}, nor is the periphery a series of discrete nodes. Thus, a more representative, physically sound, law needs to be developed which is capable of modelling a series of fibers, as well as, a representative volume element.

As an aside, the statement "simply marching the crack periphery forward" is not entirely correct. Computers are notorious for generating tremendous amounts of data, and the operator must than objectively apply his engineering judgement and determine the value of the information. Larson's code provided stress intensity values at discrete nodes along the crack front; however, for small growth increments, variations in these values became ambiguous. It was difficult to determine the curvature which the periphery would assume. Further, in defining the geometric nodes for the next time step, care had to be taken to ensure that the proper number and orientation of nodes were chosen to satisfy the cubic spline algorithm incorporated in the automatic mesh generator. Marching the crack forward a distance of one-fifth of the fiber diameter, however, seemed to provide sufficient accuracy.

As with the experiments, the computational analysis should be expanded to be more representative of an actual ceramic-matrix composite. In reality, fiber - matrix interfaces have some fracture toughness. Further, interfaces are prone to imperfections which translate into stress concentration sites. A statistical distribution of nucleations sites could be included, and special crack-tip elements added to the interface to account for these problems. The code should also be expanded to include multiple fibers, angled crack approach, interfacial penetration, general crack geometries, and different constituent properties. Note, however, that the latter additions would require a tremendous overhaul of the code since they may involve singularity problems; mixed-mode stress intensities, and complex crack growth laws. The code also does not account for residual matrix stresses which exist to satisfy equilibrium along the interface.

A series of parametric studies should be accomplished to determine convergence rates versus computational time. The crack should be marched forward in small increments in order to capture variations in periphery shape, but not at unreasonably high computer expense. Further, alternate studies estimating the minimum number of crack-tip elements required to yield sufficient accuracy should be performed to minimize computer memory requirements.

Design engineers desire handbooks listing optimal interface strengths for various fiber - matrix combinations similar to the one found in Figure 5.1. If the interface is too strong, premature fiber failure may occur. If the interface is too weak, critical energy

dissipation will be lost. Therefore, a series of computational runs determining the best Frictional Grab to obtain maximum energy dissipation need be executed. These tables would allow an engineer the ability to determine interfacial coatings or processing techniques in order to optimize the strength of the composite.

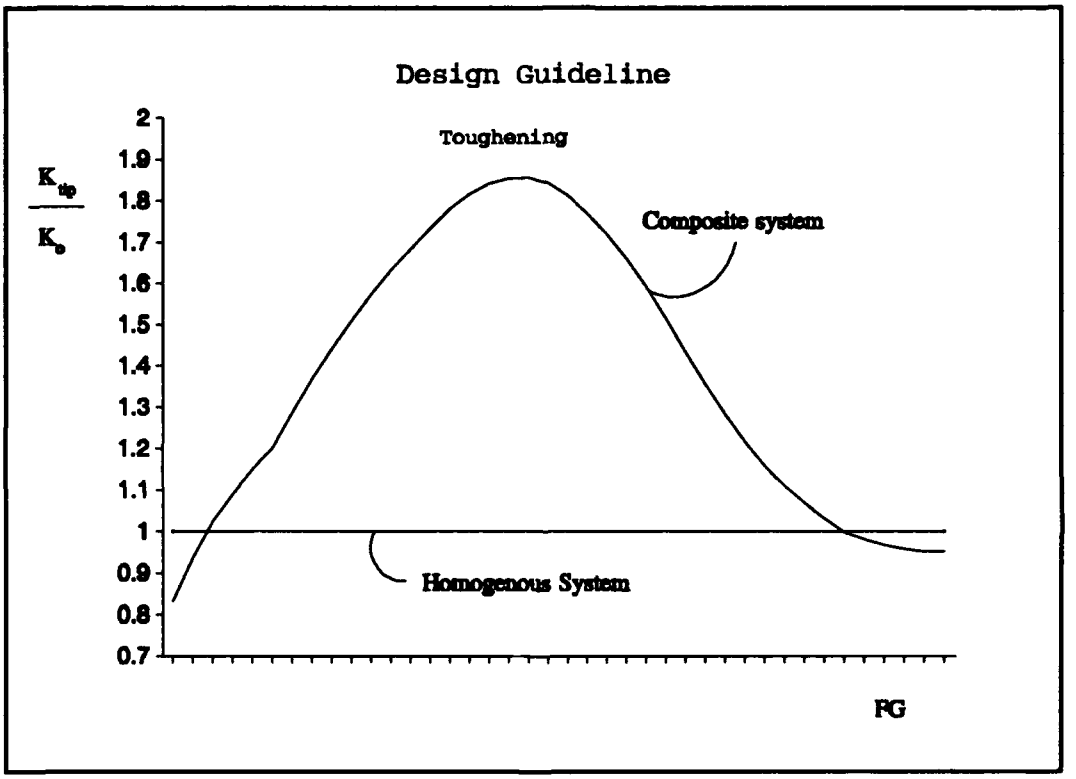

Figure 5.1 Sample chart for determining optimal interfacial strength

APPENDIX A

COMPUTATIONAL ANALYSIS OF CRACK GROWTH NEAR PLANAR INTERFACES

Parametric studies investigating critical input parameters determine (1) the influence of different variables upon the stress distributions and associated displacements along an interface, and (2) the validity of the Frictional Grab parameter, FG, as a single characterization of interface cohesion defined by

$$FG = \mu \frac{\sigma_r}{\sigma_o}$$

where

σ_r = Residual normal compressive stress

σ_o = Driving stress

μ = Friction coefficient

As such, the interface does not have any fracture toughness, but dissipates energy through frictional sliding. The maximum extent of slip at an interface was determined for two different situations:

(1) μ=.1
$0.0 \leq \sigma_r/\sigma_o \leq 100.0$
$0.0 \leq d/a \leq 2.0$

(2) $\sigma_r/\sigma_o = -5.0$
$0.0001 \leq \mu \leq 100.0$
$0.0 \leq d/a \leq 2.0$.

A portion of the results are provided in Figures A1 and A2.

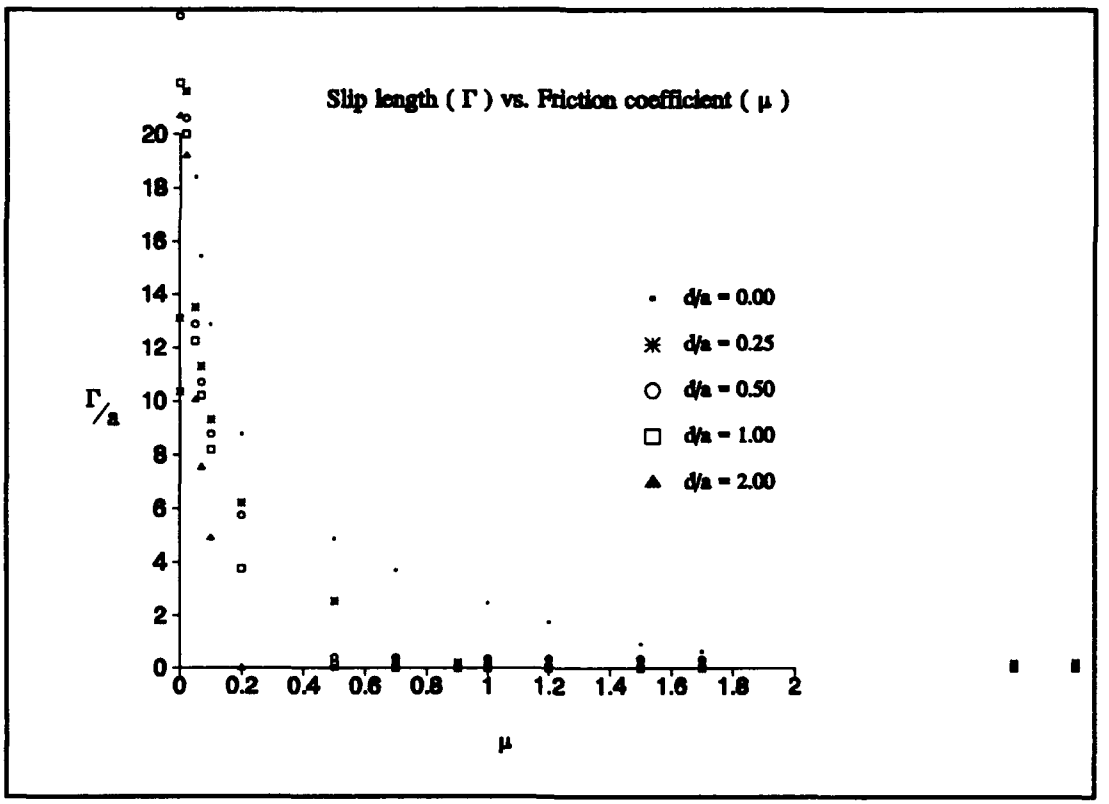

Figure A1 Slip length versus friction coefficient

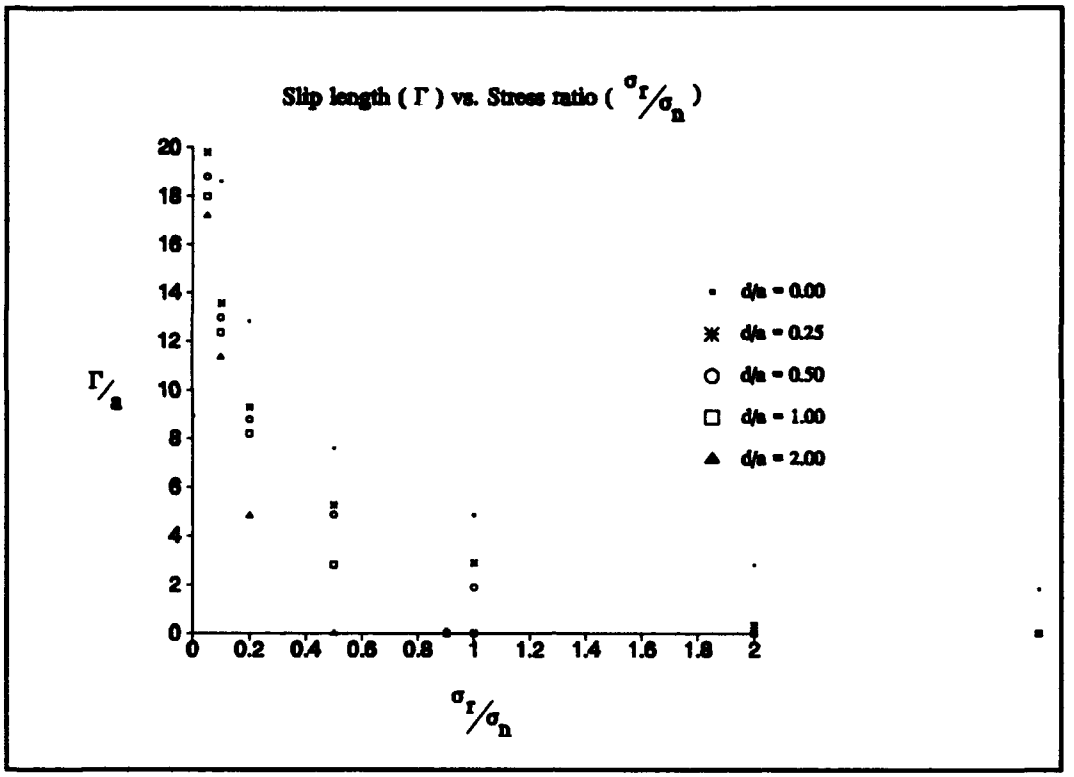

Figure A2 Slip length versus stress ratio

The general tendency for the slip length to increase as μ decreases for case 1 and as σ_r/σ_o decreases for case 2 is to be expected. The apparent similarity in the shape and magnitude of the curves in Figures A1 and A2 suggest that slip length may remain constant for a given Frictional Grab. Further investigation revealed that slip length did in fact remain reasonably constant for specific values of Frictional Grab over definitive bands of μ and σ_r/σ_o. Results are listed in Table A-1.

Table A-1 Frictional Grab evaluation

μ FG	0.001	0.01	0.10	1.00	2.00	3.00	4.00	10.0
0.0001	x	x						
0.0010	x	x	x					
0.0100	x	x	x	x				
0.1000	x	x	x	x	x	x		
1.0000	x	x	x	x	x	x	x	
10.000	x	x	x	x	x	x	x	x

x's denote the range of μ for which the slip length was within five percent of the norm for a given Frictional Grab. If you are interested in a Frictional Grab of 0.01, for example, than you may use any combination of friction coefficients (between 0.001 and 1.0) and appropriate stresses which yield the desired FG. Table A-1 illustrates that for the analysis at hand, the Frictional Grab parameter is sufficient to characterize interfacial resistance.

Figures A3 - A7 show typical slip and stress distributions for different values of Frictional Grab. For cohesive interfaces (large values of FG), stresses are easily transferred across the interface; localizing displacements. "Slippery" interfaces result in a greater distribution of stress fields brought about by slip which occurs along the interface. As the crack approaches the interface, stress distributions for low FG values

appear to shift with crack approach with only a small increase in magnitude. Stronger interfaces exhibit increasing localization and growth of stresses as the crack propagates toward the fiber. Again due to the sliding which occurs along weaker interfaces. Ideally, designers would like to optimize the strength of an interface to transmit stresses at values up to but just below fiber failure such that maximum energy dissipation occurs.

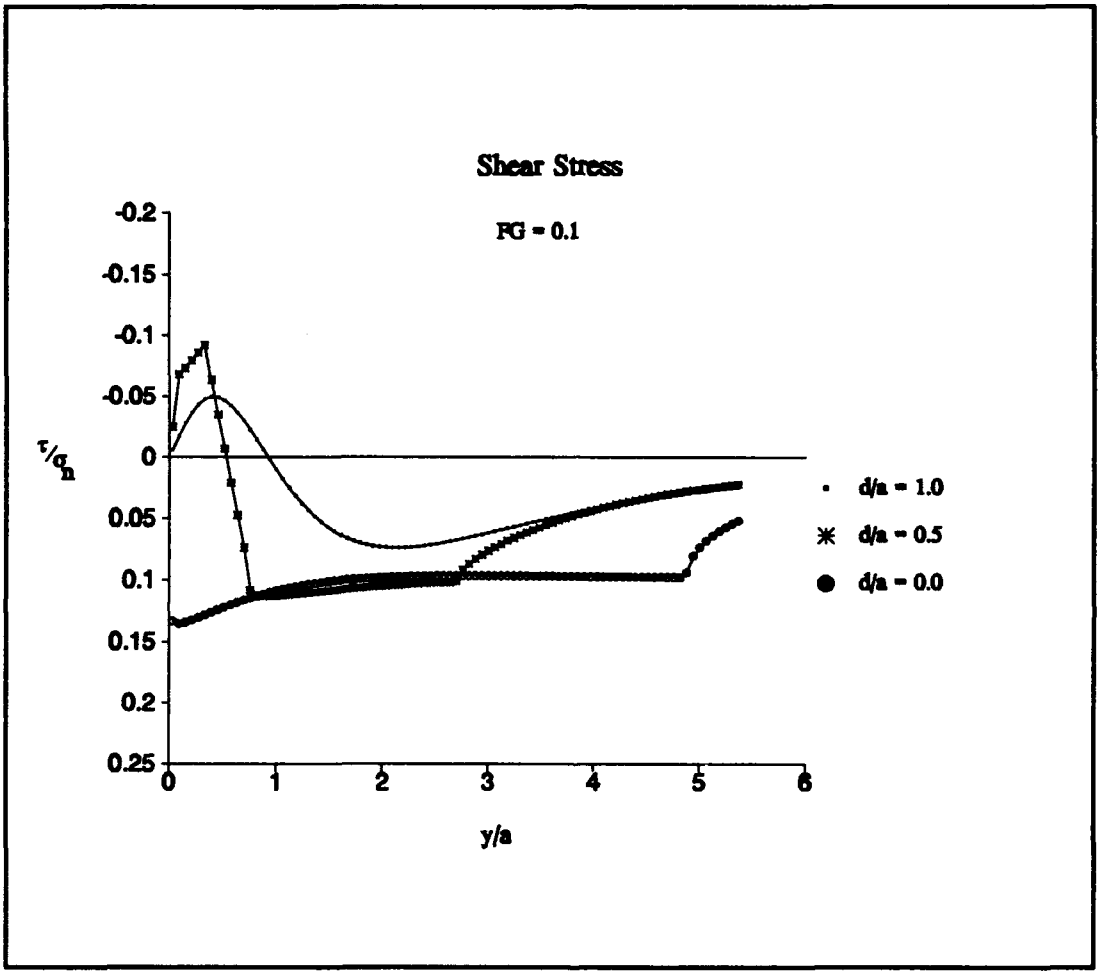

Figure A3 Shear stress distribution, FG = 0.10
"y" is the height along the interface above the crack plane as shown in Figure 1.7

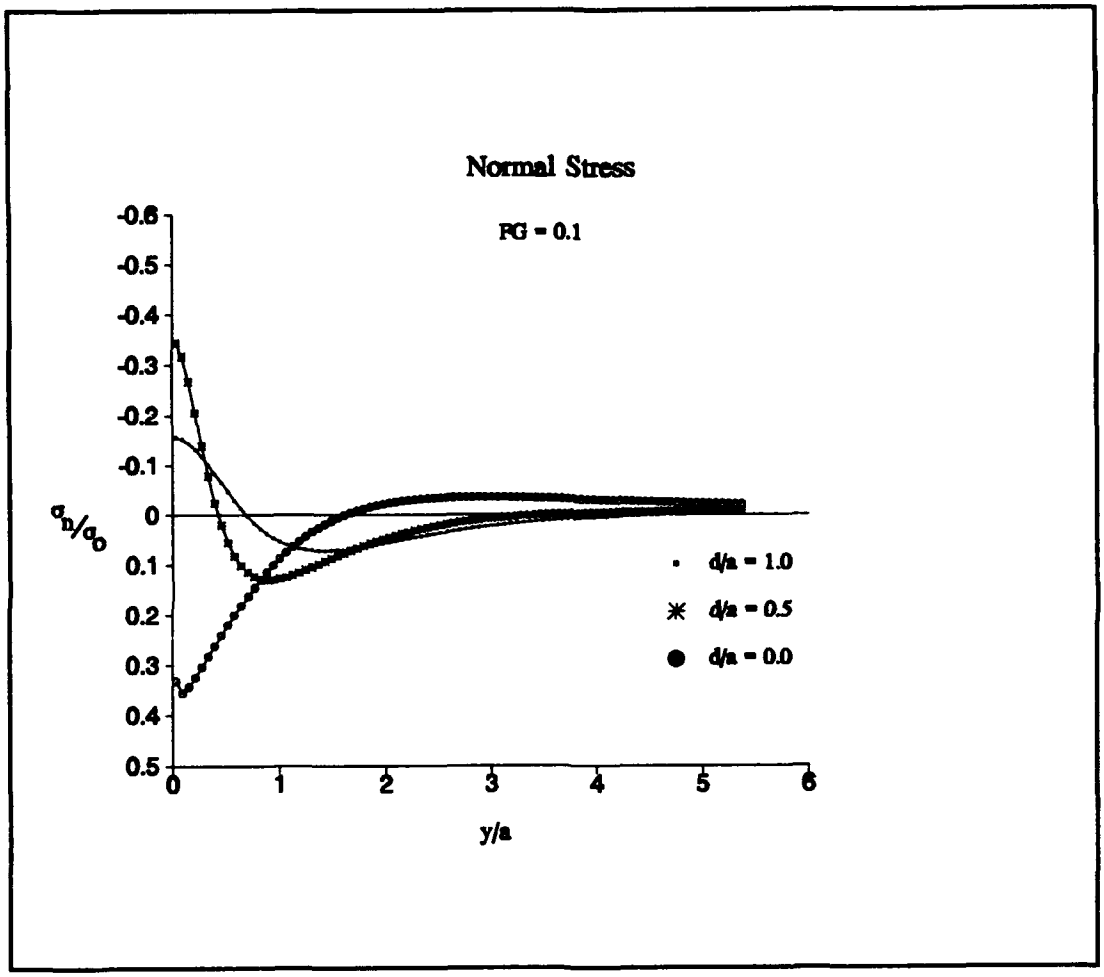

Figure A4 Normal stress distribution, FG = 0.10
"y" is the height along the interface above the crack plane as shown in Figure 1.7

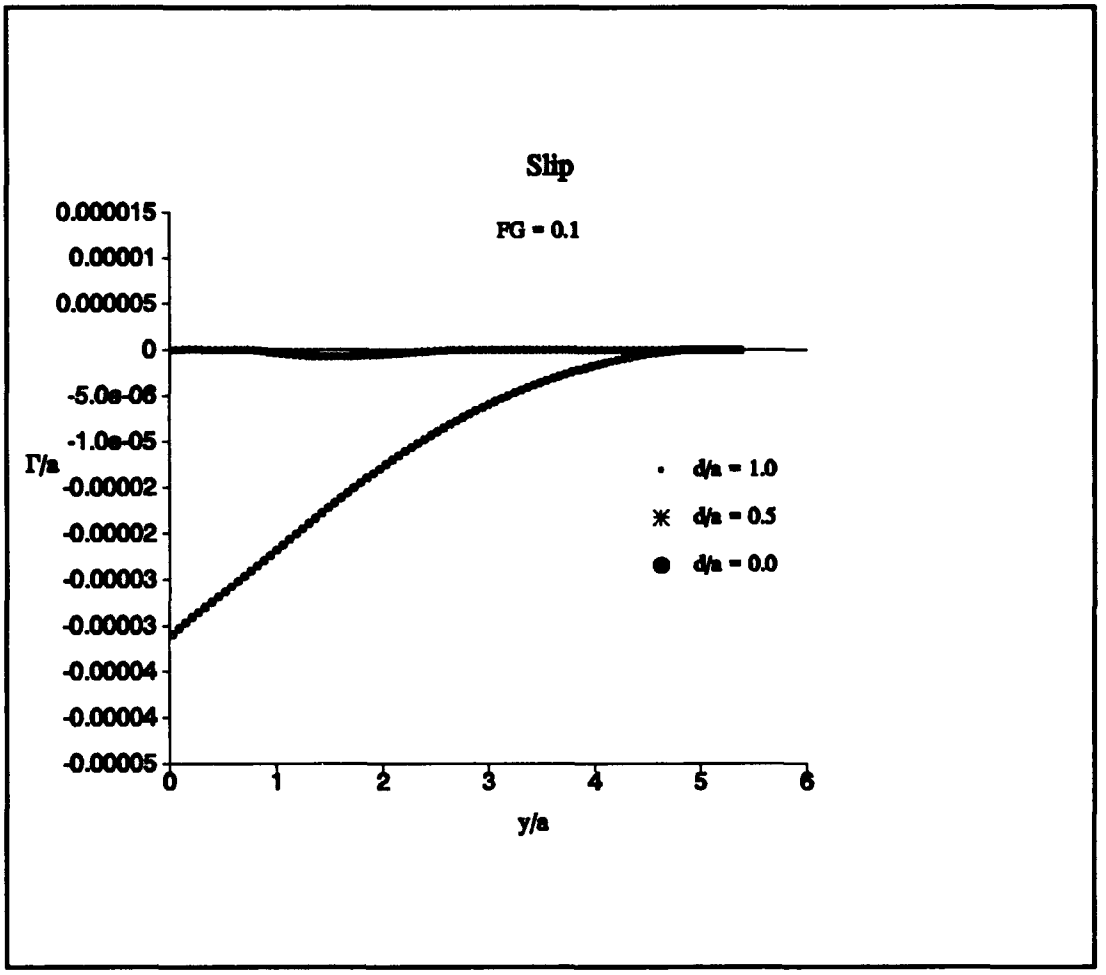

Figure A5 Slip, FG = 0.10
"y" is the height along the interface above the crack plane as shown in Figure 1.7

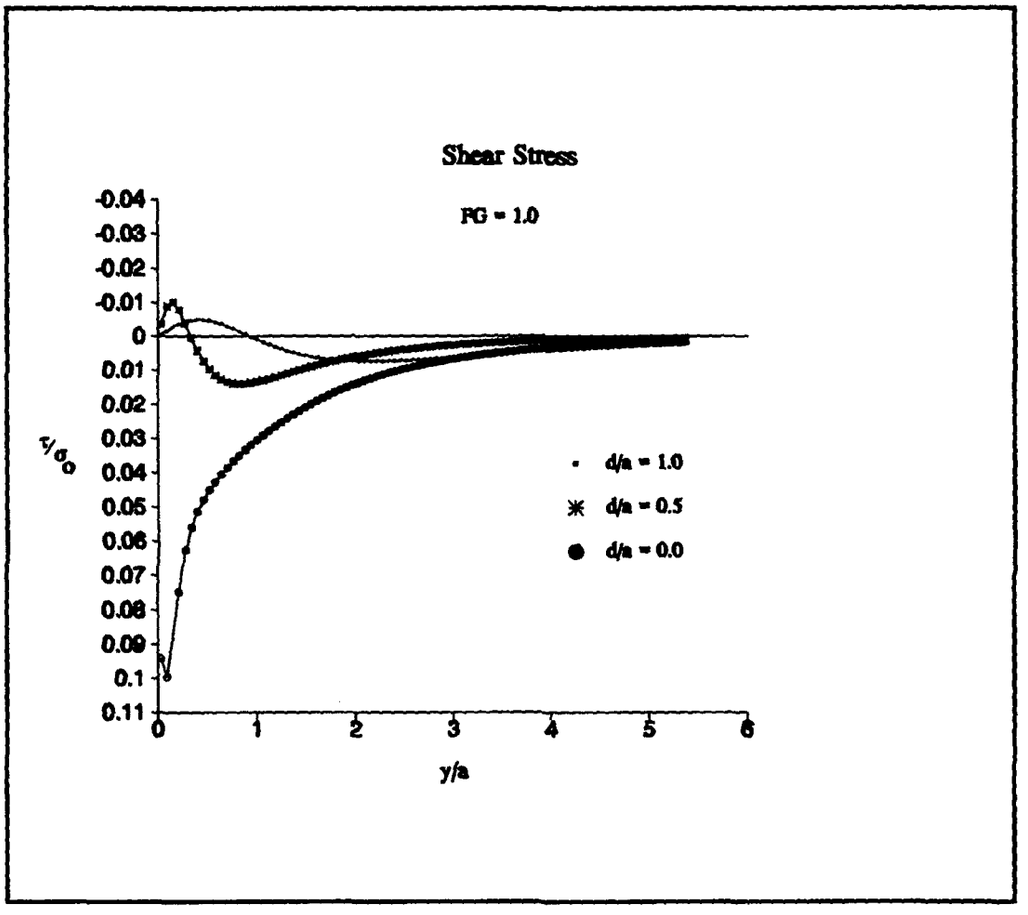

Figure A6 Shear stress distribution, FG = 1.00
"y" is the height along the interface above the crack plane as shown in Figure 1.7

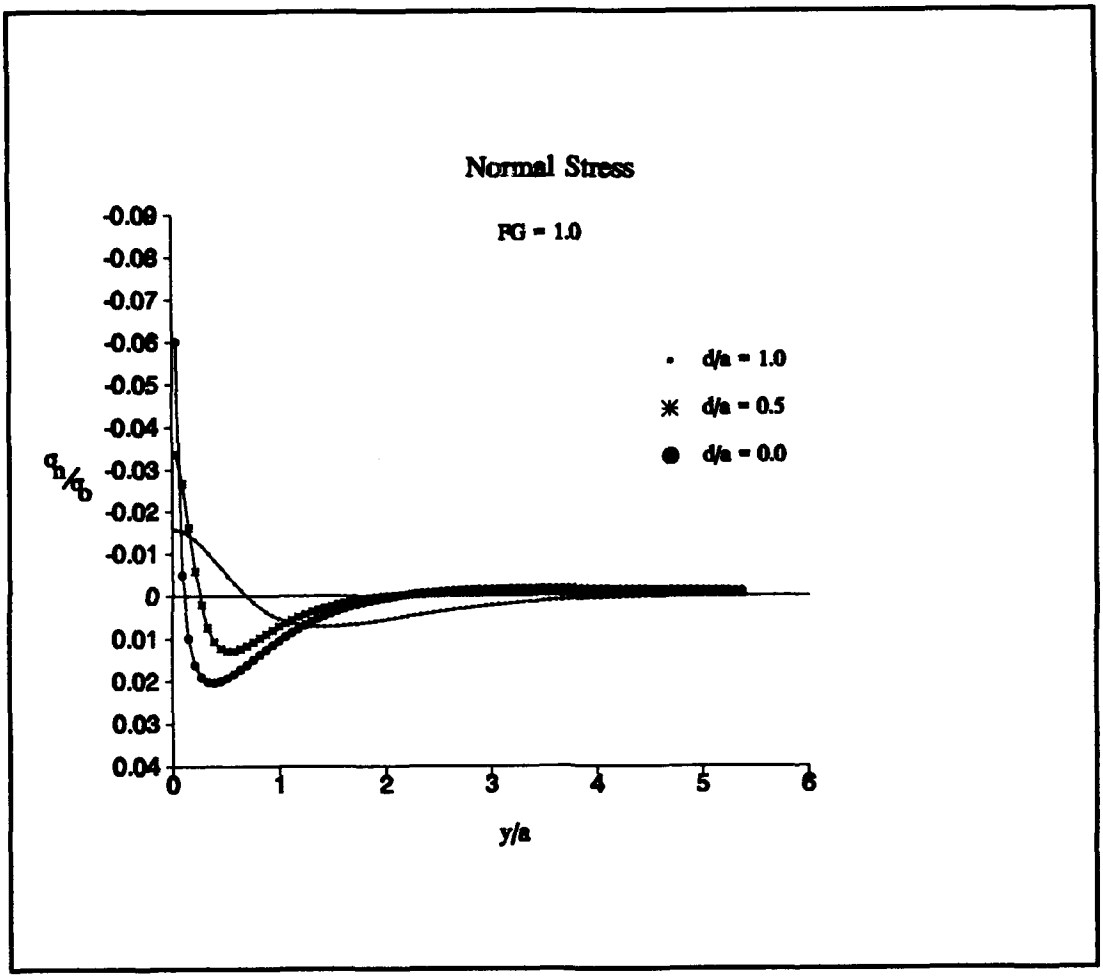

Figure A7 Normal stress distribution, FG = 1.00
"y" is the height along the interface above the crack plane as shown in Figure 1.7

APPENDIX B

STABILITY ANALYSIS OF DOUBLE CLEAVAGE DRILLED COMPRESSION (DCDC) SPECIMENS

Stability requires that the crack advance at constant increments, da, when subjected to incremental loads. If growth is unstable, failure would be catastrophic. Stability is therefore critical in controlling the growth of the crack toward the fiber such that interactions at the interface may be monitored. As discussed in section 1.3, crack growth occurs if the stress intensity factor, K, at the crack tip is greater than K_{Ic}, the fracture toughness. This is analogous to saying, yield occurs if σ is greater than the yield stress of the material, σ_y. For brittle plane strain materials, K_{Ic} is assumed constant. Stability requires that K decrease with increasing crack length such that for a crack in an infinite medium, K will eventually fall below K_{Ic}, and growth will arrest (Figure B1). Further, the applied stress intensity factor is related to the compliance of the body by

$$K^2 = \frac{EP^2}{2B}\frac{\partial c}{\partial a} \qquad (1)$$

Thus the stability requirement becomes that the slope of the compliance versus crack length curve must decrease with increasing crack length.

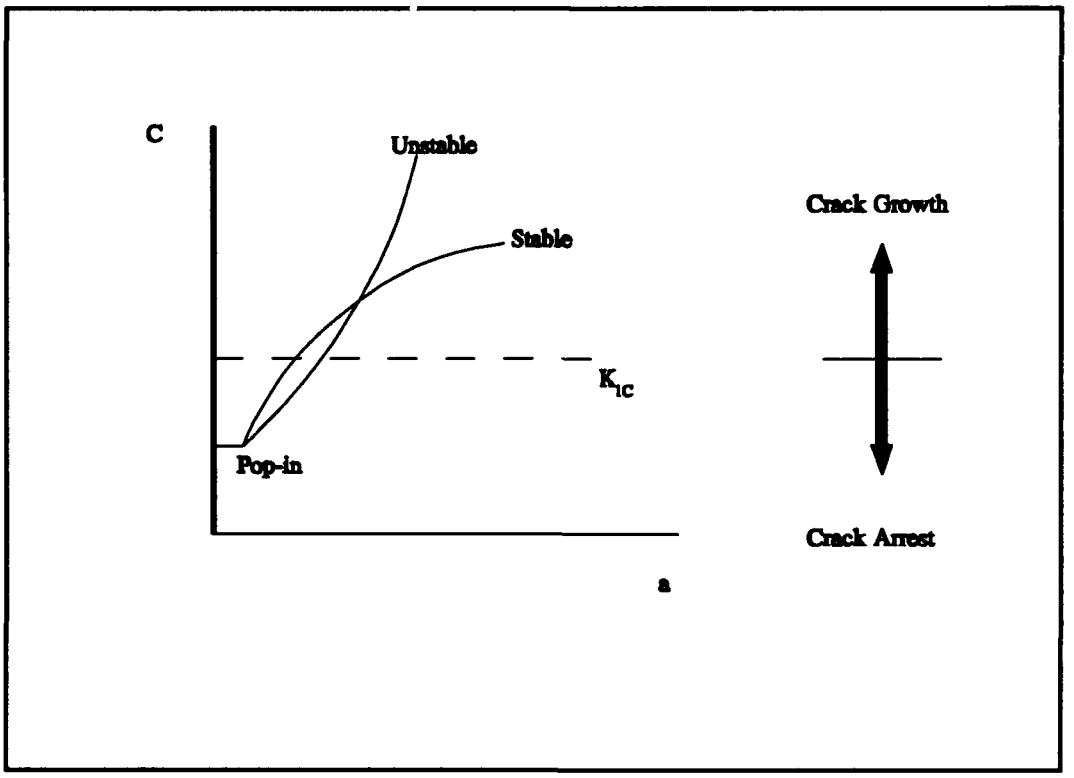

Figure B1 Crack arrest in brittle materials

Any standard finite element package will calculate load versus displacement data from which the compliance of the system can be determined. The Double Cleavage Drilled Compression specimen was modelled using I-DEAS™. Symmetry required that only a quarter of the specimen be meshed (Figure B2).

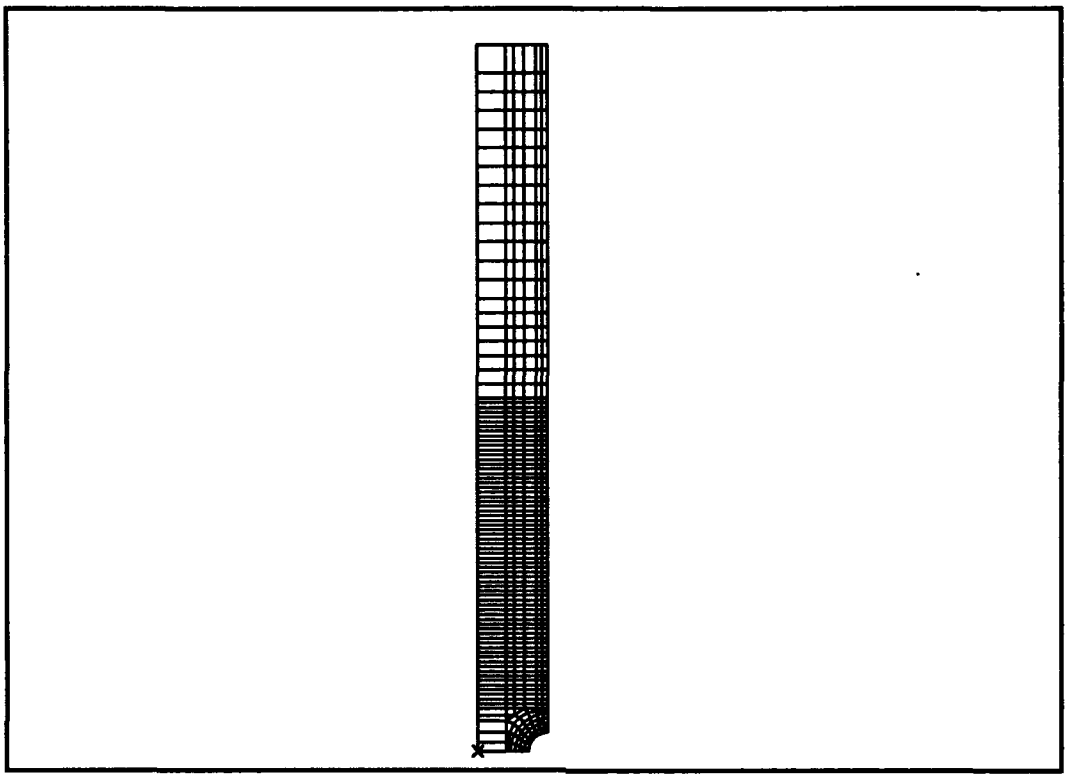

Figure B2 Double Cleavage Drilled Compression mesh

The mesh consisted of approximately 5000 8-noded brick elements. Zero shear on planes of symmetry was enforced. The crack was modelled as a free surface which allowed updating the crack length by simply changing a few degrees of freedom. The compliance of the system was determine for five different crack lengths: the largest of which extended through one-half the length of the specimen. It was assumed that the stress singularity at the crack tip would not significantly influence the compliance of the system at any given instant in time. This eliminated the need for special crack-tip elements. A similar model was successfully used by Morrison [22].

Figure B3 shows that, as would be expected, the material does become more compliant with increased crack length. Further, Figure B4 shows that fracture in DCDC specimens is indeed stable since the slope of the curve decreases with increasing crack length.

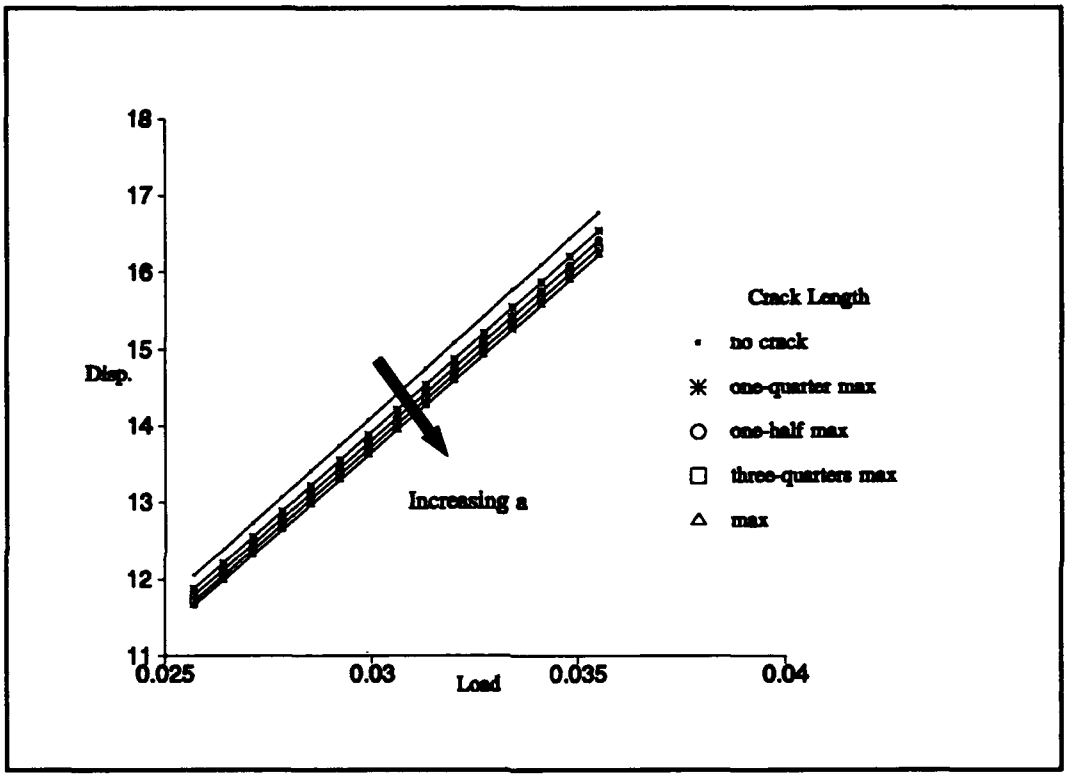

Figure B3 Compliance data

Fuller performed a similar stability analysis, in which he showed stable crack growth is preceded by a short unstable growth, commonly referred to as pop-in. The term "pop-in" is used since the sudden unstable crack extension is often accompanied by an audible click. Experiments verify that pop-in does in fact occur during testing.

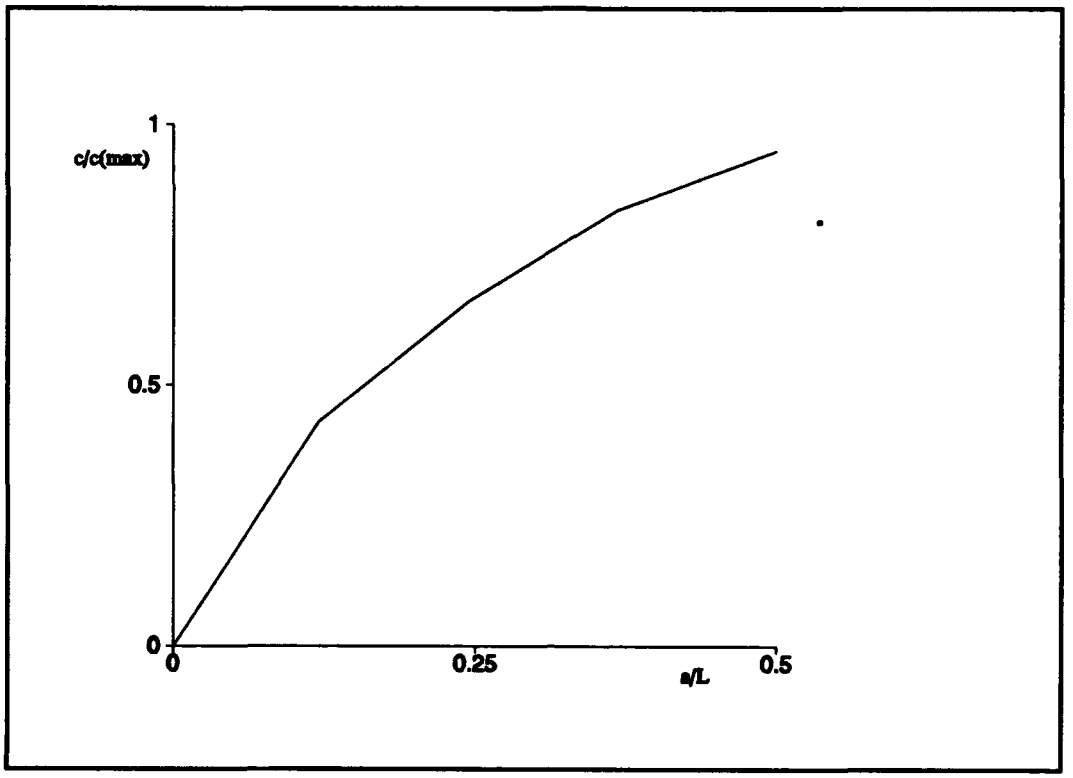

Figure B4 Compliance versus crack length

APPENDIX C

BUCKLING ANALYSIS OF DOUBLE CLEAVAGE DRILLED COMPRESSION (DCDC) SPECIMENS

Dimensions of the Double Cleavage Drilled Compression test templates were calculated to ensure fracture occurred at the large center hole prior to buckling failure. To eliminate edge affects and ensure the fiber length was large relative to the crack plane, the width was kept large. The length of the specimen was chosen to satisfy Saint Venant's principle for a significantly large crack length.

Determination of critical buckling loads support experimental findings of stable fracture prior to buckling failure. Euler's buckling equation is developed by finding the equilibrium position for which the first variation in potential energy of a buckling column is stationary. For the case of a column with hinged ends, Euler's formula is given by Equation (1). L/k is known as the slenderness ratio, and is a commonly grouped as a single parameter in stability comparisons in columns [30].

$$\sigma_{cr} = P_{cr} A = \frac{\pi^2 E}{(\frac{L}{k})^2} \quad (1)$$

where

A = cross-sectional area

L = specimen length

k = radius of gyration

E = Young's modulus

Modelling the template as two notched columns (Figure C1) and using the dimensions found in Figure 2.1 and material properties from Table 2-1, a worse-case critical buckling load is found to be 4000 pounds. The DCDC specimens were loaded to a maximum of 2000 pounds (limited by the loadcell) without buckling failure.

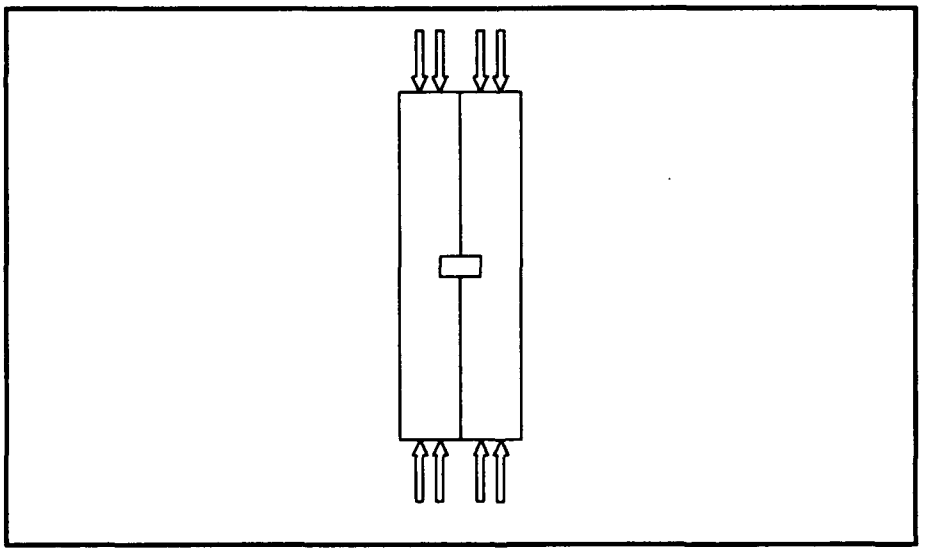

Figure C1 Buckling model

Equation (2) is used to calculate the load at which fracture initiates at the hole [2]. Using the same dimensions and material properties, the critical fracture load is found to be 1500 pounds.

$$P_{cr} = \sqrt{\frac{8\,E\,R}{\pi\,r}}\,A \tag{2}$$

It was noted that once fracture occurred in the DCDC specimen, growth occasionally arrested once the crack reached some critical length. Examining this phenomenon from an energy point of view, it appears that crack growth is arrested because the energy available for the creation of new surface area is consumed by another failure mechanism. As one example, the driving force behind the propagation of the crack can be viewed as two columns which are joined at the top and bottom and tearing apart as they buckle in opposite directions (Figure C2). As the crack length increases, the critical buckling load of the ligaments decreases as a function of square of the crack length. Letting the half crack length, a, be equal to one-half the length of the buckling ligament, Euler's buckling equation becomes

$$P_{cr} = \frac{2\,\pi^2\,E\,k^2\,A}{a^2} \tag{3}$$

Since fracture in linear-elastic brittle materials is assumed independent of crack length, as the crack length and corresponding load continue to increase, eventually buckling becomes the dominate failure mechanism. Note for specimens which were precisely milled, buckling did not occur. The specimens failed due to excessive crack length.

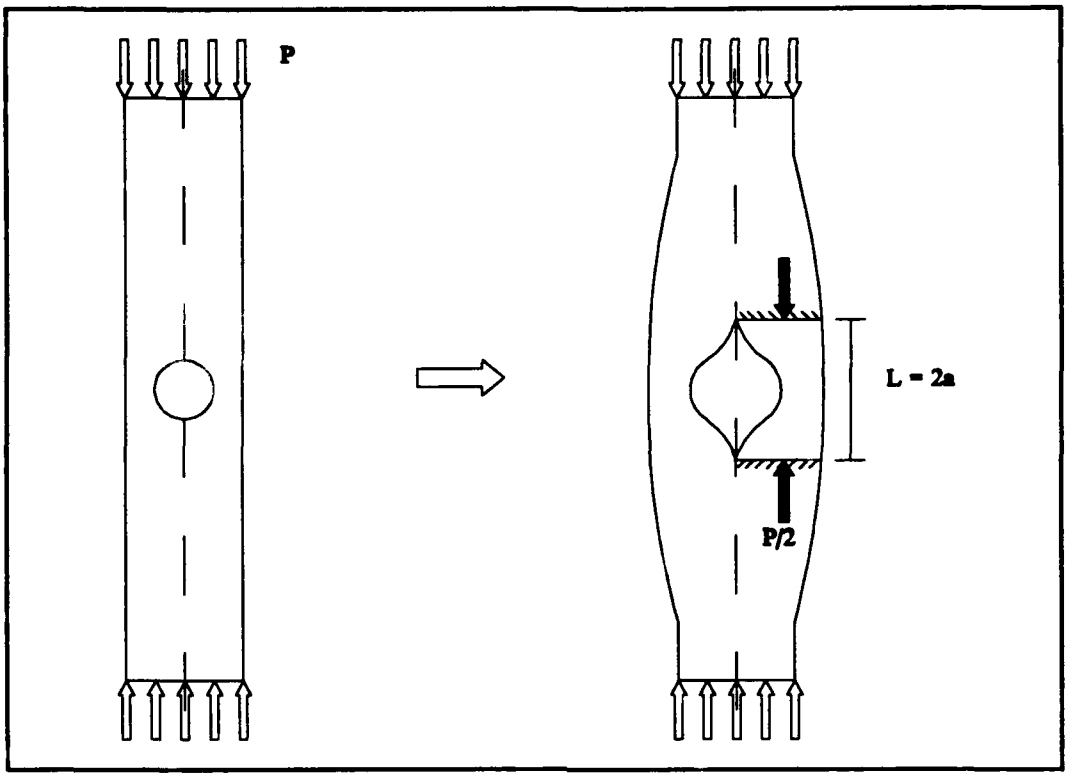

Figure C2 Ligament buckling

The above analysis is presented as an example of energy trade-off. It is not suggested that this is what is actually occurring during testing; there are other effects which attribute to arrest of the crack growth. The crack may grow beyond the stress concentrations provided by the center hole, or the crack may grow too close to the edges where again the state of stress changes and where Saint Venant's principle is no longer valid.

A finite element analysis was accomplished to ensure eccentric loading did not adversely affect the state of stress in the region of interest*. Comparison of a relatively course model with a uniform load and a severe wedge load validated Saint Venant's principle. Stresses in the region of interest were almost exact. Stress contours (σ_y) are shown in Figure C3 for the two loading cases. The stress values within the lower contours are the same. 10,000 PSI is the maximum stress applied to the specimen.

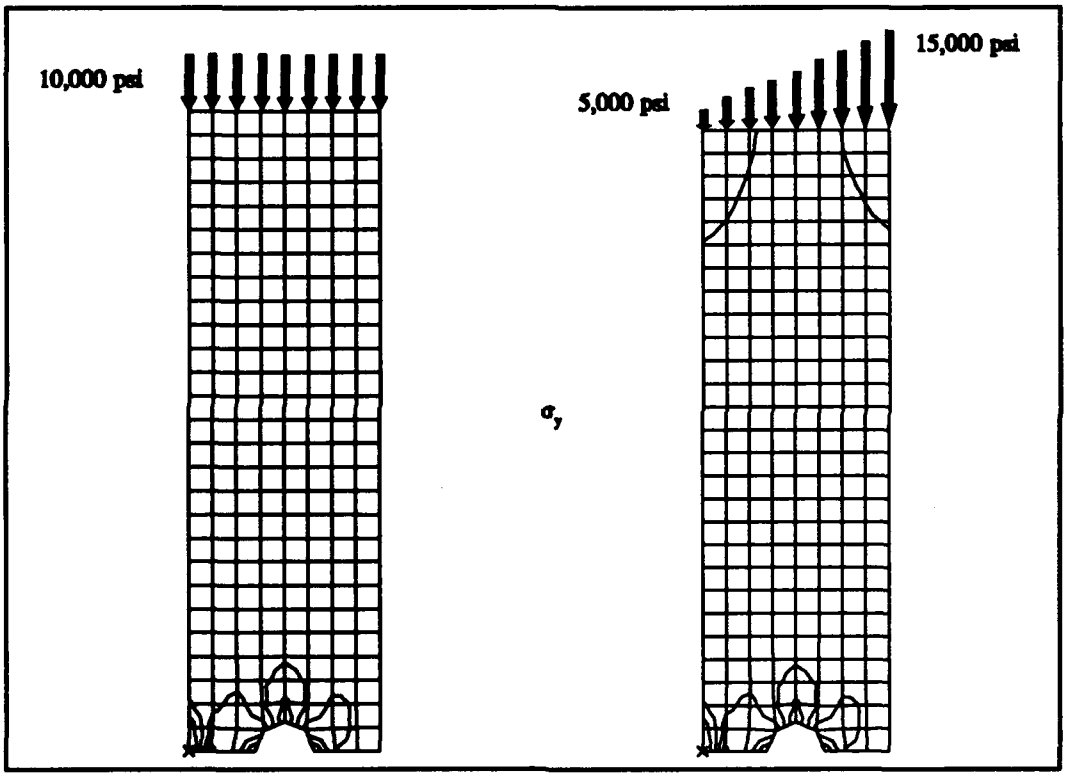

Figure C3 Stress comparisons for the DCDC templates with a uniform loading and a severe wedge loading

*From larger center hole to approximately one-quarter inch above fiber.

APPENDIX D

ESTIMATION OF FRICTIONAL GRAB PARAMETER CHARACTERIZING FIBER-MATRIX INTERFACES

The assumption that the fiber - matrix interface may be characterized by only the Frictional Grab parameter requires knowledge of the static coefficient of friction and normal residual stress at the interface, as well as the driving stress at the main crack in order to satisfy the equation:

$$FG = \mu \frac{\sigma_n}{\sigma_o} \qquad (1)$$

The coefficient of friction, μ, was determined experimentally using two small blocks and finding the tangent of the inclined angle at which slip initiated when the two blocks were resting on one another.

Pyrex fibers were introduced into a matrix of the same material by first drilling a hole for the fiber. Pyrex rods where than heated and drawn down until they could be slid through the fiber hole. The actual fiber used was than cut from the rod where the

diameter was slightly larger than that which slid through the hole. To insert the fiber into the matrix, the matrix was heated to approximately 700 °F at which time the room-temperature fiber was forced into the hole and the system was allowed to cool. The normal residual compressive stresses resulting from this process were estimated using the elasticity solution for internally and externally pressurized cylinders (Figure D1).

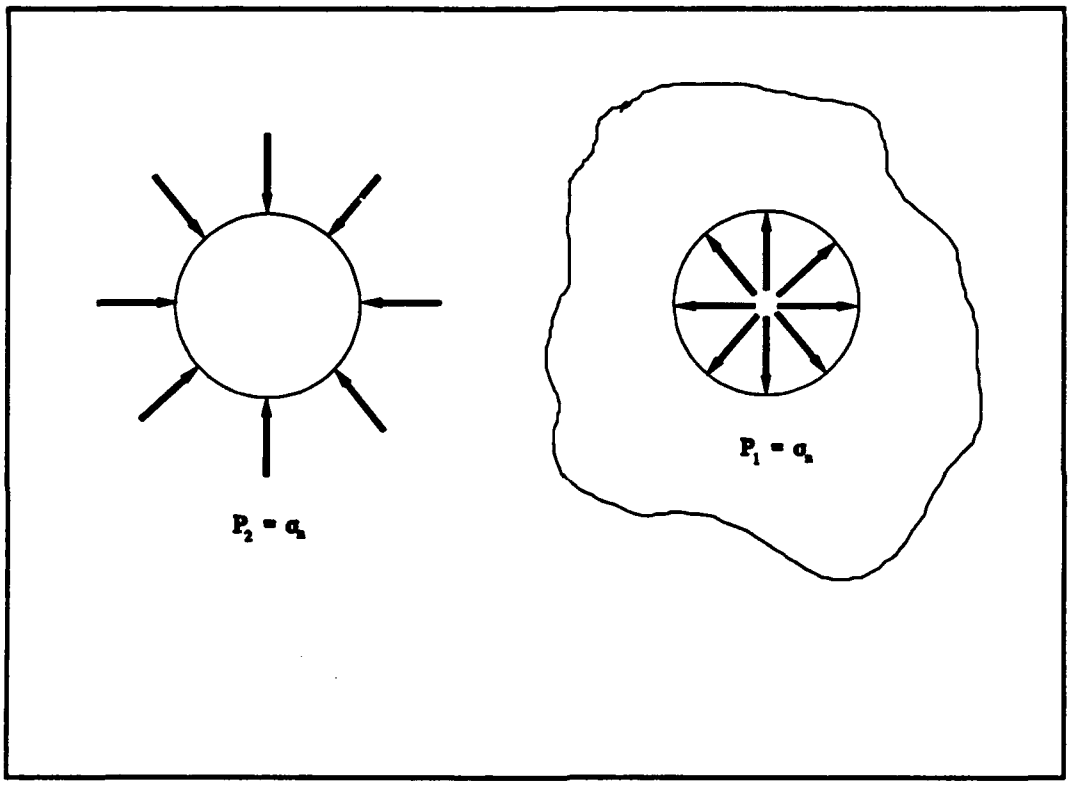

Figure D1 Residual interface stresses

As the matrix cools around the fiber, the resulting displacements are given by

$$u_f = -\frac{1-\nu}{E} P r_f \qquad u_m = \frac{1+\nu}{E} P r_m \tag{2}$$

Since the fiber was forced into the heated matrix, the fiber diameter is defined by

$$r_f = r_m + r_m \alpha(\Delta T) \tag{3}$$

Substituting Equation (3) into (2), the resulting pressure (normal residual compressive stress) is found to be defined by

$$P = \sigma_n = \frac{E\alpha(\delta T)}{2+(1-\nu)\alpha(\delta T)} \tag{4}$$

The epoxy was simply cured within the fiber hole to form the desired fibers. The epoxy does not to shrink upon curing;* however, there is a greater amount of mechanical interlocking since during curing the epoxy may flow into crevices created during drilling. To approximate this apparent increase in toughness, a small compressive stress was included in the computational analyses. A silicone release agent was added to weaken the interface by reducing the amount of interlocking which occurred.

---

* Based on manufacturers advice that the epoxy should not shrink for the given fiber size. At most, shrinkage may be 0.001 inches per inch.

An accurate assessment of μ and σ_n could be accomplished through push-out tests [16,17]; however, the epoxy fibers proved to be too ductile. The greater the axial force applied to the fiber, the greater the resistance from the Poisson expansion. The length of fiber was reduced until the fiber was successfully pushed-out; however, dominate edge removed any value from the data.

The computational analyses assume that fracture is driven by an internal pressure; whereas, the experiments were loaded at the far boundaries. The internal pressure is estimated by determining the stress required to obtain an equivalent bending moment for the specimen geometry (Figure D2).

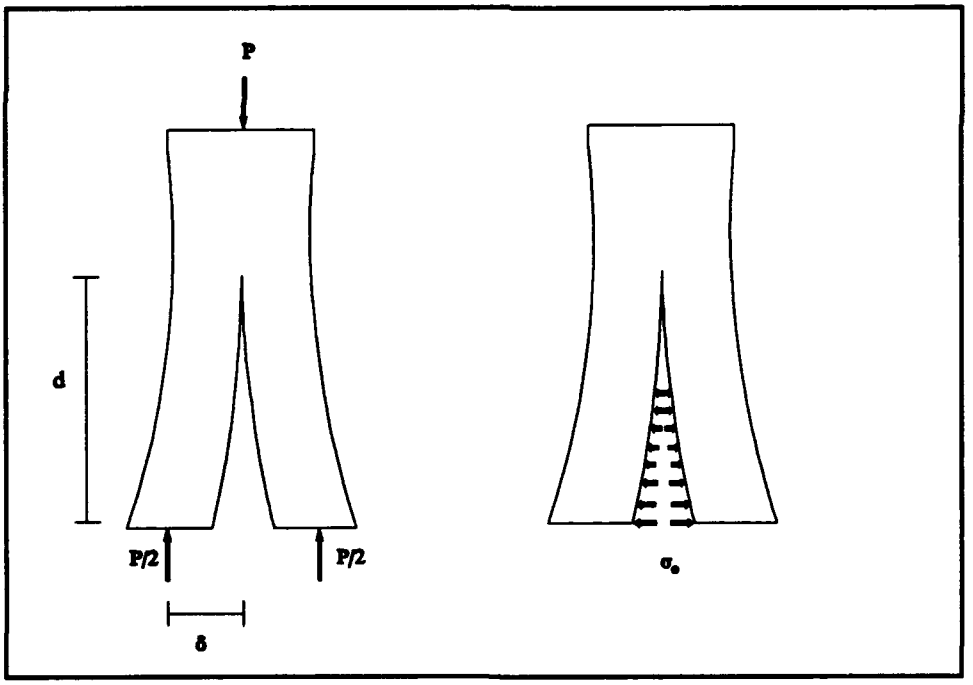

Figure D2 Determination of equivalent bending moments as an estimate for the internal driving pressure to be used in the computational analyses

The equivalent driving stress is found to be

$$\sigma_o = P(\frac{\delta}{d^2}) \qquad (5)$$

Table D-1 lists the results of this analysis.

Table D-1 Estimation of interfacial strength for model composite systems

	μ	σ_n / σ_o	Frictional Grab
Pyrex	0.23	13.0	3.0
Pyrex / oil	-	5.0	0.9
Epoxy	0.43	1.0	0.4
Epoxy / Silicone	0.59	0.3	0.2

APPENDIX E

DIGITIZED IMAGES OF CRACK FRONT

Computerized images were obtained from VHS tape as outlined in section 2.2.1. The following pages are digitally enhanced images taken from the original media. Several different cameras, lighting fixtures, magnifications, and specimens (size and quality) were used throughout this analysis. Therefore the figures which follow may appear inconsistent; however, they all attempt to show either the crack periphery or development of slip zones.

Figure: E1

Fiber: none

Comments:

Figure E1 illustrates the general shape of the crack front during fracture, as well as the procedures for measuring the half-crack length. The dark area at the bottom of the specimen is the top half of the main hole where the crack initiates. The arrow denotes the current position of the crack periphery.

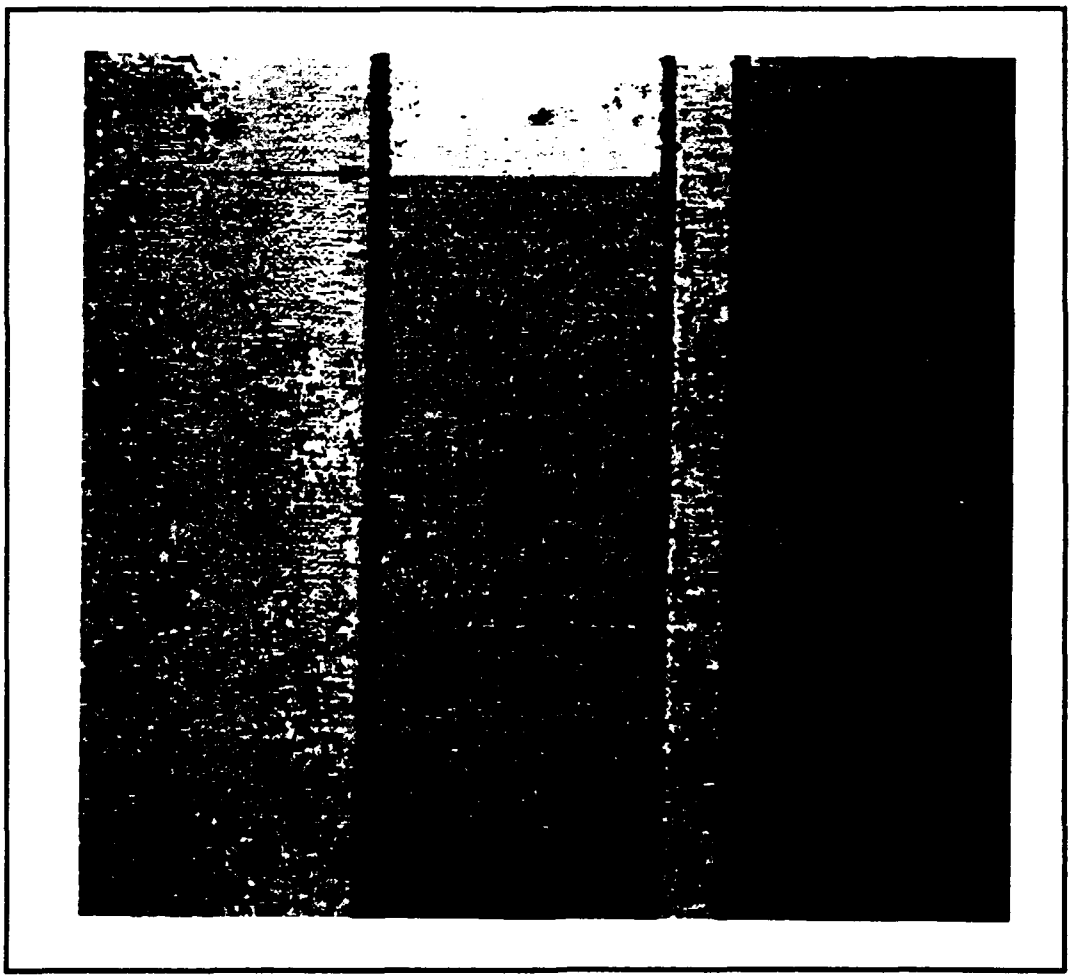

Figure E1 Fractured DCDC template illustrating crack-periphery shape

Figure: E2 through E5

Fiber: none

Comments:

1. The roughness just above what appears to be the fiber on Figure E3 is actually the back portion of the fiber. The camera was not looking down the fiber axis (as evident in Figure E2) and when filtered from a three-dimensional view to a two-dimensional view, the phantom obstruction resulted.

2. Figures E4 and E5 are two consecutive frames from the video tape. This is evident by noting that the edges of the periphery are at the same location. This sequence illustrates the dynamic jump which occurs as the fiber is sucked into the hole.

3. The jagged edge (far right) resulted when the template was cut from a large plate of glass.

Figure E2 Unfiltered image of crack periphery approaching hole

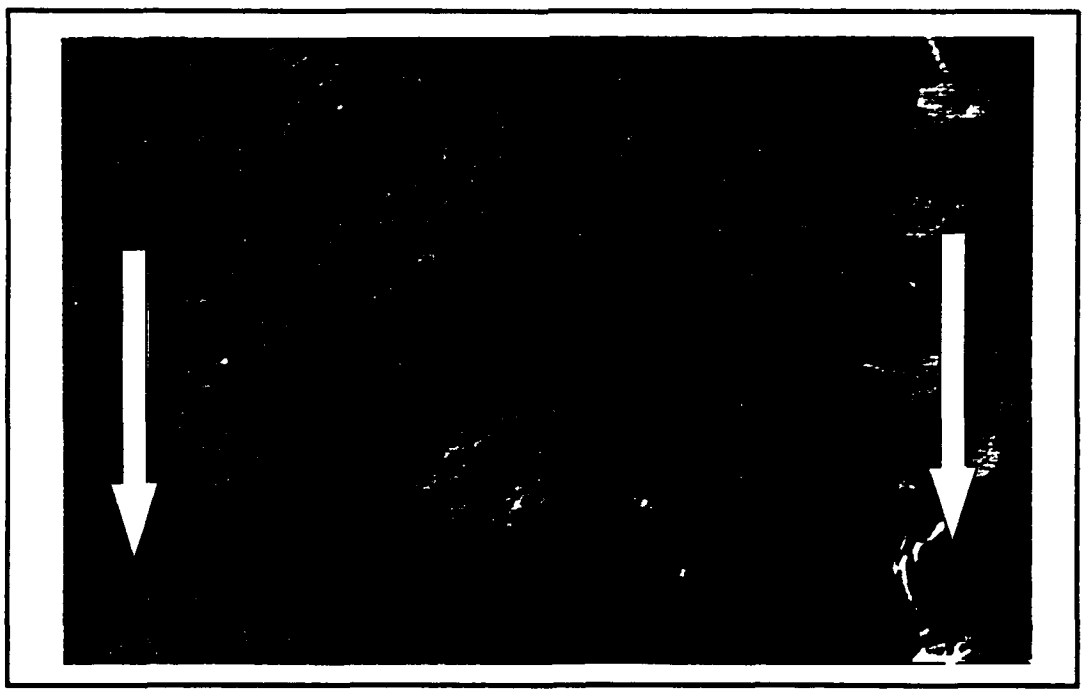

Figure E3 Embossed image of crack periphery approaching hole

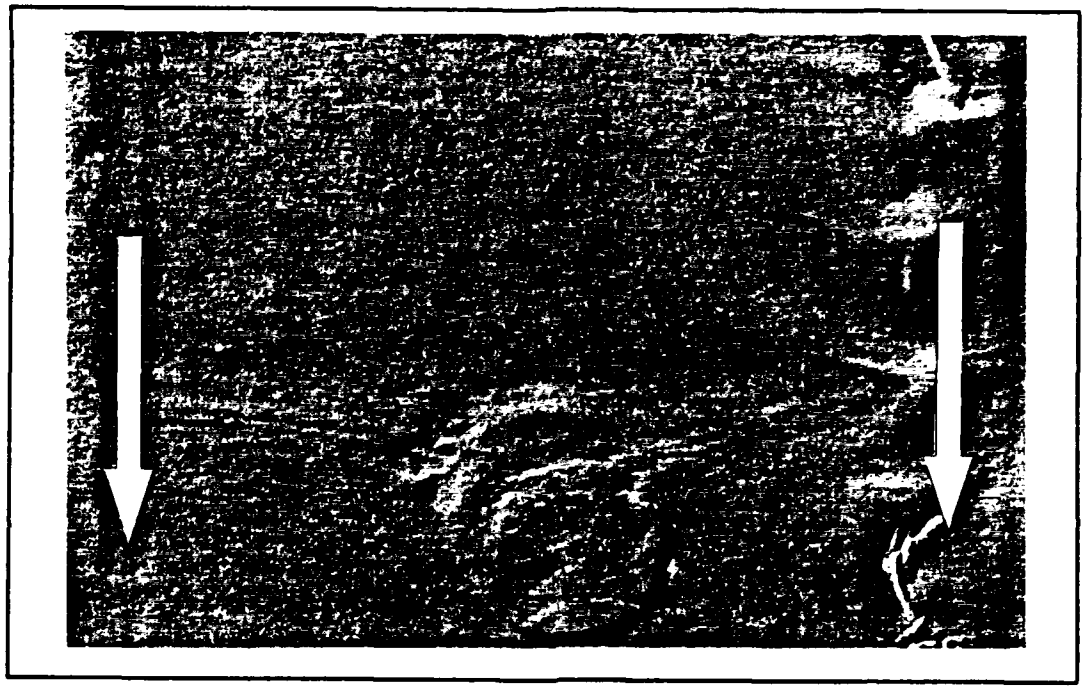

Figure E4 Embossed image of crack periphery snapping into the hole

Figure E5 Embossed image of crack periphery growing around the hole

Figure: E6 and E7

Fiber: none

Comments:

1. By shining a bright light at a specific angle relative to the camera and crack plane, color contours could be observed (Figure E6). If the stress is relieved, the contours disperse (Figure E7). When the specimen is reloaded, these bands begin to form and coalesce at the crack tip once again. These contours are visible to the naked eye during (and after) testing.

2. The glare which is the same in the two figures is produced from the bright light which was required to record the contours.

Figure E6 Stress contours due to fracture when specimen is loaded

Figure E7 Stress contours due to fracture when specimen is unloaded

Figure: E8

Fiber: hole

Comments:

1. During this test, a crack first initiated from the fiber hole. Eventually, a second crack popped-in from the larger central hole. The interaction between the two orthogonal cracks is interesting since in theory we assume that two perpendicular, mode I, cracks are independent.

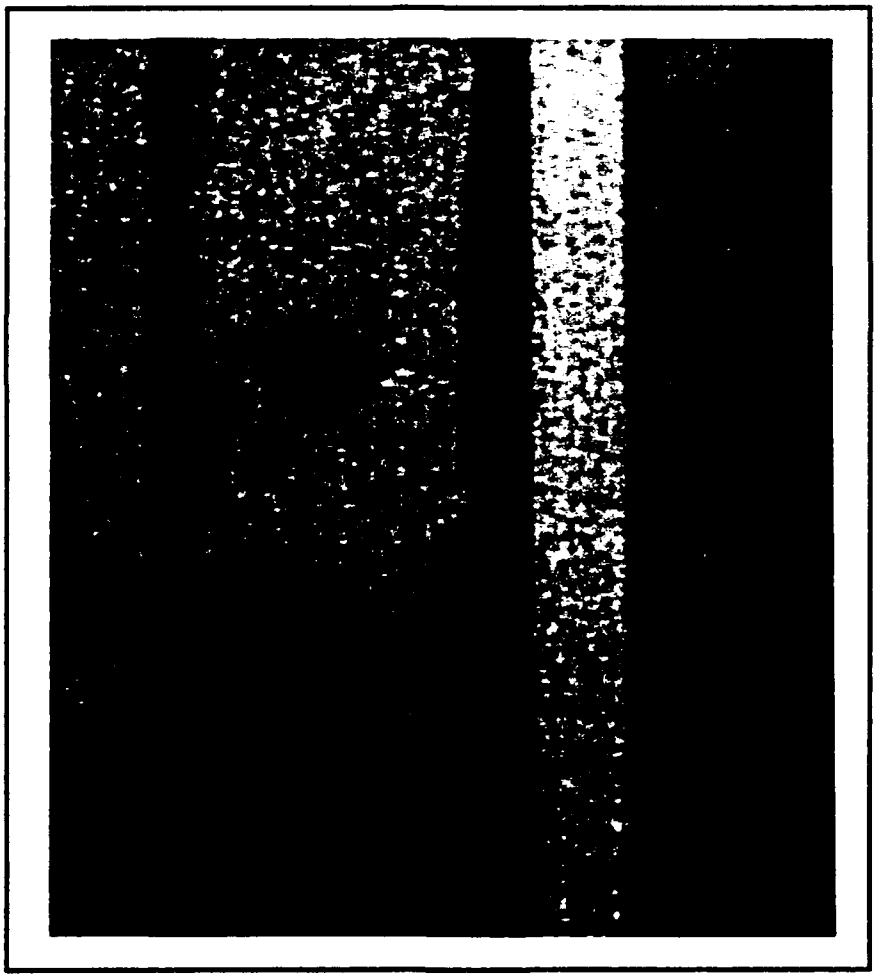

Figure E8 Interaction of mutually orthogonal cracks

Figure: E9 through E11

Fiber: hole, epoxy, and glass (respectively)

Comments:

1. The following three images are actual pictures of the crack periphery at different times which have been captured off of the VHS tape. The images have been digitally enhanced and superimposed to illustrated a time history of growth around the inclusions.

2. The dark spots and line (upper right of fiber) are actually dust particles which were on the camera lens.

3. The jagged appearance of the periphery resulted from the computer imaging. In reality, the periphery does not have any sudden changes in slope.

A. Hole (Figure E9)

The crack dynamically snaps into the hole due to the influence of the free surface. As the fracture continues around the hole, growth in retarded near the free surface since the crack must not only advance but also follow the circumference of the hole. The two crack halves continue around the hole and eventually snap together a fair distance above the inclusion. Interestingly, the crack dynamically enters and exits the inclusion.

B. Epoxy (Figure E10)

The crack again snaps into the fiber; however, the distance from the periphery to the fiber is much less than in the previous case. The two halves of the crack continue around the fiber until the meet at the top, and the fracture continues with a slight concave bow. Eventually, the crack front assumes its initial shape (flat) again.

C. Glass (Figure E11)

For the case of a strong interface, the periphery remains relatively flat for the entire growth sequence. This is attributed to the fact the crack-tip stresses are transmitted across the interface with little dissipation. The two halves of the crack snap together upon exiting fiber (as necessary for the periphery to remain flat).

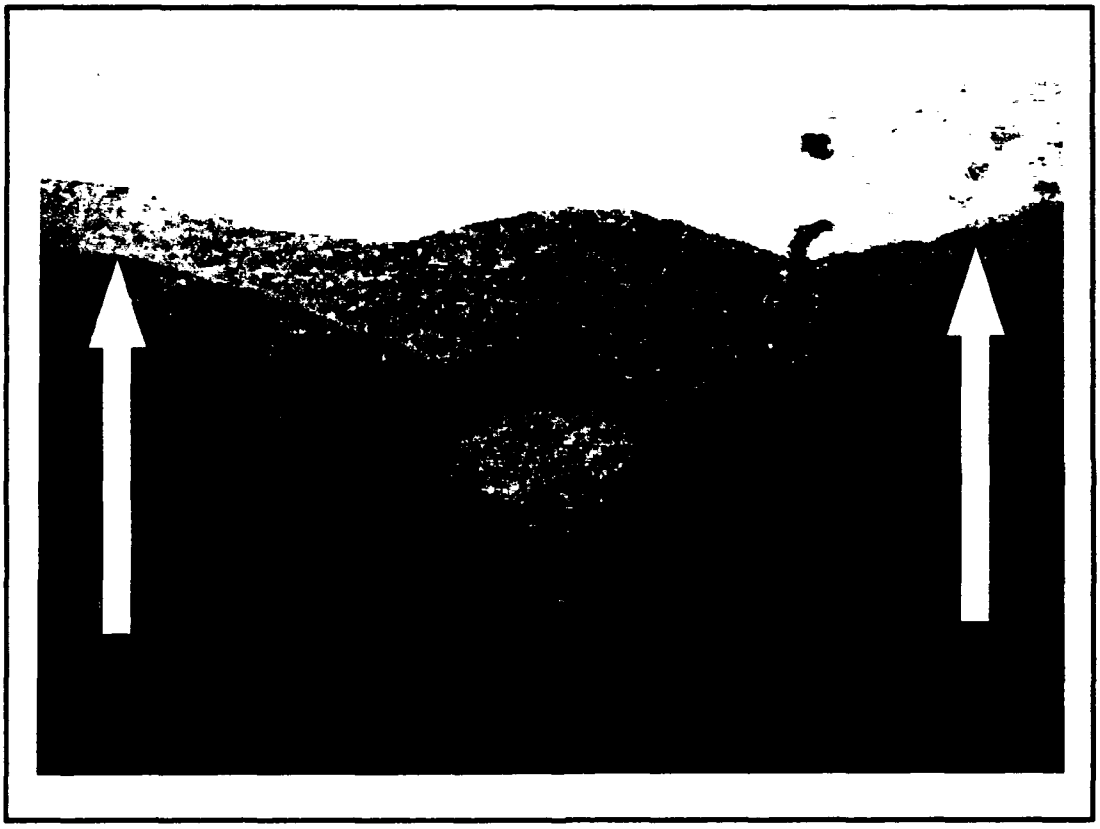

Figure E9 Experimentally determined crack propagation history around a hole

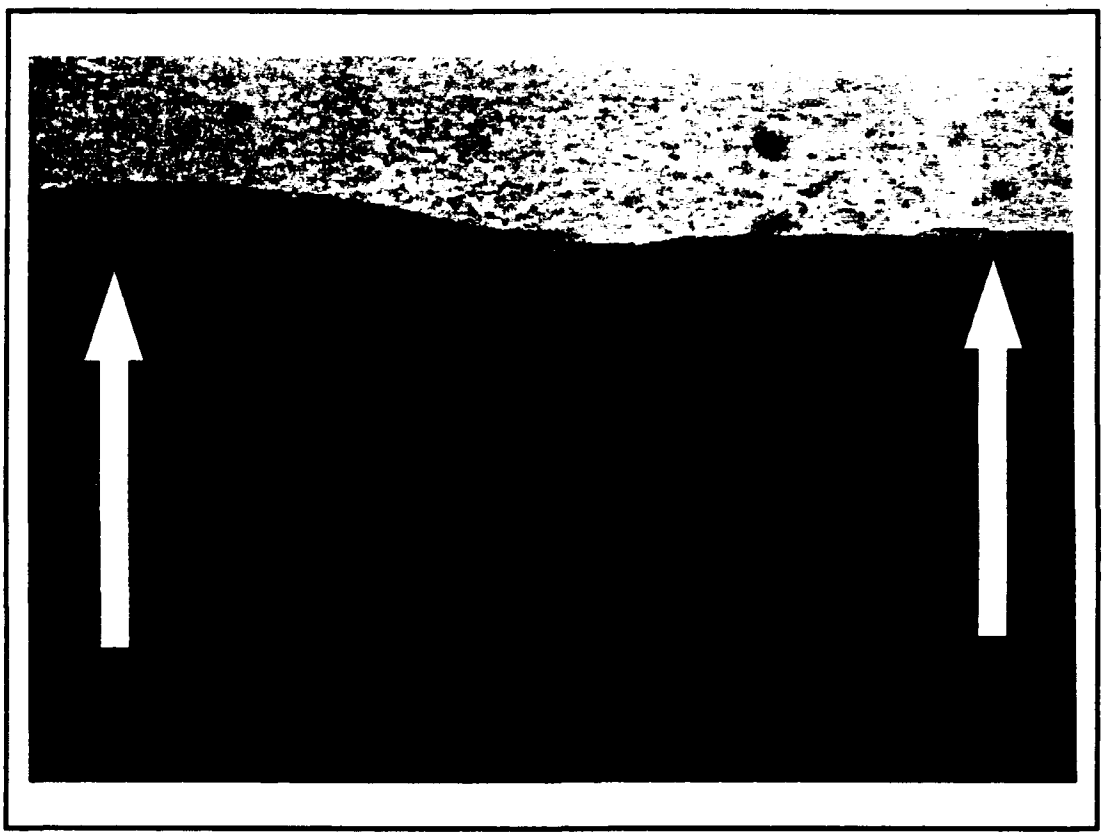

Figure E10 Experimentally determined crack propagation history around an epoxy inclusion

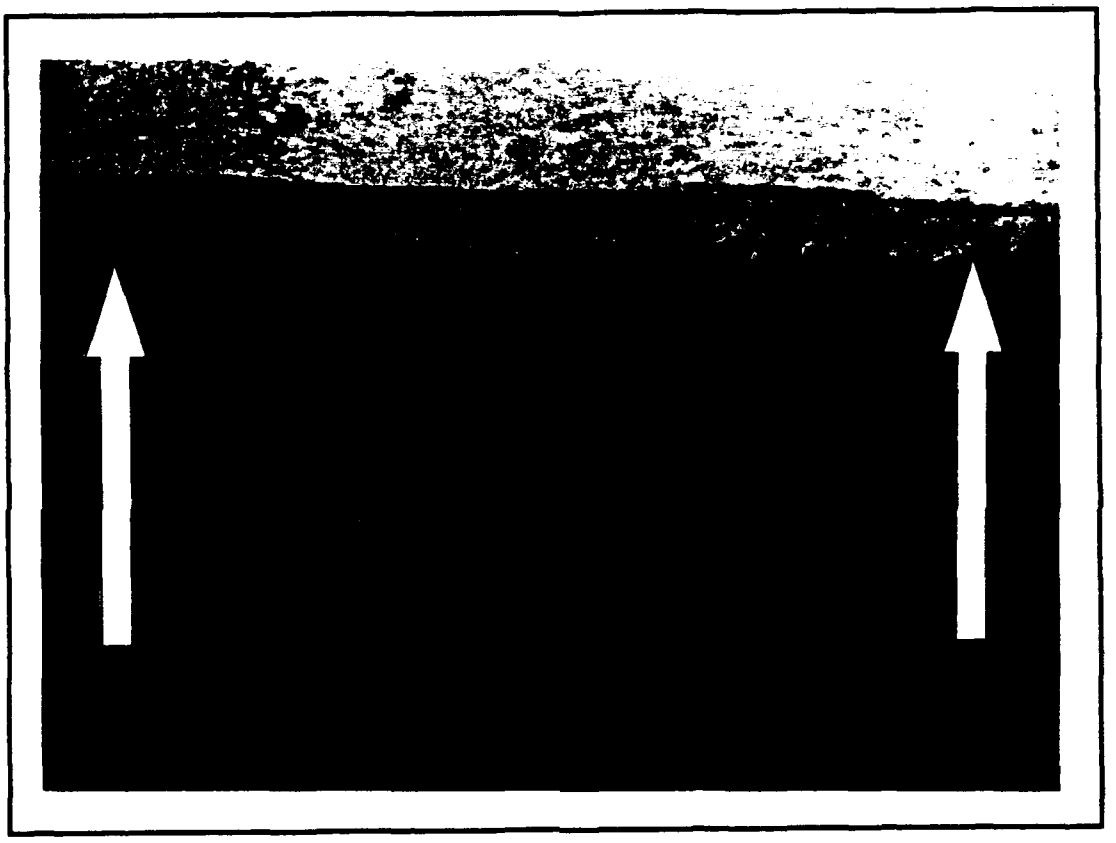

Figure E11 Experimentally determined crack propagation history around a glass inclusion

Figure: E12 through E14

Fiber: Epoxy

Comments:

The following sequence of photographs illustrate the development of frictional slip zones along an interface due to the presence of crack-tip stress fields. Figure E13 shows the tendency for weaker interfaces to debond prior to the main crack reaching the interface. Note that a matrix crack initiates well off the crack plane. This supports are assumption that the maximum stresses are above the crack plane. Figure E14 illustrates the amount of debonding and matrix cracks characterized by a bridging fiber.

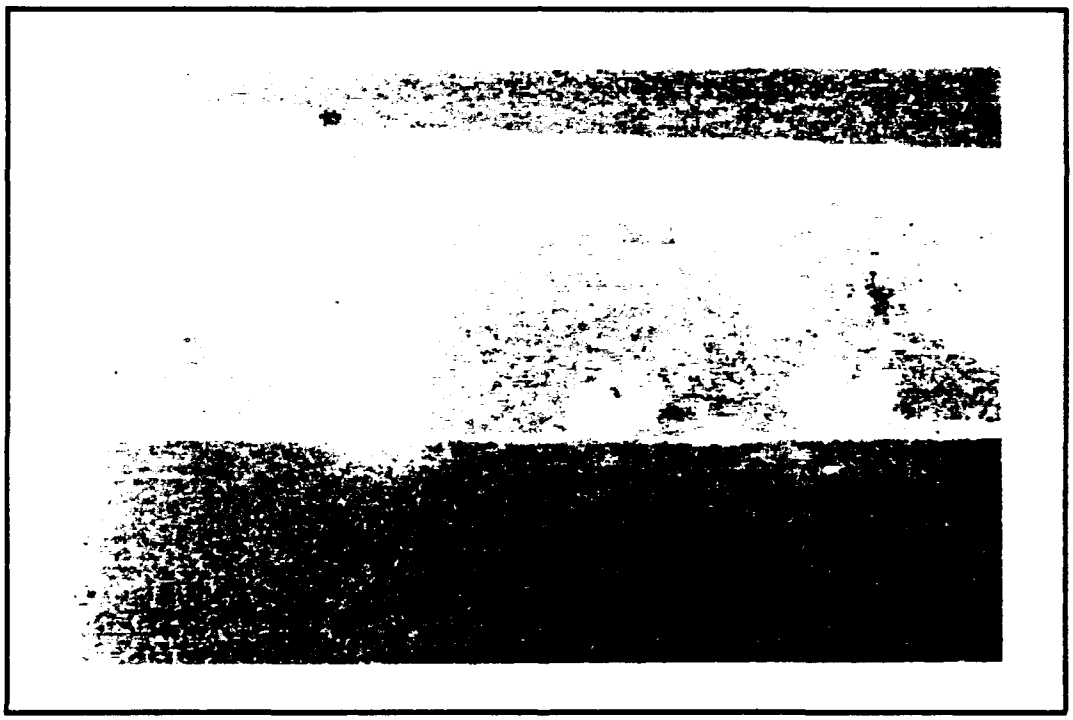

Figure E12 Fiber (epoxy) - matrix interface prior to fracture

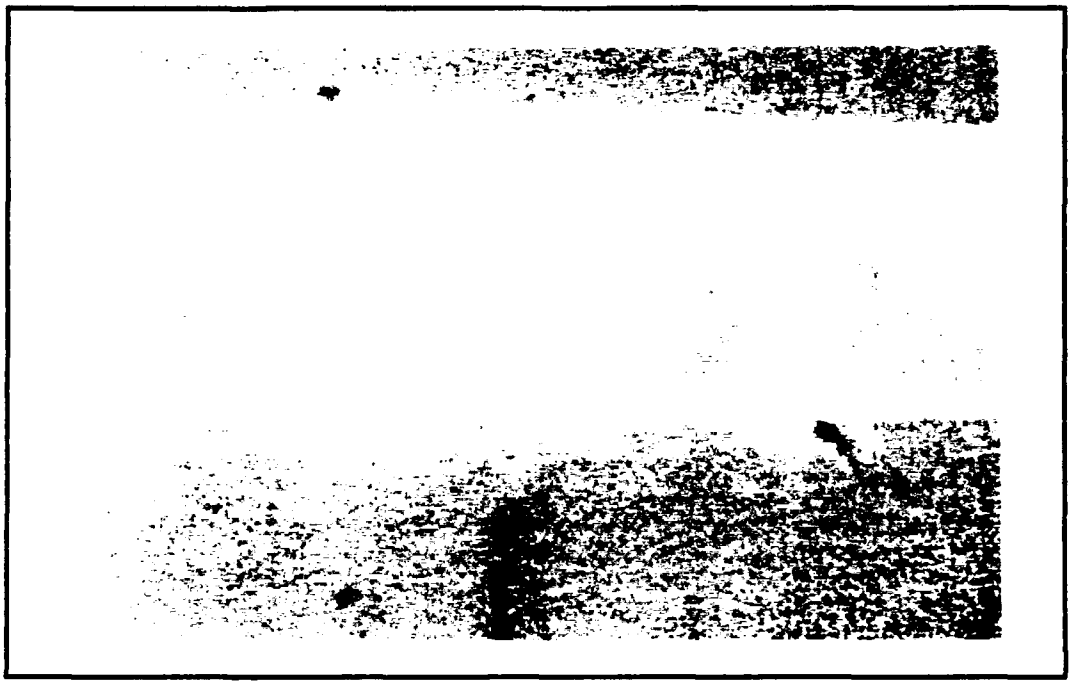

Figure E13 Fiber - matrix interface just prior to arrival of the main crack

Figure E14 Interfacial damage representative of bridging fibers

Figure: E15 and E16

Fiber: glass

Comments:

Strong interfaces are characterized by limited interfacial energy dissipation. As predicted, only a small area of the interface slips during fracture. Further, frictional sliding does not initiate until the fracture reaches the interface.

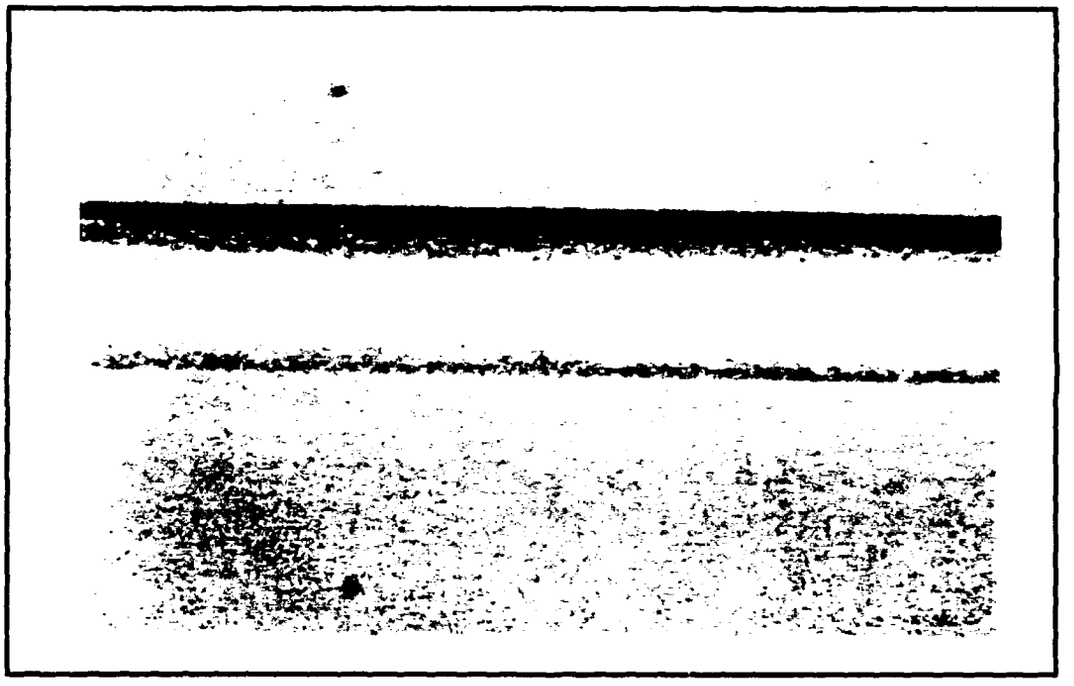

Figure E15 Fiber (glass) - matrix interface prior to fracture

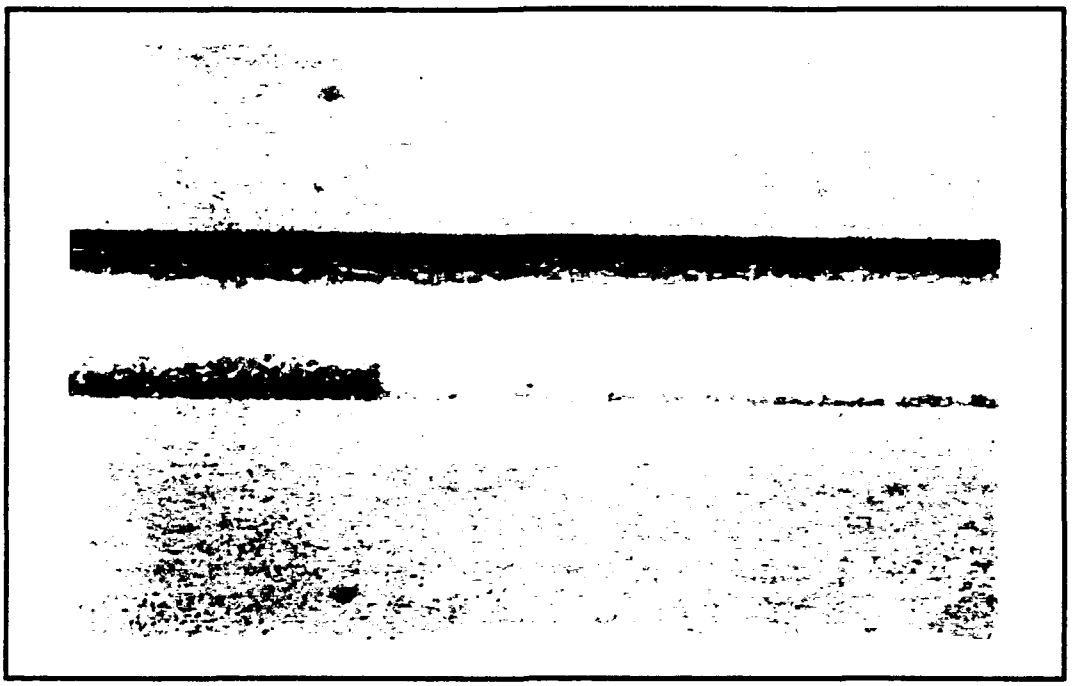

Figure E16 Interfacial slip for crack growth around first quarter of the fiber

The fracture is located near the bottom of the fiber where the dark and light regions meet. Just to the right of this mark, the light area transitions into a gray zone. The area between these two marks is the region of interfacial slip

APPENDIX F

INDIRECT BOUNDARY ELEMENT TECHNIQUES AS APPLIED TO LINEAR ELASTIC FRACTURE MECHANICS

1. Introduction

This appendix outlines, in detail, indirect boundary element methods (BEM) and their applicability to fracture mechanics problems as outlined by Crouch [9] and Larson [19]. Standard finite element techniques are being replaced by boundary element methods for specific classes of problems since BEM reduce the system of linear algebraic equations which needs to be solved, since only surfaces, not volumes, need be discretized. The numerical elasticity solution is determined through superposition of a finite distribution of analytical singular solutions (to known influence or Green's functions [18]) which exactly satisfy the governing partial differential equations in $\Re$, the region of interest.

Consider, as an example, the finite region, $\Re$, enclosed by a bounding curve, $\mathbf{C}$ (Figure F1 (a)). The elasticity solutions to region $\Re$ may be well approximated by considering a similar region $\Re^*$ (enclosed by $\mathbf{C}^*$) within an infinite region (Figure F1 (b)). Since analytical solutions to the governing PDE exists for case (b), the solution is obtained with less work. The trick, however, is to insure the results in case (b) truly represents those posed by (a).

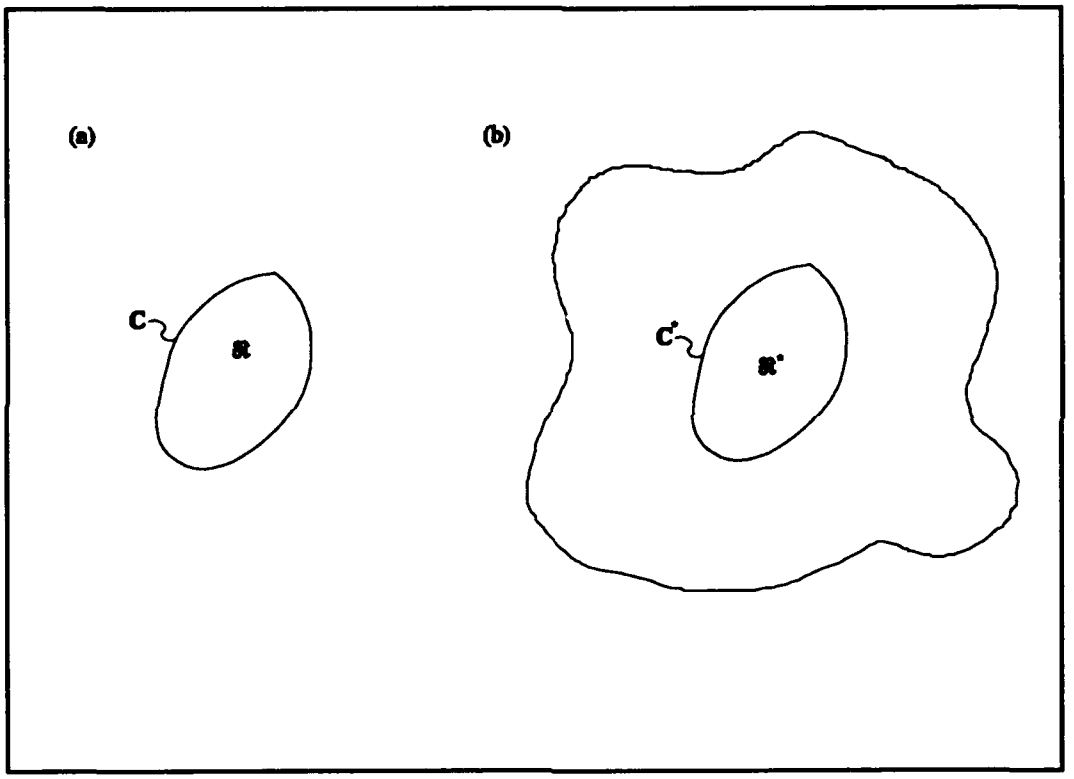

Figure F1 Regions of interest considered in boundary element formulations

Assume the above region, $\Re^*$, is a centrally-located, pressurized crack. The stresses within the body may be determined by dividing the crack periphery, $\mathbf{C}^*$, into a finite number of discrete elements, N. The elastic response due to any element, i, is defined

by a fundamental singular solution which not only becomes the kernel (singular integrand) of our governing integral equation but also has the physical characteristics of representing the crack opening displacement (or strength of the singularity), δ. The objective than is to determine a linear combination of singularity strengths (δ_i (i = 1..N)) which satisfy the prescribed boundary condition (opening pressure applied to the crack) at discrete (collocation) points along the crack surface. Theoretically, if a closed form solution to the governing integral equation could be determined in considering $\mathbf{C}^*$, the solution would be exact; however, inaccuracies are created from numerical discretization and integration procedures. The error tends toward zero as N approaches infinity. Once all the δ_i's are known, the solution for any point within $\Re^*$ (or equivalently $\Re$) may be determined. Since solutions are not constructed at discrete nodal coordinates, as in standard finite element techniques, the solution has the potential of being more accurate since interpolation is not required.

2. Fundamental Solution

Stress and displacements induced by a crack in an infinite medium are derived by integrating the effects of dislocation densities [9] along the fracture surface which are defined by Kelvin's plane strain solution for a point force in an infinite medium. The displacement discontinuities are the difference between the displacement on the upper (positive side of the crack, $y = 0_+$) and lower (negative side $y = 0_-$) as defined in Equation (11). (Section 3 discusses dislocation densities and force dipoles in detail). These

dislocation densities, or force dipoles, are constructed in the limit as two opposing point forces converge (Figure 3.1). The dipole represents a point of infinite strain, or equivalently, a finite displacement between two infinitesimal surfaces. A continuous distribution of such dipoles is used to model the crack.

Therefore in order to better understand the theory behind BEM, we must first investigate Kelvin's solution for a point force in an infinite medium. Figure F2 illustrates such a force, F_i, whose dimensions are force per unit length, and projections onto the coordinate axis are F_x and F_y respectively.

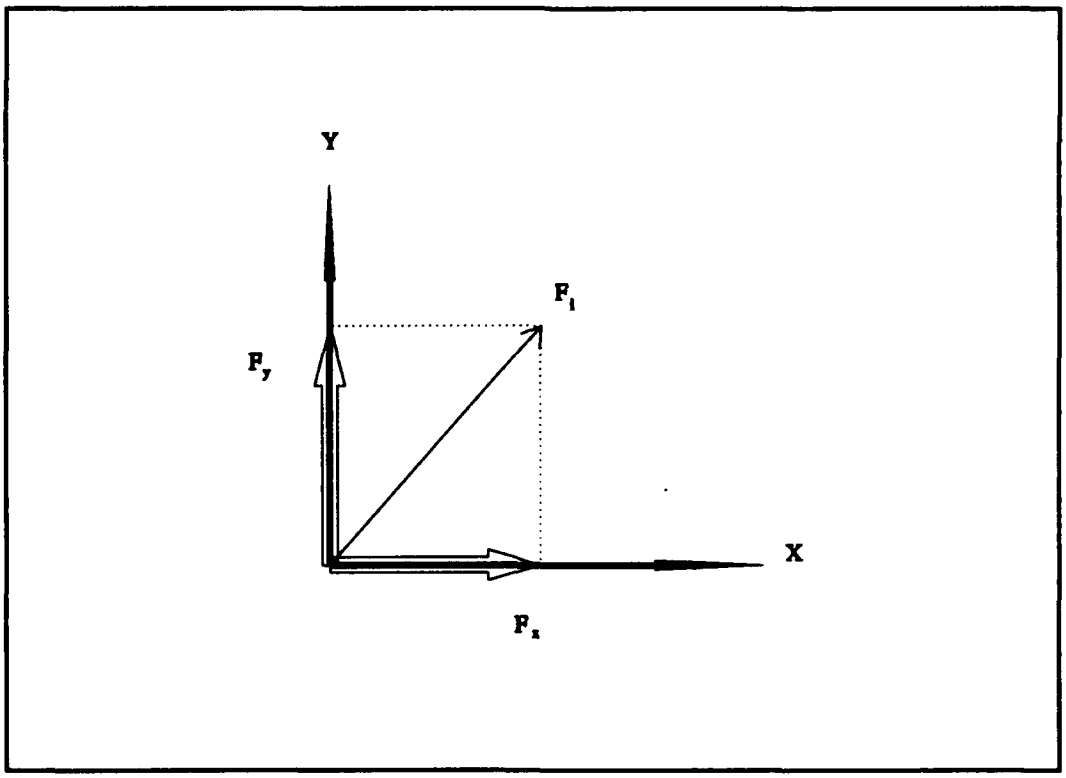

Figure F2 Point force in an infinite medium

Kelvin determined that the solution to the stresses and displacements are characterized by the function g(x,y) and its derivatives where

$$g(x,y) = \frac{-1}{4\pi(1-\nu)}\ln\sqrt{(x^2+y^2)} \tag{1}$$

Reference Crouch [32f] for the development of Equation (1). The derivatives to Equation (1) are directly evaluated as shown below.

$$\begin{aligned} g_{,x} &= \frac{-1}{4\pi(1-\nu)}\frac{x}{x^2+y^2} \\ g_{,y} &= \frac{-1}{4\pi(1-\nu)}\frac{y}{x^2+y^2} \\ g_{,xy} &= \frac{+1}{4\pi(1-\nu)}\frac{2xy}{(x^2+y^2)^2} \\ g_{,xx} &= -g_{,yy} = \frac{+1}{4\pi(1-\nu)}\frac{x^2-y^2}{(x^2+y^2)^2} \end{aligned} \tag{2}$$

where $g_{,x}$ indicates partial differentiation with respect to x. Kelvin determined that the displacements within the body are defined by

$$\begin{aligned} u_x &= \frac{F_x}{2G}[(3-4\nu)g - xg_{,x}] + \frac{F_y}{2G}[-yg_{,x}] \\ u_y &= \frac{F_y}{2G}[(3-4\nu)g - yg_{,y}] + \frac{F_x}{2G}[-xg_{,y}] \end{aligned} \tag{3}$$

where G is the shear modulus. Linear strain and stresses are determined subsequently using Equation (4)

$$e_{ij} = \frac{1}{2}(u_{i,j}+u_{j,i})$$
$$\sigma_{ij} = 2G[e_{ij}+\frac{\nu}{1-2\nu}e_{kk}\delta_{ij}] \quad (4)$$

Substituting Equation (3) into Equation (4), the stresses are found to be:

$$\begin{aligned}\sigma_{xx} &= F_x[2(1-\nu)g_{,x}-xg_{,xx}]+F_y[2\nu g_{,y}-yg_{,xx}]\\ \sigma_{yy} &= F_x[2\nu g_{,x}-xg_{,yy}]+F_y[2(1-\nu)g_{,y}-yg_{,yy}]\\ \sigma_{xy} &= F_x[(1-2\nu)g_{,y}-xg_{,xy}]+F_y[(1-2\nu)g_{,x}-yg_{,xy}]\end{aligned} \quad (5)$$

The next step in determining the fundamental solution to the pressurized crack problem is to examine a continuous distribution of point forces along the fracture surface. Figure F3 illustrates the related problem of a constant stress, or traction, over a discrete line boundary which is representative of one side of our two dimensional pressurized crack. Since the solution for each individual point force is characterized by g(x,y), the total result of the line intensity is obtained through a straight forward integration of the original solution as expressed in Equation (6).

$$\begin{aligned}f(x,y) &= \int_{-a}^{a} g(x-\xi,y)d\xi\\ &= \frac{-1}{4\pi(1-\nu)}[y(\arctan\frac{y}{x-a}-\arctan\frac{y}{x+a})\\ &-(x-a)\ln\sqrt{[(x-a)^2+y^2]}\\ &+(x+a)\ln\sqrt{[(x+a)^2+y^2]}\end{aligned} \quad (6)$$

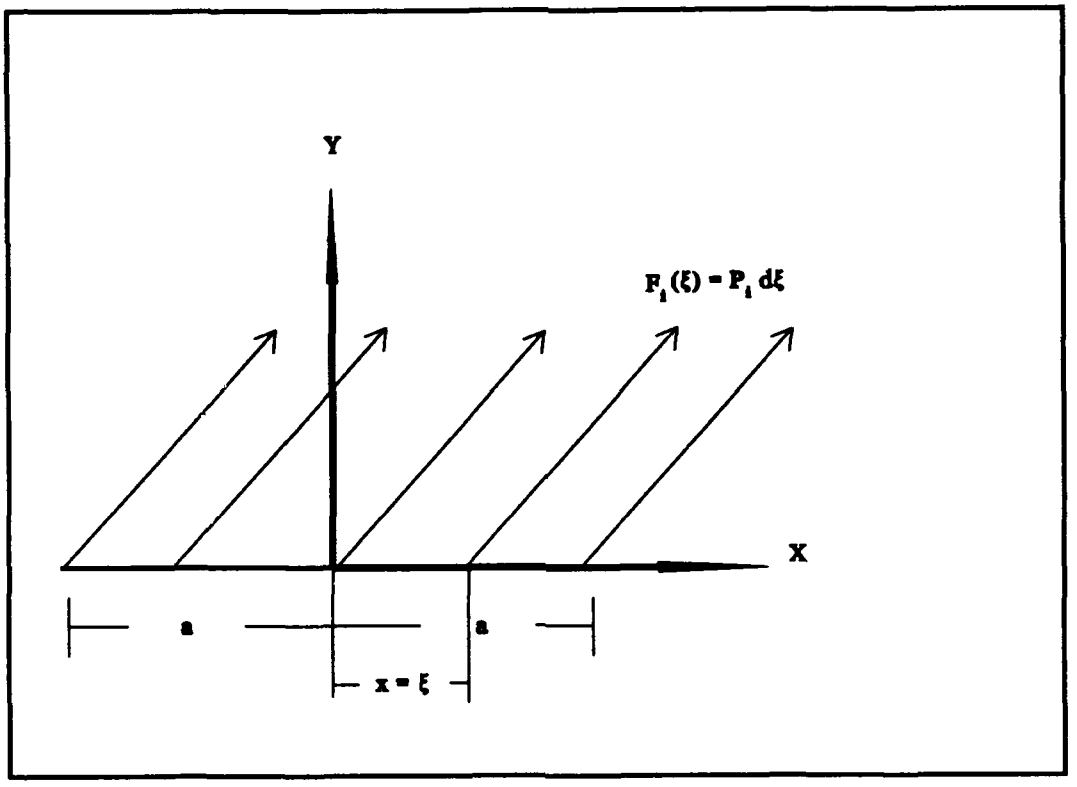

Figure F3 Line intensity representing one half of a two dimensional pressurized crack of length 2a

Using the same procedure as before, Kelvin obtained the following displacement and stress solution to the problem shown in Figure F3.

$$
\begin{aligned}
u_x &= \frac{P_x}{2G}[(3-4\nu)f+yf_{,y}]+\frac{P_y}{2G}[-yf_{,x}] \\
u_y &= \frac{P_x}{2G}[-yf_{,x}]+\frac{P_y}{2G}[(3-4\nu)f-yf_{,y}] \\
\sigma_{xx} &= P_x[(3-2\nu)f_{,x}+yf_{,xy}]+P_y[2\nu f_{,y}+yf_{,yy}] \\
\sigma_{yy} &= P_x[(2\nu-1)f_{,x}-yf_{,xy}]+P_y[2(1-\nu)f_{,y}-yf_{,yy}] \\
\sigma_{xy} &= P_x[2(1-\nu)f_{,y}+yf_{,yy}]+P_y[(1-2\nu)f_{,x}-yf_{,xy}]
\end{aligned}
\qquad (7)
$$

where P_i is defined by $F_i(\xi) = P_i\, d\xi$ and the derivatives of function f(x,y) are defined by Equation (8). $d\xi$ is the infinitesimal area over which a single point force acts.

$$
\begin{aligned}
f_{,x} &= \frac{+1}{4\pi(1-\nu)}\left[\ln\sqrt{[(x-a)^2+y^2]} - \ln\sqrt{(x+a)^2+y^2]}\right] \\
f_{,y} &= \frac{-1}{4\pi(1-\nu)}\left[\arctan\frac{y}{x-a} - \arctan\frac{y}{x+a}\right] \\
f_{,x} &= \frac{+1}{4\pi(1-\nu)}\left[\frac{y}{(x-a)^2+y^2} - \frac{y}{(x+a)^2+y^2}\right] \\
f_{,xx} &= -f_{,yy} = \frac{+1}{4\pi(1-\nu)}\left[\frac{x-a}{(x-a)^2+y^2} - \frac{x-a}{(x+a)^2+y^2}\right]
\end{aligned}
\qquad \textbf{(8)}
$$

Note that each discrete element is referenced in a local frame of reference as illustrated in Figure F4, and therefore must be transformed globally in order to develop the proper set of linear equations. The resulting global displacements and stresses are given by Equations (9) and (10).

$$
\begin{aligned}
u_x &= \frac{P_{\bar{x}}}{2G}\left[(3-4\nu)\cos\beta\bar{F}_1 + \bar{y}(\sin\beta\bar{F}_2 + \cos\beta\bar{F}_3\right] \\
&\quad + \frac{P_{\bar{y}}}{2G}\left[(4\nu-3)\sin\beta\bar{F}_1 - \bar{y}(\cos\beta\bar{F}_2 - \sin\beta\bar{F}_3)\right] \\
u_y &= \frac{P_{\bar{x}}}{2G}\left[(3-4\nu)\sin\beta\bar{F}_1 + \bar{y}(\cos\beta\bar{F}_2 - \sin\beta\bar{F}_3\right] \\
&\quad + \frac{P_{\bar{y}}}{2G}\left[(3-4\nu)\cos\beta\bar{F}_1 - \bar{y}(\sin\beta\bar{F}_2 + \cos\beta\bar{F}_3)\right] \\
\sigma_{xx} &= P_{\bar{x}}[\bar{F}_2 + 2(1-\nu)(\cos(2\beta)\bar{F}_2 - \sin(2\beta)\bar{F}_3) + \bar{y}(\cos(2\beta)\bar{F}_4 + \sin(2\beta)\bar{F}_5)] \\
&\quad + P_{\bar{y}}[\bar{F}_3 - (1-2\nu)(\sin(2\beta)\bar{F}_2 + \cos(2\beta)\bar{F}_3) + \bar{y}(\sin(2\beta)\bar{F}_4 - \cos(2\beta)\bar{F}_5] \\
\sigma_{yy} &= P_{\bar{x}}[\bar{F}_2 - 2(1-\nu)(\cos(2\beta)\bar{F}_2 - \sin(2\beta)\bar{F}_3) - \bar{y}(\cos(2\beta)\bar{F}_4 + \sin(2\beta)\bar{F}_5)] \\
&\quad + P_{\bar{y}}[\bar{F}_3 + (1-2\nu)(\sin(2\beta)\bar{F}_2 + \cos(2\beta)\bar{F}_3) - \bar{y}(\sin(2\beta)\bar{F}_4 - \cos(2\beta)\bar{F}_5] \\
\sigma_{xy} &= P_{\bar{x}}[2(1-\nu)(\sin(2\beta)\bar{F}_2 + \cos(2\beta)\bar{F}_3) + \bar{y}(\sin(2\beta)\bar{F}_4 - \cos(2\beta)\bar{F}_5)] \\
&\quad + P_{\bar{y}}[(1-2\nu)(\cos(2\beta)\bar{F}_2 - \sin(2\beta)\bar{F}_3) - \bar{y}(\cos(2\beta)\bar{F}_4 + \sin(2\beta)\bar{F}_5]
\end{aligned}
\qquad \textbf{(9)}
$$

$$
\begin{aligned}
F_1(\bar{x},\bar{y}) &= f(\bar{x},\bar{y}) = \frac{-1}{4\pi(1-\nu)}[\bar{y}(\arctan\frac{\bar{y}}{\bar{x}-a} - \arctan\frac{\bar{y}}{\bar{x}+a}) \\
&\quad -(\bar{x}-a)\ln\sqrt{[(\bar{x}-a)^2+\bar{y}^2]} + (\bar{x}+a)\ln\sqrt{[(\bar{x}+a)^2+\bar{y}^2]}\,] \\
F_2(\bar{x},\bar{y}) &= f_{,\bar{x}} = \frac{+1}{4\pi(1-\nu)}[\ln\sqrt{[(\bar{x}-a)^2+\bar{y}^2]} - \ln\sqrt{[(\bar{x}+a)^2+\bar{y}^2]}\,] \\
F_3(\bar{x},\bar{y}) &= f_{,\bar{y}} = \frac{-1}{4\pi(1-\nu)}[\arctan\frac{\bar{y}}{\bar{x}-a} - \arctan\frac{\bar{y}}{\bar{x}+a}] \\
F_4(\bar{x},\bar{y}) &= f_{,\bar{x}\bar{y}} = \frac{+1}{4\pi(1-\nu)}[\frac{\bar{y}}{(\bar{x}-a)^2+\bar{y}^2} - \frac{\bar{y}}{(\bar{x}+a)^2+\bar{y}^2}] \\
F_5(\bar{x},\bar{y}) &= f_{,\bar{x}\bar{x}} = -f_{,\bar{y}\bar{y}} = \frac{+1}{4\pi(1-\nu)}[\frac{\bar{x}-a}{(\bar{x}-a)^2+\bar{y}^2} - \frac{\bar{x}+a}{(\bar{x}+a)^2+\bar{y}^2}] \\
F_6(\bar{x},\bar{y}) &= f_{,\bar{x}\bar{y}\bar{y}} = \frac{+1}{4\pi(1-\nu)}[\frac{(\bar{x}-a)^2-y^2}{((\bar{x}-a)^2+\bar{y}^2)^2} - \frac{(\bar{x}+a)^2-\bar{y}^2}{((\bar{x}+a)^2+\bar{y}^2)^2}] \\
F_7(\bar{x},\bar{y}) &= f_{,\bar{y}\bar{y}\bar{y}} = \frac{+2\bar{y}}{4\pi(1-\nu)}[\frac{(\bar{x}-a)}{((\bar{x}-a)^2+\bar{y}^2)^2} - \frac{(\bar{x}+a)}{((\bar{x}+a)^2+\bar{y}^2)^2}]
\end{aligned}
\qquad \textbf{(10)}
$$

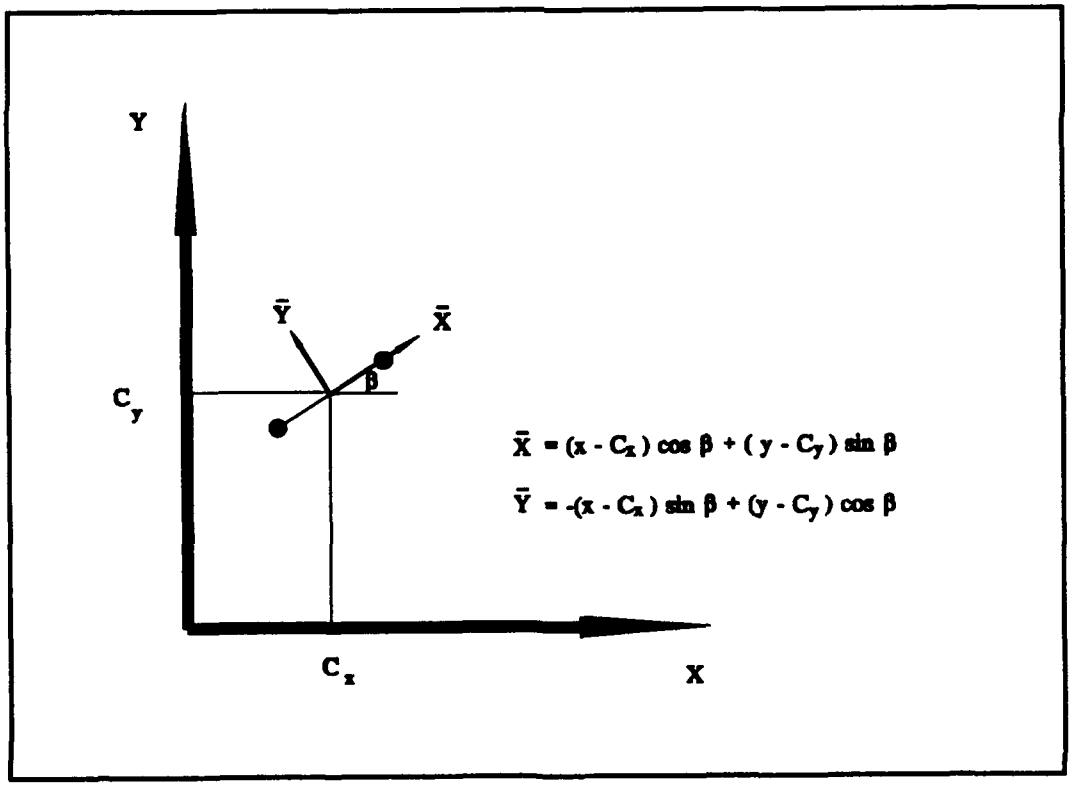

Figure F4 Coordinate transformations

The final step in the formulation of the elasticity solution is to consider the displacement discontinuity, D_i, between the positive side of the crack, denoted $y = 0_+$, and the negative side, denoted $y = 0_-$. D_i is, therefore defined by

$$D_i = u_i(x_i,0_-) - u_i(x_i,0_+) \tag{11}$$

Note that the resulting solution is equivalent to that obtained by Larson in representing the fractured surface as a continuous distribution of force dipoles ($D_i = K\delta_i$)*. The global displacement and stresses written in the local frame of reference for any element, i, can now be written as shown in Equation (12).

$$\begin{aligned}
u_x &= \delta_x[(2\nu-1)\sin\beta\bar{F}_2+2(1-\nu)\cos\beta\bar{F}_3+\bar{y}(\sin\beta\bar{F}_4-\cos\beta\bar{F}_5)] \\
&\quad +\delta_y[(2\nu-1)\cos\beta\bar{F}_2-2(1-\nu)\sin\beta\bar{F}_3-\bar{y}(\cos\beta\bar{F}_4+\sin\beta\bar{F}_5)] \\
u_y &= \delta_x[-(2\nu-1)\cos\beta\bar{F}_2+2(1-\nu)\sin\beta\bar{F}_3-\bar{y}(\cos\beta\bar{F}_4+\sin\beta\bar{F}_5)] \\
&\quad +\delta_y[(2\nu-1)\sin\beta\bar{F}_2+2(1-\nu)\cos\beta\bar{F}_3-\bar{y}(\sin\beta\bar{F}_4-\cos\beta\bar{F}_5)] \\
\sigma_{xx} &= 2G\delta_x[2\cos^2\beta\bar{F}_4+\sin(2\beta)\bar{F}_5+\bar{y}(\cos(2\beta)\bar{F}_6-\sin(2\beta)\bar{F}_7)] \\
&\quad +2G\delta_y[-\bar{F}_5+\bar{y}(\sin(2\beta)\bar{F}_6+\cos(2\beta)\bar{F}_7)] \\
\sigma_{yy} &= 2G\delta_x[2\sin^2\beta\bar{F}_4-\sin(2\beta)\bar{F}_5-\bar{y}(\cos(2\beta)\bar{F}_6-\sin(2\beta)\bar{F}_7)] \\
&\quad +2G\delta_y[-\bar{F}_5-\bar{y}(\sin(2\beta)\bar{F}_6+\cos(2\beta)\bar{F}_7)] \\
\sigma_{xx} &= 2G\delta_x[\sin(2\beta)\bar{F}_4-\cos(2\beta)\bar{F}_5+\bar{y}(\sin(2\beta)\bar{F}_6+\cos(2\beta)\bar{F}_7)] \\
&\quad +2G\delta_y[-\bar{y}(\cos(2\beta)\bar{F}_6-\sin(2\beta)\bar{F}_7)]
\end{aligned} \tag{12}$$

---

*Indirect boundary element methods integrate Kelvin's point force solution on both sides of the crack surface ($y = 0_+$ and $y = 0_-$) and determine dislocation densities via a limiting process. Surface integral techniques incorporate force dipoles which are created via the same limiting process of two Kelvin point forces. The solution is obtained with a single integration of the new fundamental solution. The results are the same, only the mathematical procedure in interchanged. Section 2.1 details the differences between the two methods, as well as the solution for the constant K.

For simplicity, express the stress components in Equation (12) as

$$\sigma_{ij}(x_i) = \Gamma(\bar{F})\delta_i(x_i) \tag{13}$$

Recalling that σ_{ij} is our prescribed boundary conditions, the total crack opening displacement at any point is found by summing the effects of a continuous distribution of dislocation densities (force dipoles) over the crack domain.

$$\sigma_{ij}(x_i) = \int_{-a}^{a}\Gamma(\bar{F})\delta_i(x_i)dA \tag{14}$$

If Equation (14) could be directly integrated over the crack surface, the exact solution to the problem would be obtained. Since this is impractical, the crack domain is divided into N discrete elements where the boundary conditions are exactly satisfied at a single collocation point. This results in a discontinuity in displacement across each element creating a stair-step approximation for a continuous crack opening displacement. This numerical technique well approximates the analytical solution provided small enough elements are incorporated. Since δ_i is assumed constant across each element*, the final solution is determined by the following set of linear equations.

$$\sigma_{ij}(x_i) = \sum_{i=0}^{N}\delta_i\int\Gamma(\bar{F})dA \tag{15}$$

---

*Reference chapter three (page 3-10) for exceptions.

Note that $\Gamma(F)$ is completely defined by the material properties and geometric boundary conditions. Given these parameters, Equation (15) can be written as

$$\tilde{\sigma} = [C]\tilde{\delta} \tag{16}$$

where C is known as the matrix of influence coefficients satisfying Equation (12).

The problem of interest to this study is a pressurized crack near an interface. The initial prescribed boundary conditions are the applied tractions along the crack surface and the initial displacements along the interface which are assumed to be zero. Partitioning of the influence coefficient matrix allows direct determination of unknown crack displacements according to Equation (17). Once the unknown crack displacements have been determined, the stresses are updated using the following conditions:

(1) If the interfacial shear stress is less than the normal stress times the friction coefficient, the stress at the interface is set equal to the value of the shear stress and the interface does not displace.

(2) If the shear stress is greater than the product of the normal stress and friction coefficient, then the shear stress is set equal to the value of the normal stress times the friction coefficient and the interface slips.

(3) If the normal tractions are greater than the initial compressive stress, the interface is allowed to open and the shear stress is set equal to zero.

$$\begin{vmatrix} \sigma_{1x} \\ \sigma_{1y} \\ \sigma_{2x} \\ . \\ . \\ . \\ \sigma_{ny} \\ \hline ? \\ ? \\ . \\ . \\ . \\ ? \end{vmatrix} = \begin{vmatrix} C_{11} & \cdots & C_{1n} \\ . & & . \\ . & & . \\ . & & . \\ . & & . \\ . & & . \\ . & & . \\ . & & . \\ . & & . \\ . & & . \\ . & & . \\ C_{n1} & \cdots & C_{nn} \end{vmatrix} \begin{vmatrix} ? \\ ? \\ ? \\ . \\ . \\ . \\ ? \\ \hline 0 \\ 0 \\ . \\ . \\ . \\ 0 \end{vmatrix} \qquad (17)$$

Given these stresses, displacements are updated through application of Equation (17) once again. Once the displacements are known, new stresses are calculated, and the procedure is repeated until equilibrium is reached. The final solution is determined through n iterations; applying tractions of p/n along the crack plane at each increment.

Once the crack opening displacements for each collocation point are known, stress intensity values along the crack periphery may be calculated. Recalling that the periphery is assumed to open as a parabola, $\delta(r)$ is determined using standard curve fitting routines (Figure F5). Given $\delta(r)$, K_I, K_{II}, and K_{III} are estimated using Equation (18).

$$\delta_i = K_i A_i(\nu, E)\rho^{\frac{1}{2}}$$

$$i = I,\ II,\ III$$

$$A_I = A_{II} = \frac{4(1-\nu^2)}{E\sqrt{2\pi}} \qquad (18)$$

$$A_{III} = \frac{8(1+\nu)}{E\sqrt{2\pi}}$$

where ρ is the perpendicular distance from the crack periphery.

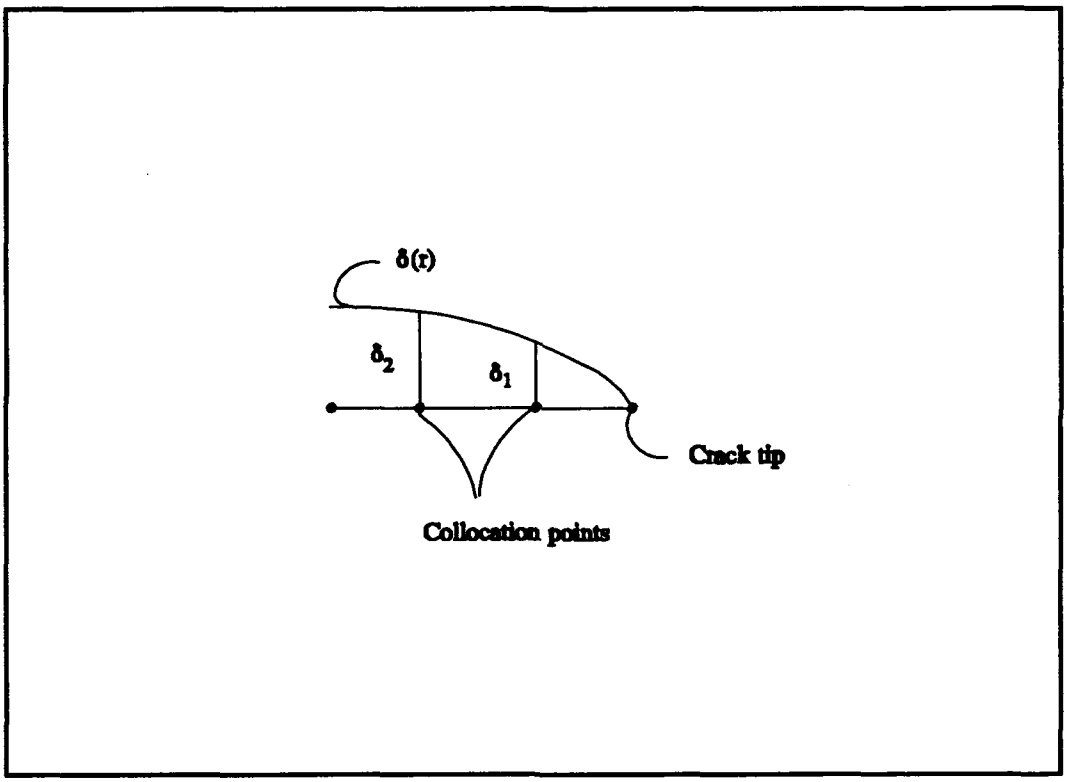

Figure F5 Opening displacement for crack-tip element

2.1 The Dipole Concept

The discussion which follows examines the utility of representing fractures as a continuous distribution of force dipoles as presented by Keat [33f]. Representation of a nucleus of strain by a pair of opposing concentrated forces is not new and may be traced back to Love [21]. What is new, is its application to fracture behavior.

Consider a pair of parallel but opposing point forces, equal in magnitude and separated by a distance, δ. In general, the forces need not be collinear. The displacements and stresses created by the force system may be determined presupposing that the solution to a single point force is known. (Kelvins solution, Equation (1)). Consider, as an example, that the variations in g induced by a single force, **F**, are defined by

$$g = F_i g^i \tag{19}$$

where g^i is a scaler function representing the force's position and the material properties. The magnitude of g due to the dipole shown in Figure F6 is determined through superposition of the two solutions, while noting that the solutions due to both forces may differ by a small amount dg^i. The resulting equation is

$$g = F_i g^i - F_i (g^i + dg^i) = -F_i dg^i \tag{20}$$

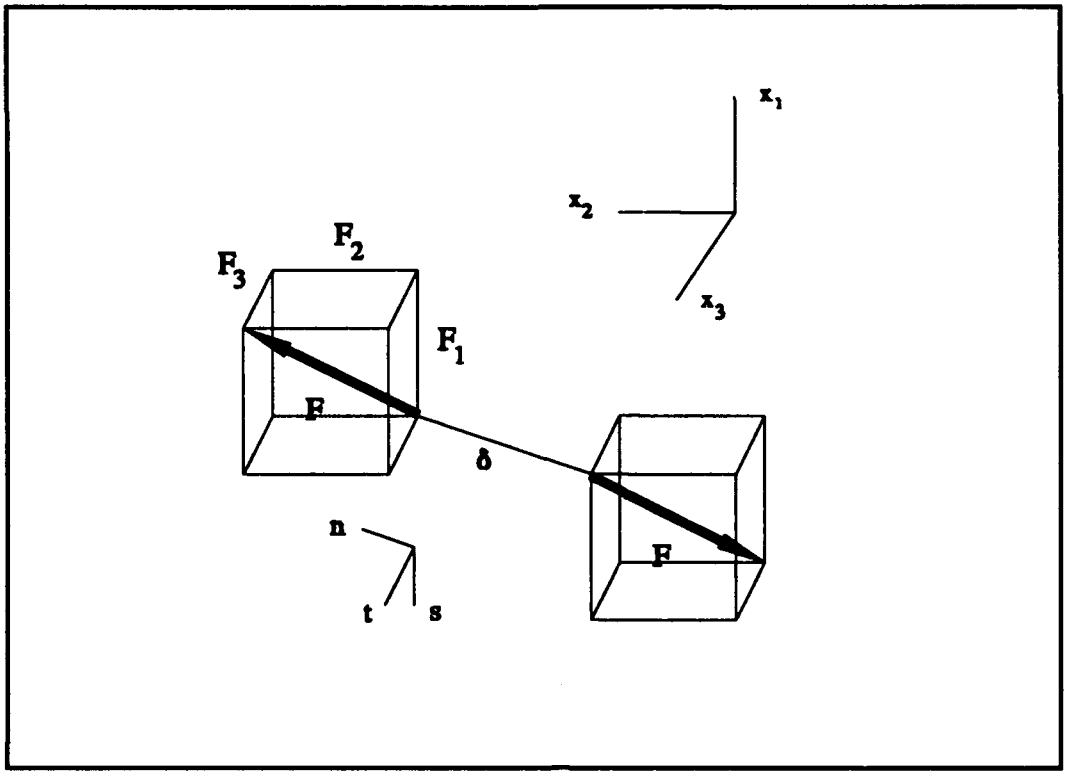

Figure F6 General dipole configuration

Performing a Taylor series expansion of dg^i, Equation (20) becomes

$$g = = F_i \left(\delta\ n_j\ g^i{}_{,j} + \frac{1}{2}\ \delta^2\ n_k\ n_l\ g^i{}_{,kl} + \cdots\right) \tag{21}$$

where **n** is a unit vector directed along the line connecting the two point forces.

The variation in g due to the force dipole is found via a limiting process of allowing δ to approach zero, while keeping the products $\delta\ F_i$ constant. This necessitates $F_i \rightarrow \infty$; resulting in an infinite strain between the two point forces defined by Equation (22).

$$g = -\delta F_i n_j g^i{}_{,j} \tag{22}$$

It is convenient to resolve **F** into components which are collinear and orthogonal to the unit vector, **n**. The collinear pair of forces creates what is known as a *tensile dipole* while the resultant of the orthogonal forces is known as a *shear dipole*. The displacement field emanating from the two dipoles is shown schematically in Figure F7. The reader will note the similarity to dipoles (or doublets) used in irrotational fluid flow and magnetic field theory.

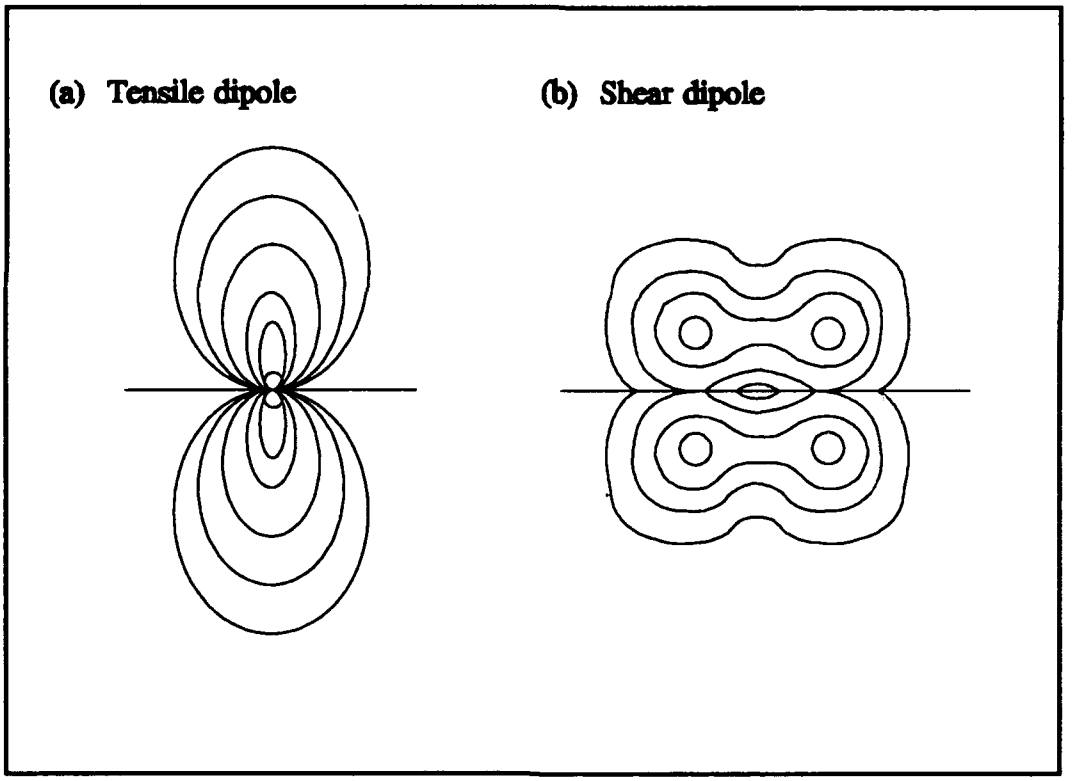

Figure F7 Typical scaler fields produced by tensile and shear dipoles

Note that an arbitrarily oriented dipole in three dimensional space (Figure F6) yields a single tensile dipole perpendicular to the s-t plane, and two shear dipoles describing rotations in the n-s and n-t planes respectively. Equation (23) represents the strength of the different dipoles.

$$\begin{aligned} g &= -\delta\, P_1\, n_i\, n_j\, g^i{}_{,j} \qquad \textit{tensile} \\ g &= -\delta\, P_2\, s_i\, n_j\, g^i{}_{,j} \qquad \textit{shear} \\ g &= -\delta\, P_3\, t_i\, n_j\, g^i{}_{,j} \qquad \textit{shear} \end{aligned} \tag{23}$$

where P_i is the magnitude of each force, and δP_i is the dipole intensity. Each dipole models one of the crack displacement modes described in chapter one on page 1-13.

To model the mode I pressurized crack problem considered throughout this paper, the tensile dipole is supplemented with a pair of laterally acting tensile dipoles scaled to eliminate any Poisson contractions which may occur. Superposition of these three results in an equation of the form

$$g = -\delta P_1 [n_i\, n_j\, g^i{}_{,j} + (\frac{\nu}{1-\nu})\, (s_i\, s_j\, g^i{}_{,j} + t_i\, t_j\, g^i{}_{,j})] \tag{24}$$

Shear components are modelled by pairs of self-equilibrating shear dipoles as shown in Figure F8 (a). Corresponding displacements used in the displacement discontinuity techniques are shown in Figure F8 (b). The resulting stresses and strains are completely defined by δ, P_i, and D_i. Substitution of these parameters into Hooke's law results in the following relationship between the dipole strengths, δ_i, and the displacement

$$\begin{aligned} \delta_1 &= \frac{E(1-\nu)}{(1+\nu)(1-2\nu)} D_1 \\ \delta_2 &= GD_2 \\ \delta_3 &= GD_3 \end{aligned} \tag{25}$$

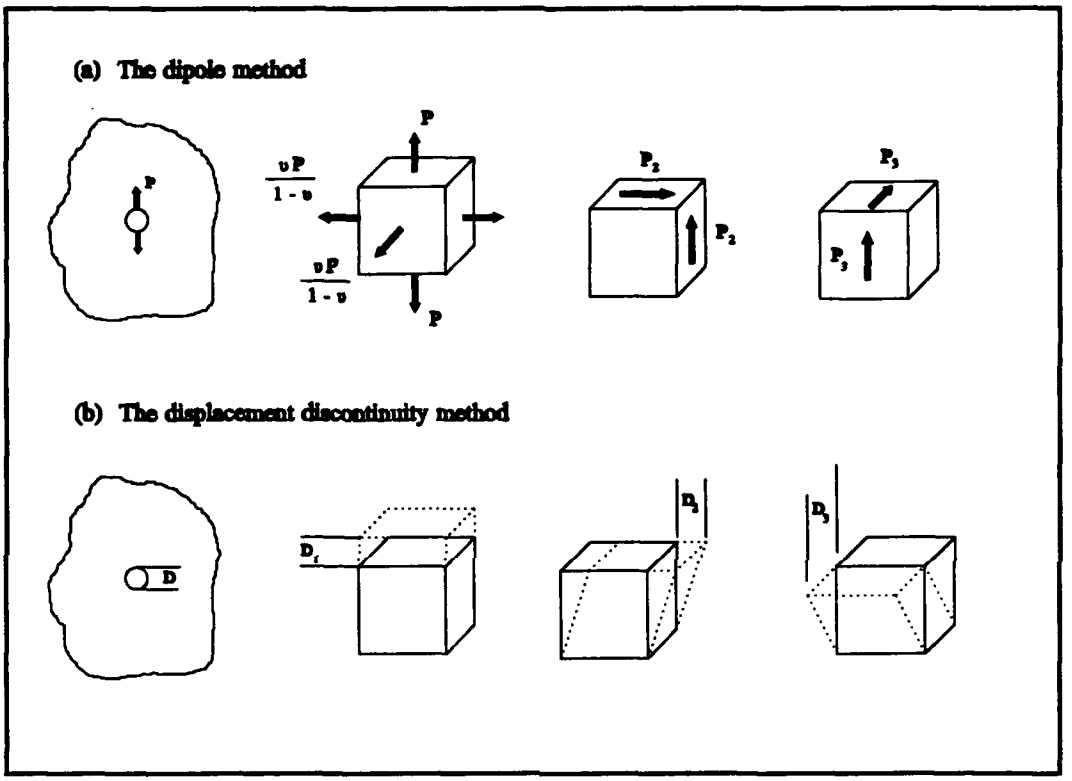

Figure F8 Dipole systems and equivalent displacement discontinuities

Solutions using the dipole method are found through a single integration of the "new" fundamental solution corresponding to the force dipole (as opposed to Kelvin's solution to a point force). Displacement discontinuity techniques integrate the original fundamental solution over both crack surfaces, and than incorporate superposition. The two methods are equivalent, only the mathematical order is interchanged.

3. Numerical Procedure

Equation 12 (repeated below) describes the state of stress at any point within an infinite medium due to a single element with a continuous distribution of force dipoles.

$$
\begin{aligned}
u_x &= \delta_{\bar{x}}[(2\nu-1)\sin\beta\bar{F}_2+2(1-\nu)\cos\beta\bar{F}_3+\bar{y}(\sin\beta\bar{F}_4-\cos\beta\bar{F}_5)] \\
&\quad +\delta_{\bar{y}}[(2\nu-1)\cos\beta\bar{F}_2-2(1-\nu)\sin\beta\bar{F}_3-\bar{y}(\cos\beta\bar{F}_4+\sin\beta\bar{F}_5)] \\
u_y &= \delta_{\bar{x}}[-(2\nu-1)\cos\beta\bar{F}_2+2(1-\nu)\sin\beta\bar{F}_3-\bar{y}(\cos\beta\bar{F}_4+\sin\beta\bar{F}_5)] \\
&\quad +\delta_{\bar{y}}[(2\nu-1)\sin\beta\bar{F}_2+2(1-\nu)\cos\beta\bar{F}_3-\bar{y}(\sin\beta\bar{F}_4-\cos\beta\bar{F}_5)] \\
\sigma_{xx} &= 2G\delta_{\bar{x}}[2\cos^2\beta\bar{F}_4+\sin(2\beta)\bar{F}_5+\bar{y}(\cos(2\beta)\bar{F}_6-\sin(2\beta)\bar{F}_7)] \\
&\quad +2G\delta_{\bar{y}}[-\bar{F}_5+\bar{y}(\sin(2\beta)\bar{F}_6+\cos(2\beta)\bar{F}_7)] \\
\sigma_{yy} &= 2G\delta_{\bar{x}}[2\sin^2\beta\bar{F}_4-\sin(2\beta)\bar{F}_5-\bar{y}(\cos(2\beta)\bar{F}_6-\sin(2\beta)\bar{F}_7)] \\
&\quad +2G\delta_{\bar{y}}[-\bar{F}_5-\bar{y}(\sin(2\beta)\bar{F}_6+\cos(2\beta)\bar{F}_7)] \\
\sigma_{xx} &= 2G\delta_{\bar{x}}[\sin(2\beta)\bar{F}_4-\cos(2\beta)\bar{F}_5+\bar{y}(\sin(2\beta)\bar{F}_6+\cos(2\beta)\bar{F}_7)] \\
&\quad +2G\delta_{\bar{y}}[-\bar{y}(\cos(2\beta)\bar{F}_6-\sin(2\beta)\bar{F}_7)]
\end{aligned}
\tag{12}
$$

If the solution is summed across all the elements defining the crack domain, the equilibrium state at that point is fully defined. Let the domain be defined by N discrete elements; each element comprising a single collocation point at the midpoint of the element and a local frame of reference

$$s = \bar{x} \qquad n = \bar{y}$$

where x (bar) and y (bar) are defined according to Figure F4. Examining the displacement and stresses fields created by one element, i, upon another element, j, Equation (12) can be written as

$$
\begin{aligned}
u_s^i &= B_{ss}^{ij}\,\delta_s^j + B_{sn}^{ij}\,\delta_n^j \\
&= \delta_s^j[(1-2\nu)\sin\gamma\bar{F}_2+2(1-\nu)\cos\gamma\bar{F}_3 \\
&- \bar{y}(\sin\gamma\bar{F}_4+\cos\gamma\bar{F}_5)] \\
&+ \delta_n^j[-(1-2\nu)\cos\gamma\bar{F}_2+2(1-\nu)\sin\gamma\bar{F}_3 \\
&- \bar{y}(\cos\gamma\bar{F}_4-\sin\gamma\bar{F}_5)] \\
u_n^i &= B_{ns}^{ij}\,\delta_s^j + B_{nn}^{ij}\,\delta_n^j \\
&= \delta_s^j[(1-2\nu)\cos\gamma\bar{F}_2-2(1-\nu)\sin\gamma\bar{F}_3 \\
&- \bar{y}(\cos\gamma\bar{F}_4-\sin\gamma\bar{F}_5)] \\
&+ \delta_n^j[(1-2\nu)\sin\gamma\bar{F}_2+2(1-2\nu)\cos\gamma\bar{F}_3 \\
&+ \bar{y}(\sin\gamma\bar{F}_4+\cos\gamma\bar{F}_5)] \\
\sigma_n^i &= A_{ns}^{ij}\delta_s^j+A_{nn}^{ij}\delta_n^j \\
&= 2G\delta_s^j[2\sin^2\gamma\bar{F}_4+\sin(2\gamma)\bar{F}_5 \\
&-\bar{y}(\cos(2\gamma)\bar{F}_6+\sin(2\gamma)\bar{F}_7)] \\
&+2G\delta_n^j[-\bar{F}_5+\bar{y}(\sin(2\gamma)\bar{F}_6-\cos(2\gamma)\bar{F}_7)] \\
\sigma_s^i &= A_{ss}^{ij}\delta_s^j+A_{sn}^{ij}\delta_n^j \\
&= 2G\delta_s^j[-\sin(2\gamma)\bar{F}_4-\cos(2\gamma)\bar{F}_5 \\
&-\bar{y}(\sin(2\gamma)\bar{F}_6-\cos(2\gamma)\bar{F}_7)] \\
&+2G\delta_n^j[-\bar{y}(\cos(2\gamma)\bar{F}_6+\sin(2\gamma)\bar{F}_7)]
\end{aligned}
\qquad (26)
$$

where γ is the relative angle between the two elements defined by β_i - β_j. The total solution for any point within the region of interest is calculated by summing the influence of all N elements along the crack domain (Equation (27)).

$$
\begin{aligned}
u_s^i &= \sum_{j=1}^{N} (B_{ss}^{ij}\delta_s^j) + \sum_{j=1}^{N} (B_{sn}^{ij}\delta_n^j) \qquad i=1..N \\
u_n^i &= \sum_{j=1}^{N} (B_{ns}^{ij}\delta_s^j) + \sum_{j=1}^{N} (B_{nn}^{ij}\delta_n^j) \qquad i=1..N \\
\sigma_s^i &= \sum_{j=1}^{N} (A_{ss}^{ij}\delta_s^j) + \sum_{j=1}^{N} (A_{sn}^{ij}\delta_n^j) \qquad i=1..N \\
\sigma_n^i &= \sum_{j=1}^{N} (A_{ns}^{ij}\delta_s^j) + \sum_{j=1}^{N} (A_{nn}^{ij}\delta_n^j) \qquad i=1..N
\end{aligned}
\tag{27}
$$

where the A's and B's are known as the influence coefficients. As an example, A^{ij}_{ss} represents the shear stress generated at the "i"th element based upon a unit shear displacement at the "j"th element.

The system of equations generated by N discrete elements consists of 4N equations in 4N variables as defined by Equation (27). Prescribed boundary conditions reduce the system of equations to 2N algebraic equations in 2N unknown displacement discontinuities (or strength of the singularities). Unfortunately, the BEM model creates a fully populated 2N by 2N matrix which is generally solved by Gaussian elimination. A similar FEM model would consist of many more degrees of freedom; however, the solution matrix is banded and can be solved using more efficient algorithms (eg. wavefront method) [6]. Once the singularity strengths (crack opening displacements) are known, the stresses for any point in space may be determined by placing the proper spacial coordinates into the matrix of influence coefficient defined by Equation (16).

3.1 Symmetry Considerations

Since structural nodes are not used in boundary element solutions as in standard finite element techniques (only geometric nodes are incorporated), a line of symmetry cannot be imposed by simply constraining (or freeing) specific degrees of freedom along an edge of the mesh. Instead a line of symmetry acts as a "mirror;" reflecting the stress components to a point which is not only co-planar with its corresponding point but also placed symmetrically with respect to the same point as viewed from an observer along the line of symmetry. The conditions which are enforced ensure that no normal displacements occur across the line, and that no shear stresses act along it. These two physical constraints are maintained by reflecting shear components which are equal in magnitude but opposite in sign. The normal reflections are always equal (magnitude and direction).

Bibliography

[1] Anderson, T. L. *Fracture Mechanics, Fundamentals and Applications.* CRC Press, 1991, pp 95-101.

[2] Atkins, A. G. and Y. W. Mai. *Elastic and Plastic Fracture: Metals, Polymers, Ceramics, Composites, Biological Materials.* New York: John Wiley and Sons, 1985, pp 796.

[3] Bowen, H. K. "Advanced Ceramics," *Journal of the American Ceramic Society, 73*: 169-176 (1990).

[4] Broek, David. *Elementary Engineering Fracture Mechanics.* Dordrecht: Kluwer Academic Publishers, 1986, pp 115-122.

[5] Cook and Erdogan. "Stresses in Bonded Materials with a Crack Perpendicular to the Interface," *Journal of Engineering Science, 10*: 677-697 (1972).

[6] Cook, R. *et al. Concepts and Applications of Finite Element Analysis* (Third Edition). New York: John Wiley and Sons, 1989, pp 170-190.

[7] Coyle, T. W. *et al.* "High Temperature Structural Composites: Synthesis, Characterization, and Properties," *Proceedings of the 1987 Northeast Regional Meeting of TMS.* Hobokean, NJ, 1987.

[8] Coyle, T. W. *et al.* "Fracture Mechanics Characterization of Crack/Fiber Interactions in Ceramic Matrix Composites," *Ceramic Engineering and Scientific Proceedings, 8*: 630-635 (1987).

[9] Crouch, S. L. and A. M. Starfield. *Boundary Element Methods in Solid Mechanics.* London: George Allen and Unwin Ltd., 1983, pp 1-7.

[10] Evans, Anthony G. "Perspective on the Development of High-Toughness Ceramics," *Journal of the American Ceramic Society, 73:* 187-206 (1990).

[11] Findley, W. *et al. Creep and Relaxation of Nonlinear Viscoelastic Materials.* New York: Dover Publications, Inc., 1976, pp 3-15.

[12] Griffith, A. A. "The Phenomena of Rupture and Flow in Solids," *Philosophical Transactions, 221:* 163-198 (1920).

[13] He, Ming-Yuan and J. W. Hutchinson. "Crack Deflection at an Interface Between Dissimiliar Elastic Materials," *International Journal of Solid Structures 24:* 1053-1067 (1989).

[14] Jayatilaka, A. *Fracture of Engineering Brittle Materials.* London: Applied Science Publishers, 1979.

[15] Keat, W. D. *et al.* "Computational and Experimental Simulation of 3-D Fracture in Ceramic Fiber - Ceramic Matrix Composites," *Ceramic Engineering and Scientific Proceedings, 12*: 1389-1407 (1991).

[16] Kerans, Ronald J. *et al.* "The Role of the Fiber-Matrix Interface in Ceramic Composites," *Ceramic Bulletin, 68:* 429-442 (1989).

[17] Kerans, Ronald J. and Triplicane A. Parthasarathy. "Theoretical Analysis of the Fiber Pullout and Pushout Tests," *Journal of the American Ceramic Society, 74:* 1585-1596 (1991).

[18] Kreyszig, E. *Advanced Engineering Mathematics* (Sixth Edition). New York: John Wiley and Sons, 1988, pp 767-800.

[19] Larson, Michael C. *Theoretical and Experimental Analysis of Toughening in Brittle Matrix - Brittle Fiber Ceramic Composites with Frictional Interfaces.* PhD Thesis. Massachusetts Institute of Technology, Cambridge MA, 1992.

[20] Lewis, D. "Strength and Toughness of Fiber-Reinforced Ceramics and Related Interface Behavior," *Proceedings of an International Conference.* 265-273. 1988.

[21] Love, A. E. H. *A Treatise on the Mathematical Theory of Elasticity.* New York: Dover Publications, 1984, pp 183-220.

[22] Morrison, Jill K. "Analysis of Fiber Debonding and Pullout in Composites," *Journal of Engineering Mechanics, 114*: 277-287. (February 1988).

[23] Mukherjee, S. *Boundary Element Methods in Creep and Fracture.* New York: Applied Science Publishers, 1982, pp 1-3.

[24] Pan, Tsung-Yu *et al.* "Fractographic Study of Transverse Cracks in a Fibre Composite," *Journal of Materials Science, 23*: 2553-2563 (July 1988).

[25] Pfaender, Heinz G. *Schott Guide to Glass.* New York: Van Nostrand Reinhold Company, Inc., 1983, pp 16.

[26] Rice, J. R. "Elastic Fracture Mechanics Concepts for Interfacial Cracks," *Journal of Applied Mechanics, 55*: 98-103. (1988).

[27] Saada, A. *Elasticity: Theory and Applications.* Florida: Robert E. Krieger Publishing Company Inc., 1974, pp 147-162.

[28] Shand, E. B. *Glass Engineering Handbook* (Second Edition). New York: McGraw-Hill Book Company, Inc., 1958, pp 45-46.

[29] Tada, H. *The Stress Analysis of Cracks Handbook* (Second Edition). St. Louis: Paris Productions Inc., 1985.

[30] Timoshenko, S. *Strength of Materials: Part II - Advanced Theory and Problems.* New York: D. Van Nostrand Company, Inc., 1947, 288-297.

[31] Uhlmann, D. R. "Elasticity and Strength in Glasses," *Glass: Science and Technology*, Volume 5, edited by M. J. Kreidl. New York: Academic Press, 1980, pp 14-47.

[32f] Crouch, S. L. "Solution of Plane Elasticity Problems by the Displacement Discontinutiy Method," *International Journal for Numerical Methods in Engineering, 10*: 301-343. (1976).

[33f] Keat, W. D. *Surface Integral and Finite Element Hybrid Method for the Analysis of Three-Dimensional Fractures.* PhD Thesis. Massachusetts Institute of Technology, Cambridge, MA, 1989.

Vita

Captain James Paul Solti was born on 2 July 1966 in Ashtabula, Ohio. He graduated from Ashtabula High School located in Ashtabula, Ohio in 1984 and attended the United States Air Force Academy, graduating with a Bachelor of Science in Engineering Sciences on 1 June 1988. He was commissioned into the United States Air Force on the same date. He began his first Air Force tour as a mechanical engineer at Eglin Air Force Base, Florida. He served at the Air Force Armament Laoboratory (AFSC) from 3 August 1988 to 10 May 1991. He currently lives in London, Ohio with his wife Christine.

Permanent Address:

2716 Douglas Road
Ashtabula, Ohio 44004

REPORT DOCUMENTATION PAGE

Form Approved
OMB No. 0704-0188

1. AGENCY USE ONLY (Leave blank)	2. REPORT DATE	3. REPORT TYPE AND DATES COVERED
	December 1992	Master's Thesis

4. TITLE AND SUBTITLE
Computational and Experimental Investigation Into Fracture of Brittle Fiber - Brittle Matrix Composite Systems

5. FUNDING NUMBERS

6. AUTHOR(S)
James P. Solti, Captain, USAF

7. PERFORMING ORGANIZATION NAME(S) AND ADDRESS(ES)
Air Force Institute of Technology
Wright-Patterson Air Force Base
Ohio 45433-6583

8. PERFORMING ORGANIZATION REPORT NUMBER
AFIT/GAE/ENY/92D-04

9. SPONSORING / MONITORING AGENCY NAME(S) AND ADDRESS(ES)

10. SPONSORING / MONITORING AGENCY REPORT NUMBER

11. SUPPLEMENTARY NOTES

12a. DISTRIBUTION / AVAILABILITY STATEMENT
Approved for public release; distribution unlimited

12b. DISTRIBUTION CODE

13. ABSTRACT *(Maximum 200 words)*

Experimental and computational analyses provided an improved understanding of quasi-static fracture in model composite systems. Constant displacement compression tests using borosilicate glass double cleavage drilled compression test templates provided qualitative assessments of localized toughening for crack growth near cylindrical inclusions. Large crack-tip stress fields induced interfacial slip and separation prior to arrival of the main crack. Debonding and the proliferation of secondary matrix cracks characterized the role of bridging fibers along weak interfaces. Strong residual normal compressive interfacial stresses diminished the influence of crack-tip stresses; however, slip was still observed. VHS tape and computer enhanced photos record a history of crack propagation and interfacial slip. Experimental data was used to validate a fully three-dimensional computational code capable of analyzing fracture near and around cylindrical inclusions. Consistent variations in the shape of the crack periphery renders confidence in the elasticity solution.

14. SUBJECT TERMS	15. NUMBER OF PAGES
Crack Propagation; Fracture Mechanics; Quasi-static Fracture Brittle Composites; Toughening; Slip and Debonding	158
	16. PRICE CODE

17. SECURITY CLASSIFICATION OF REPORT	18. SECURITY CLASSIFICATION OF THIS PAGE	19. SECURITY CLASSIFICATION OF ABSTRACT	20. LIMITATION OF ABSTRACT
Unclassified	Unclassified	Unclassified	UL